Master Thesis

"Hybrid nanowire/perovskite solar cells"

Eleftheria Darivianaki

Supervisor: Prof. Nikos Pelekanos

DEPARTMENT OF MATERIALS SCIENCE AND TECHNOLOGY

UNIVERSITY OF CRETE

FOUNDATION FOR RESEARCH AND TECHNOLOGY OF HELLAS

Committee

Prof. N. Pelekanos (Supervisor)
Associate Prof. C. Stoumpos
Associate Prof. Z. Chatzopoulos

Heraklion, December 2019

Contents

Abstract

Perovskite solar cells attract much interest in photovoltaic applications nowadays, due to the high solar cell performance that they exhibit, combined with the relative ease of fabrication. Moreover, III-V nanowires, such as for instance GaAs nanowires also constitute a matter of research due to their excellent optoelectronic properties, such as high mobility of carriers and optimum bandgap. Moreover, the reduced cost of fabrication is another advantage of nanowires. Due to their properties, GaAs nanowires could be used as an Electron Transporting Material (ETM) in perovskite solar cells, replacing conventional ETMs, like titanium dioxide (TiO_2). Compared to TiO_2, GaAs has orders of magnitude higher electron mobility value. Moreover, the energy levels of intrinsic GaAs favor band alignment of GaAs conduction band with the LUMO orbital of $CH_3NH_3PbI_3$ perovskite. So, effective electron extraction can be achieved. Thus, GaAs nanowires could be a better choice as an ETM in perovskite solar cells. In the present thesis, hybrid GaAs nanowire/perovskite solar cell devices were fabricated. Moreover, electro-optical characterization of the samples was accomplished.

Acknowledgments

Firstly, I would like to thank my supervisor professor Nikos Pelekanos for his guidance and supervision of my experimental work. I would also like to thank professor C. Stoumpos for his assistance and his directions in my experimental work. Moreover, I thank Maria Androulidaki for her assistance in my experiments. I would also like to thank Professor Zacharias Chatzopoulos for nanowire's growth. Furthermore, I would also like to thank Mr Thanassis Kostopoulos, Mr George Stavrinidis, Mr George Konstantinidis for involving with the deposition of BCB and the metallizations of our samples. What' s more, I thank Mrs K. Tsagaraki for the SEM images of the samples, Mrs Maria Kayabaki for the I-V characterization of the samples. Additionally, I would like to thank the whole microelectronics research group for the excellent co-operation, and finally my family for their support to complete this work.

Dedication

The thesis is dedicated to my twin sister for her support throughout the process of completing my work.

CHAPTER 1

1.1 Introduction

Solar energy is a renewable source of energy that could replace other sources of energy like fossil fuels which cause harmful effects on the environment. The utilization of solar energy can contribute to the solution of many environmental problems. For this reason, solar cell technology is developed and research is carried out for the improvement of the photovoltaic performance. The evolution of solar cell technology passing through many improvement steps from generation to generation is mentioned below *[16]* :

The first-generation solar cells, mainly single crystals grown on silicon wafers.
- Single/ Mono-crystalline silicon solar cell
- Poly/Multi-crystalline silicon solar cell

The second-generation solar cells—Thin Film Solar Cells
- Amorphous Silicon Thin Film (a-Si) Solar Cell
- Cadmium Telluride (CdTe) Thin Film Solar Cell
- Copper Indium Gallium Di-Selenide (CIGS) Solar Cells

Third Generation Solar Cells
- Nano Crystal Based Solar Cells
- Polymer solar cells (PSC)
- Dye Sensitized Solar Cells (DSSC)
- Concentrating photovoltaic (CPV)

Perovskite Based Solar Cell

Doping

Intrinsic semiconductors are the semiconductors that have a very low number of free carriers. Impurities of other atoms can be introduced in a semiconductor (doping), so as to increase the number of free carriers. Particularly, two different kinds of atoms can be introduced. Donors which increase the number of free electrons and acceptors which increase the number of free holes. Therefore, when the material has an excess in electrons it is called an n-type material, while when it has an excess in holes, it is called a p-type material.

P-N junction

A p-n junction is formed by the contact of an n-type and a p-type semiconducting material. In a p-n junction three regions are distinguished as can be seen in figure 1.1, the p-region, the n-region and a space charge region (SCR) which is formed at the interface between the p- and n-doped materials. At the SCR region an electric field is generated due to the existence of opposite charge in that region.

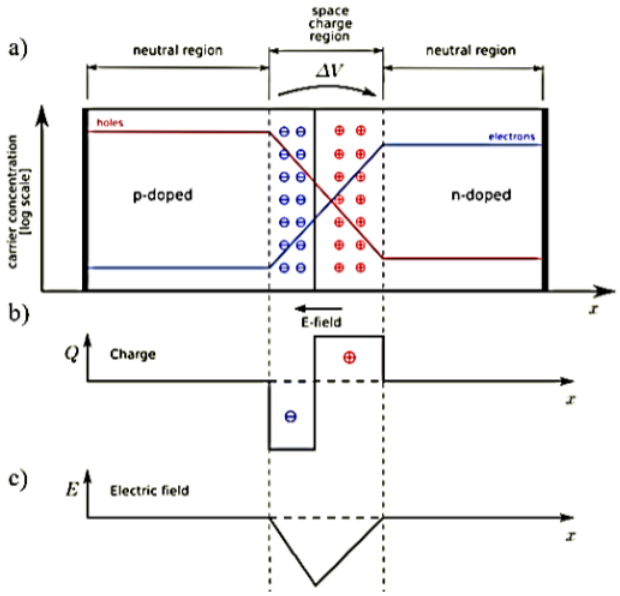

Figure 1.1: An illustration of the regions that constitute the p-n junction and the electric field that is generated in it.

Under the presence of the electric field, both drift current and diffusion current will flow in the p-n junction. Diffusion is a process during which carriers diffuse in the material due to a difference in carrier concentration to reach an equilibrium state. So, with the existence of a concentration gradient, diffusion current is generated. The diffusion current can be described as:

$$J_{D_n} = q * D_n * \frac{dn}{dx} \quad (1.1)$$

$$J_{D_p} = -q * D_p * \frac{dp}{dx} \quad (1.2)$$

for electrons and holes respectively, where:

D_n: Diffusivity for electrons and D_p: Diffusivity for holes

dn/dx and dp/dx is the concentration gradient for electrons and holes respectively.

q: the electronic charge

As for the drift current, the movement of the holes is through the electric field while for the electrons is opposite of the electric field. The velocity of the free carriers is given as:

$$\overrightarrow{u_n} = -\mu_n * \vec{E} \quad (1.3)$$

$$\overrightarrow{u_p} = -\mu_p * \vec{E} \quad (1.4)$$

The drift current for electrons and holes can be described by the formula:

$$J_{n_{drift}} = q * n * \mu_n * \vec{E} \quad (1.5)$$

$$J_{p_{drift}} = q * p * \mu_p * \vec{E} \quad (1.6)$$

The total current density for electrons and holes in the p-n junction is:

$$J_n = q * n * \mu_n * \vec{E} + q * D_n * \frac{dn}{dx} \quad (1.7)$$

$$J_p = q * p * \mu_p * \vec{E} - q * D_n * \frac{dp}{dx} \quad (1.8) \quad [37]$$

The photovoltaic effect

A diode (p-n junction) can operate as a solar cell device under illumination conditions. Photons with energy equal or above bandgap energy are absorbed by the semiconductor. So, electron-hole pairs are generated in the space charge region (depletion region). The electric field directs the electron to the n-type region of the diode and correspondingly the hole to the p-type region of the diode which are finally collected by the electrodes. A voltage is therefore generated (open circuit voltage V_{oc}), as well as a current under short-circuit conditions. The drift current is enhanced. Under no illumination conditions, no extra conduction carriers are generated in the depletion region. In this case, the drift current and the diffusion current are balanced and the p-n junction operates as a diode.

Solar cell response

The equations that describe the response of a solar cell and estimate the output current under or no illumination are the following:

$$I = I_L - I_O \left[e^{\left(\frac{q*V}{n*k*T}\right)} - 1 \right] \quad \text{eq. (1.9)}$$ under no illumination for voltage values: V<100mV.

$$I = I_L - I_O \left[e^{\left(\frac{q*V}{n*k*T}\right)} \right] \quad \text{eq. (1.10)}$$ under illumination for small voltages

In the above equation, I_L expresses the photogenerated current, I_o is the saturation current, V,T,q are the voltage, the temperature and the electronic charge respectively.

Characteristic parameters of the solar cell are short circuit current (I_{sc}), open-circuit voltage (V_{oc}), fill factor (FF) and the device's efficiency (η). In more details, I_{sc} is the current value when the voltage is zero, while V_{oc} is the voltage value when the current is zero. In addition, fill factor is one parameter than can determine the maximum power (P_{max}) generated in the solar cell. It is defined as:

$$FF = \frac{P_m}{(I_{sc} * V_{oc})} \quad eq. (1.11)$$

P_m expresses the maximum point in the power vs Voltage (P-V) curve. In figure 1.2, the solar cell parameters are illustrated.

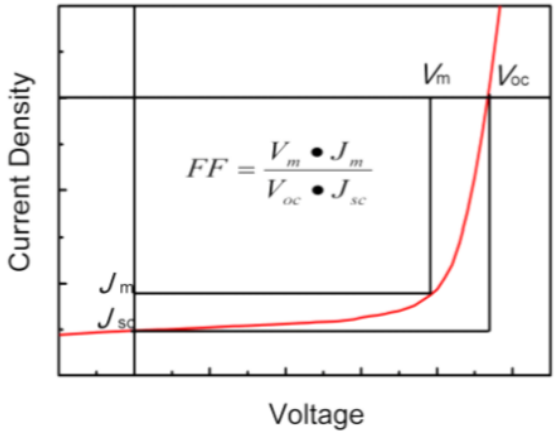

Figure 1.2: I-V curve of the solar cell under illumination where characteristic parameters of the solar cell are illustrated. The inner box represent the points with the maximum power $P_m=V_m*I_m$ *[47].*

Finally, the efficiency of the solar cell device is an important parameter that expresses the fraction of the incident power converting to electricity. It is expressed as:

$$\eta = \frac{P_m}{P_{in}} \quad eq\ (1.12)$$

P_{in} is the incident power which is equal to 1 sun (100mW/cm^2) and P_m the maximum power of the diode in mW/cm^2.

1.2 Nanowire solar cells

Nanowire properties

Nanowires are the nanostructures that have one of their dimensions bigger in size relatively to the other dimensions. Due to their numerous advantages, nanowires constitute a current matter of research. Owing to the properties and the quantum phenomena that nanowires present, they can find many applications. Nanowires are used in a wide range of fields, such as in electronic and photonic applications. Especially GaAs nanowires that are III-V semiconductors are widely studied owing to the in material properties, such as direct bandgap and high mobility values. Nanowire applications comprise single-photon sources, light emitting diodes, lasers, photodetectors, field effect transistors and solar cells *[9].* In this chapter, nanowire heterostructures will be referred mainly to solar cell applications.

For solar cell applications, properties of nanowires like anti-reflecting properties, effective light trapping, wave-guiding effects can lead to enhanced light absorption. Thus, the use of nanowires instead of bulk materials reduces the amount of material needed and therefore the cost of fabrication. What's more, the cost of fabrication can be further decreased, since nanowires due to relaxed lattice matching requirements can be grown on low-cost substrates such as silicon but also conductive glass, stainless steel etc. *[10],[5].*

Nanowire fabrication technique

Molecular Beam Epitaxy (MBE) method is an epitaxy technique that can be used for the growth of thin crystalline films under conditions of ultra-high vacuum (UHV), enabling the formation of film thickness as low as $\sim 10\text{Å}$. As for the epitaxial growth set up, there are special containers, the effusion cells, that contain pure sources of materials which are heated until the material molecules to evaporate. Subsequently, the molecules are deposited on the substrate in the form of vapor. In addition, there is a RHEED system based on a high-energy electron diffraction mechanism that detects changes on the surface crystal structure. Via MBE, we can control film thickness, film composition and doping concentrations, as well as the morphology of film structures. Additionally, films of high crystalline quality are formed. The term "beam" means that the atoms do not interact with each other or with other gases in the vacuum chamber until they deposit on the substrate, due to their high mean free path distance *[3]*.

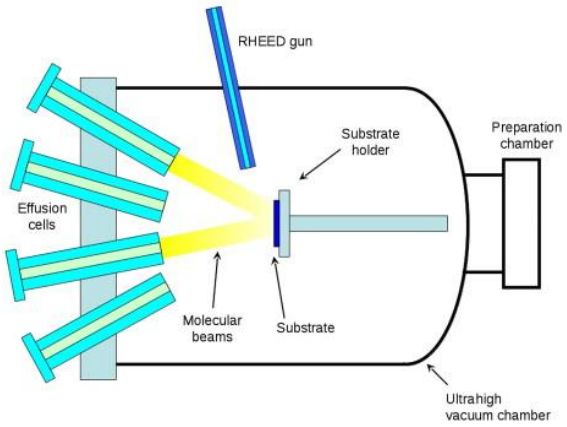

Figure 1.3: The set-up of Molecular Beam Epitaxy method *[4]*

In addition, Vapor-Liquid-Solid (VLS) growth is an epitaxial method that can be used to grow structures in one dimension, like nanowire structures. Particularly, nanowires are grown by chemical vapor deposition on a substrate with the incorporation of a liquid catalyst. The liquid catalyst that is deposited on the substrate constitutes the center of nucleation of nanowire structures and it favors nanowire growth. Particularly, the catalyst droplet adsorbs the molecules of the molecular beams. Subsequently, molecules diffuse in the liquid catalyst droplet. When the liquid solution exceeds equilibrium concentration, molecules diffuse to the interface between the solid and the liquid droplet, so as the free energy of the system to be minimized. As a result, nucleation of nanowire crystal takes place and the nanowire crystal starts to grow. Because of the fact that solid, liquid and vapor phases are needed for the growth of nanowires, the growth of nanowires is called vapor-liquid-solid growth *[15]*.As a liquid catalyst, Au or Ga can be used. In our case, a Ga droplet was used as a catalyst for the nucleation of nanowires instead of Au. One reason for this is that Ga droplet is easier to remove under particular conditions after nanowire growth, in contrast to Au. In figure 1.4 we can see a representation of VLS mechanism for the growth of GaAs nanowires.

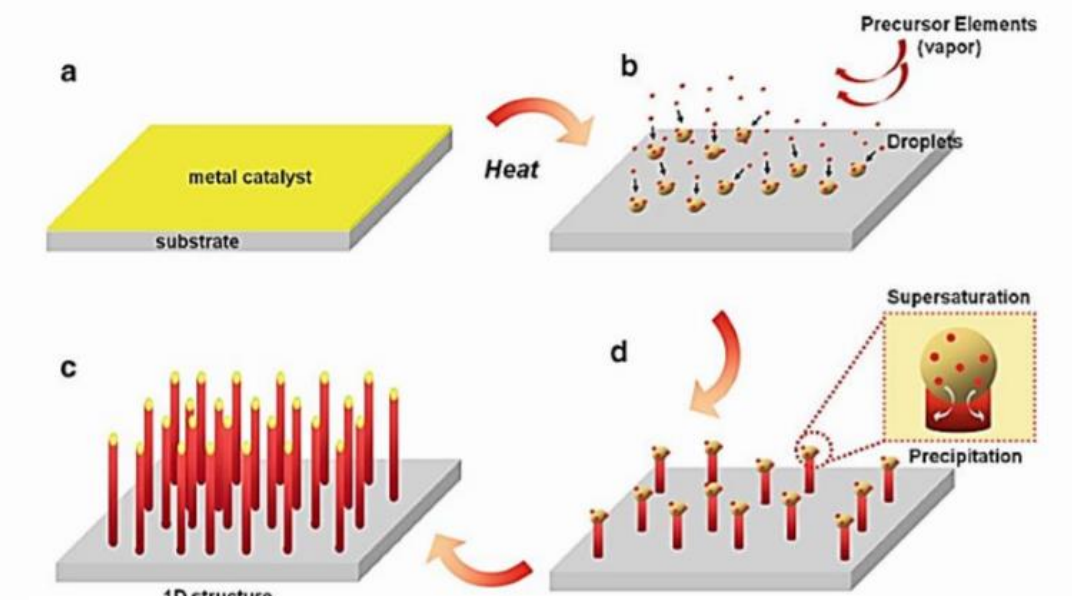

Figure 1.4: Vapor-Liquid-Solid (VLS) mechanism for the growth of nanowires ***[15]***

Benefits of nanowires

Wave-guiding and quantum confinement effects are very important characteristics of nanowires. As far as wave-guiding is concerned, the high refractive index of nanowires combined with their nano-scale dimensions can create wave-guiding paths to the incident radiation, enhancing light absorption *[13].* Optical modes can be guided usually along the nanowire length, according to the electric field polarization *[12].* Due to the wave-guiding properties of nanowires that enhance light coupling, nanowires exhibit increased light absorption compared to planar materials of equivalent volume *[13].*

Moreover, quantum confinement effect appears on nanowires and generally on nanocrystals that have decreased dimensions. Particularly, due to the decreased material dimensions, electrons are confined in a small region in the material, smaller than the typical carrier de Broglie wavelength. Therefore, energy band splitting takes place, leading to a modification in the energy band diagram of the material. As a result, the electrical and optical properties of the material change, such as the density of states and the bandgap energy. The bandgap energy of nanocrystals becomes larger than its bulk bandgap energy. Consequently, by modifying the crystal dimensions, bandgap tuning of the crystal can be achieved *[8].*

Nanowire structures

There are two types of nanowire hetero-structures, radial and axial nanowire hetero-structure. Radial nanowires have a core-shell structure. Specifically, they are composed of a material that constitutes the core of nanowire and a material around it, forming the shell of the nanowire heterostructure. On the other hand, axial nanowires consist of different materials that are deposited axially, along the nanowire, as can be seen in figure 1.5 *[14].* For axial nanowire heterostructures, the nanowire growth is achieved by modifying the growth materials that form the nanowire heterostructure. On the contrary, the radial nanowire growth is achieved by changing the growth conditions during nanowire synthesis *[14].*

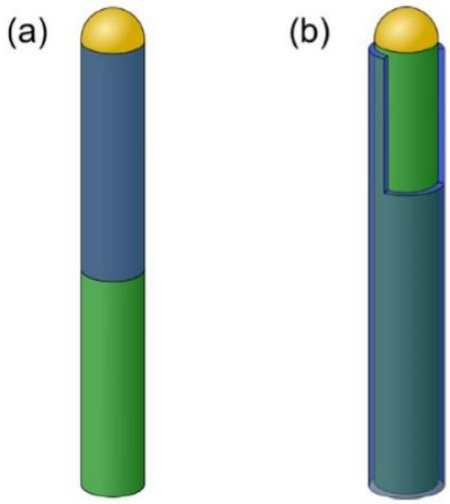

Figure 1.5: (a) Axial and (b) Radial nanowire growth *[14]*.

In solar cell applications, both axial and radial nanowire structures can form a p-n junction or a p-i-n junction. As for radial nanowires, after their growth they are covered by a "passivation" layer, which is another layer whose role is to hinter carrier recombination at the surface of nanowires and enhances the production of photocurrent. Materials used as passivation layers in nanowire solar cells can be aluminium gallium arsenide (AlGaAs), InGaP, AlInP, silicon dioxide, silicon nitride or polymeric materials like BCB *[14]*.

Radial nanowire solar cells are widely used due to the numerous advantages they have. The high aspect surface-to-volume ratio leads to enhanced absorption in the semiconducting material. Moreover, the short junction distance that approaches the nanowire diameter can be comparable to the diffusion length of minority carriers. Thereby, there are many possibilities that generated carriers reach the p-n junction without recombining. Therefore, there is enhanced carrier separation, as well as charge collection by the electrodes. However, the large area of the p-n junction which covers along the nanowire can lead to high dark currents, lower values in open circuit voltage V_{oc} and therefore to low efficiency values. In addition, the fabrication process of radial nanowire solar cells incorporates the involvement of additional layers around the nanowire structure, such as passivation layers which render the fabrication process more complicated.

On the other hand, axial nanowire solar cells have a short area p-n junction being in the axial direction of nanowire structure. Due to the increased thickness of the absorbing material, enhanced optical absorption is noticed. Nevertheless, the distance that carriers travel until they reach the junction is bigger, resulting in increased recombination and not very effective carrier collection, compared to radial nanowire solar cells. Finally, the fabrication process is relatively simpler. According to studies that have been made on nanowire solar cells, radial nanowire solar cells exhibited better photovoltaic efficiency than axial nanowire solar cells *[2].*

Chemical-Physical Oxide.

On the surface of the silicon substrate there is a native oxide. By annealing the native oxide, pores are created which can be used as nucleation centers for the growth of nanowires. Nanowires start to grow within the pores of the native oxide.

The nucleation of nanowire crystals depends on the properties of the native oxide, such as the chemical composition, the roughness and the porosity of the oxide. The composition and the surface properties of the native oxide cannot be controlled, so as the use of native-oxide templates does not provide reproducibility in nanowire growth. So, nanowires that are grown on similar silicon substrates, but the substrates derive from different wafer batches, may very well lead to growth results under identical growth conditions. For this reason, to overwhelm this problem, an "artificial" chemical oxide is developed that substitutes the native oxide.

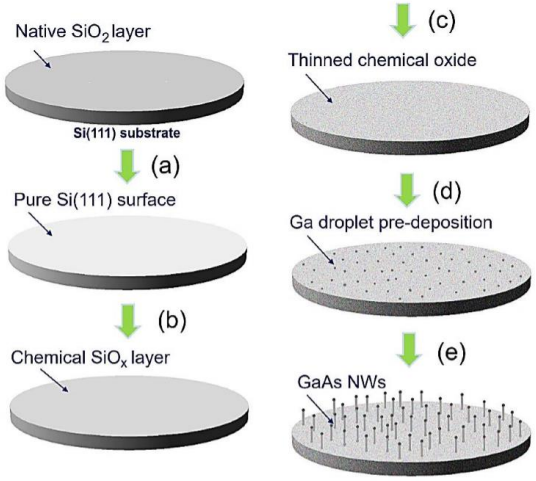

Figure 1.6: Fabrication process of the chemical oxide. The processing steps are: (a)Removing the native oxide layer,(b)The pure substrate is chemically oxidized in a heated HNO_3 solution. (c)Thinning of the chemical oxide layer,(d) Ga droplet pre-deposition for the nucleation of nanowire crystals,(e) Ga-assisted growth of GaAs nanowires *[1]*

In figure 1.6, we can see the processing steps for the fabrication of the chemical oxide on silicon substrate. Comparing the growth of nanowires on native oxide and chemical oxide-covered substrates, the growth of nanowires in the case of native oxide templates exhibit poor uniformity and poor crystalline quality. On the contrary, the development of the chemical oxide provides a good control of the morphology and density of pores on the oxide surface. Therefore, high uniformity of nanowires is achieved with improved crystalline quality, high reproducibility in nanowire growth and a high yield of vertical nanowires. Moreover, there is the ability to fabricate nanowires in different sizes and densities on the same substrate, under the same growth conditions.

In figure 1.7, we can see SEM images which show the growth of GaAs nanowires on Si(111) substrates covered with chemical and native oxide.

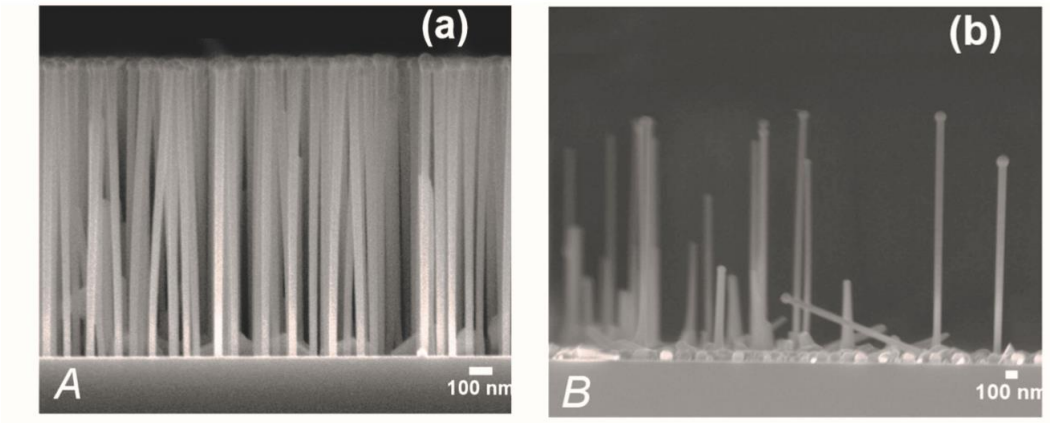

Figure 1.7: SEM images of Ga-assisted GaAs NWs grown on Si(111) substrates covered with (a) chemical oxide and (b) native oxide [1].

Photoluminescence

Photoluminescence is a non-destructive spectroscopic technique in which carriers are excited from the ground state to a higher energy state. This excitation is caused by photons via illumination, usually by a laser. Subsequently, the excited carriers are submitted to relaxation processes, before they perform an e-h recombination emitting a photon. Usually, excitation occurs at an excitation energy $hv>E_g$. The wavelength of the emitted photon which is caused by electron recombination is characteristic of the material studied and not of the incident radiation. So, we can evaluate the quality of materials studied, examining the existence of possible lattice defects in the material. Photoluminescence can be intrinsic taking place in pure materials or crystals or it can be extrinsic referring to materials that incorporate impurities or defects. In pure materials with no impurities or defects, (intrinsic) photoluminescence can be band-to-band at high temperatures. So, carrier transition can occur directly from the conduction band to the valence band. However, at low temperatures exciton photoluminescence takes place. Particularly, exciton luminescence is the recombination of an electron bound to a hole, by Coulomb interaction. The exciton moves into the crystal, carries energy and finally the electron and the hole recombines, giving a characteristic luminescence. For extrinsic photoluminescence, bound excitons to impurities are involved. Photoluminescence intensity is determined by temperature, excitation density as well as the concentration of various impurities and defects *[11].*

The piezoelectric effect

One of the goals in studying radial nanowire heterostructures is the exploitation of piezoelectric effect, which can improve the I-V characteristics of nanowire solar cells. Particularly, materials that have different crystal lattices can be used for the fabrication of nanowires. The difference in crystal structure for these materials causes strain effects in the nanowire layers, due to lattice mismatching. The strain fields that are generated create piezoelectric polarization. The axial component of the piezoelectric polarization generates significant axial piezoelectric fields, while the lateral components of the polarization generate a potential with periodic maxima and minima which have triangular symmetry. These maxima and minima represent confinement regions of electrons and holes. For example, it was reported that piezoelectric polarization can be observed in GaAs/InGaAs core-shell nanowires. Particularly, the nanowires were grown on n^+ Si(111) substrate with molecular beam epitaxy via VLS method. They had a GaAs core thickness of 70nm and an InGaAs shell thickness of 40nm. The potential difference between the periodic maxima and minima approaches

$\sim 100mV$ for 5% Indium (In) incorporation in the shell. This potential difference is enough to ensure effective carrier separation in different parts of the nanowire, reducing recombination of carriers significantly. Therefore, the solar cell efficiency can be improved. In figure 1.8, we can see the piezoelectric potential profile in a cross section of the InGaAs/GaAs core-shell nanowire, with 5% In incorporation *[5].*

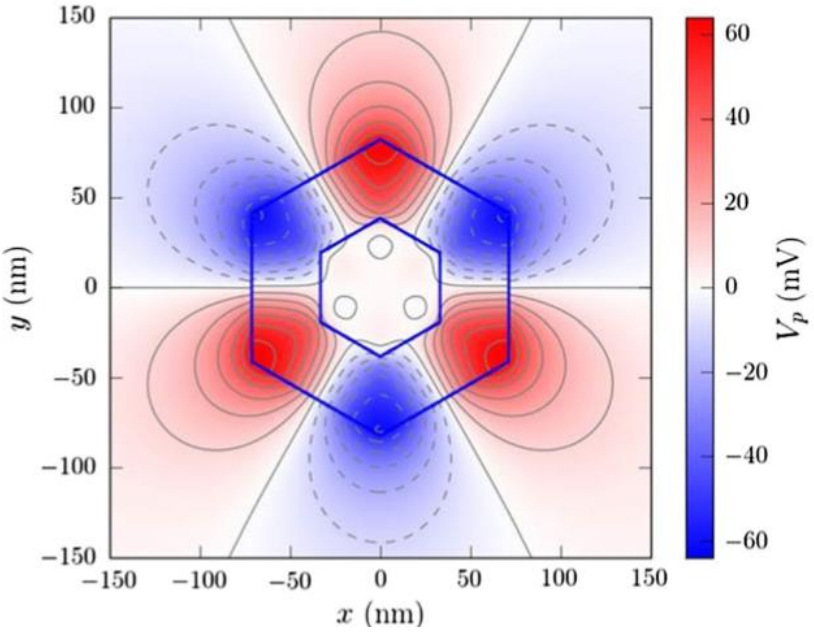

Figure 1.8: Piezoelectric potential profile in a cross section of a InGaAs/GaAs core-shell nanowire structure with a core thickness of 70nm and a shell thickness of 40nm. The shell incorporates 5% In *[5].*

It is worth mentioning that the particular nanowire structure is expected to have gradients in indium concentration. This means that the indium percentage may be different in the various parts of the shell with a higher percentage of In being integrated in the tips of the nanowires compared to nanowire sides.

In figure 1.9 (a), we can see a photoluminescence (PL) spectrum for a InGaAs/GaAs core-shell nanowire sample at a temperature of 12K that has a nanowire shell thickness of 50nm. In figure 1.10(b) we can see PL spectra at low temperature for core-shell nanowire samples that have different nanowire shell thicknesses.

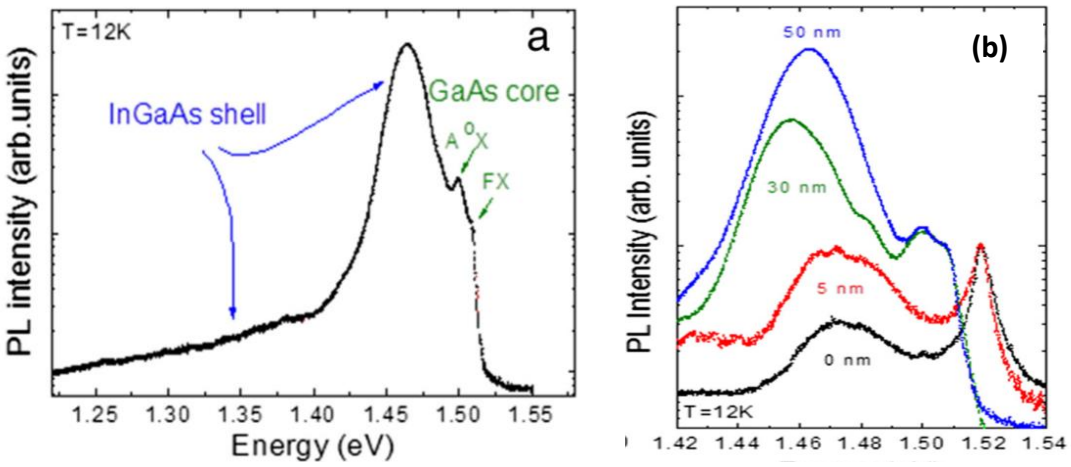

Figure 1.9:(a) PL spectrum at 12 K from a core-shell NW sample with ≈50-nm shell thickness. (b) Comparison of low temperature PL spectra for core-shell NW samples with varying shell thicknesses *[5]*

As we can see from figure 1.9(a), PL spectrum shows an emission which corresponds to the InGaAs shell at about 1.46eV and to GaAs core at 1.509eV and 1.500eV. The core-shell multiple PL emission is attributed to the existence of GaAs free-like excitons (FX) and excitons bound to neutral acceptors (A^0X), respectively. Moreover, from figure 1.9(b) we can notice that as shell thickness increases there is an increased red-shift in PL spectrum. This can be attributed to the strain that is caused by the shell.

In figure 1.10 we can see PL spectra of bulk GaAs, GaAs nanowire sample as a reference and InGaAs /GaAs core-shell nanowire sample. Comparing the PL spectra of GaAs nanowire reference sample and the bulk GaAs, we observe that PL emission is blue-shifted as for the GaAs nanowire reference sample, possibly due to quantum confinement effects as GaAs nanowire diameter decreases. We also notice that the reference nanowire sample has a PL emission at 1.52eV, while the PL spectrum of InGaAs/GaAs nanowire sample is red-shifted compared to the spectrum of the reference sample. The red-shift is assigned to strain effects that are induced by the shell layer *[5]*.

The optimization of parameters can lead to enhanced absorption and improved efficiency in nanowire solar cells. Such parameters are the doping profile, the presence of passivation layers, as well as the geometric characteristics of nanowires.

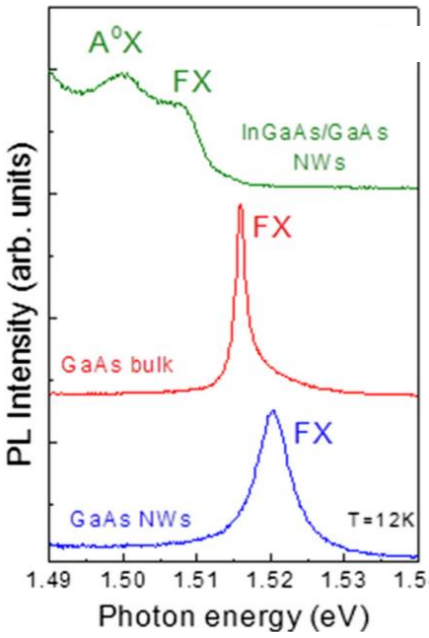

Figure 1.10: Comparison of low-temperature PL spectra at the GaAs band edge between the core-shell NW sample with ≈50-nm shell thickness, an undoped GaAs bulk sample, and reference GaAs NWs ***[5]***

According to a study, InP nanowires were fabricated due to the direct bandgap of InP semiconductor. InP has a bandgap energy equal to 1.34eV which corresponds to a wavelength λ=925nm, suitable for the solar spectrum. Nanowire mean height is <h>=1.5μm, the mean diameter fluctuates between 130nm and 190nm and the mean distance between nanowires is 470nm both in x and y axis. Moreover, the nanowires were fabricated with MOCVD epitaxy method on an InP(111) substrate.

InP nanowires were grown via VLS method. For the nucleation of the nanowire crystal, Au catalyst droplet was used in various sizes. Therefore, nanowires of different diameters were fabricated. Au droplet was finally removed to reduce reflection. A 50nm-thick SiO_2 layer was deposited around nanowires that acts as a "passivation" layer. Above this layer a transparent conducting oxide (TCO) was deposited, 50 nm thick at the base and 38nm thick at the nanowire sides. The TCO forms a hemispherical structure of 130nm on the top of the nanowires. The growth rate of nanowires is 60nm/min. In figure 1.11 we can see the structure of nanowire solar cells, as well as the nanowire dimensions.

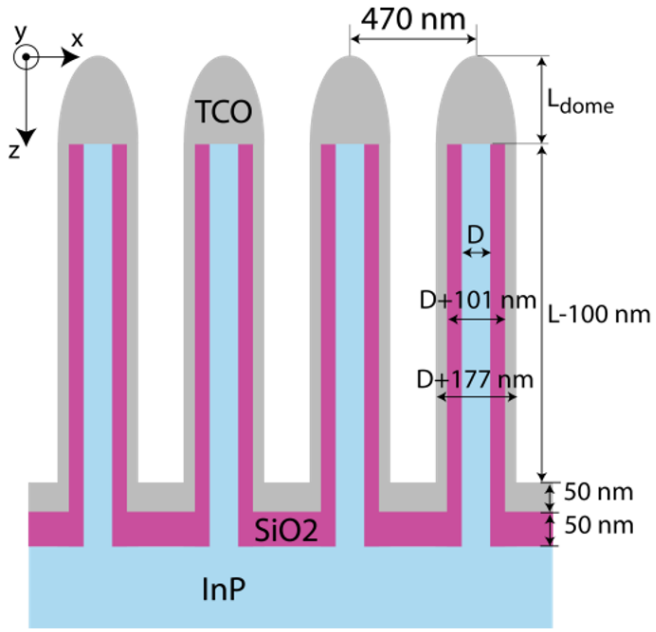

Figure 1.11: Illustration of InP nanowire structure and their dimensions *[6].*

Three nanowire solar cell devices were studied that had different nanowire heights. Particularly, the nanowire heights were L=1.4μm, L=1.5μm and L=1.7μm for cells A,B,C respectively. The I-V characteristics of the nanowire solar cells are the following: The cell A had a current density J_{sc}=24.6mA/cm^2, open circuit voltage Voc=0.791V,a Fill Factor(FF) 72.4% and the maximum efficiency was 13.8%. The cell B had J_{sc}=18.5mA/cm^2, Voc=0.773V, Fill Factor(FF)=68.1% and the maximum efficiency was 8.6%. The cell C had J_{sc}=11.9mA/cm^2, Voc=0.656V, Fill Factor (FF)=61.5% and a maximum efficiency of 4.3% *[2.6].*

According to another study that has been made, axial GaAs nanowires were grown on GaAs (111)B substrate. Nanowires had a diameter D=165nm. Subsequently, AlGaAs was deposited on nanowires as a passivation layer which was 25-40 nm thick. Afterwards, an additional dielectric layer was deposited, SiO_2 layer that was covered by Cyclotene resin. The SiO_2 layer was etched until the nanowire tips to emerge. Finally, a transparent conducting oxide was deposited, as well as a back Au metallic contact to extract carriers to a circuit.

The fabrication process of the axial GaAs nanowires is the following: The GaAs substrate was patterned via lithography printing and the nanowires were grown in a MOCVD reactor via VLS method. Au droplet was used as a catalyst. The nucleation of GaAs nanowires was implemented by using trimethyl gallium and arsenide at 400^0C. P- and n- impurities of dimethyl zinc and trimethyl tin were incorporated in GaAs crystal, so as a p-n junction to be formed at each nanowire. Passivation layers made of AlGaAs were subsequently deposited. In figure 1.12, we can see a SEM image of a nanowire sample which incorporate passivation layers.

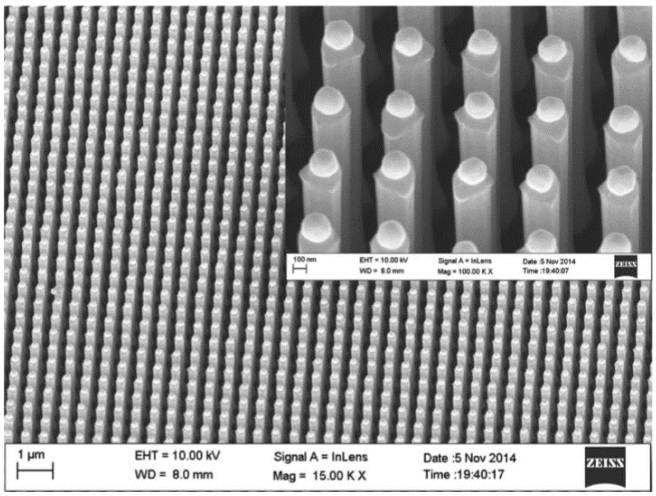

Figure 1.12 :A SEM image of passivated axial GaAs nanowires. The mean nanowire distance between nanowires is 500nm. The inset shows the presence of Au catalyst droplet, on the tips of nanowires that were grown via VLS method *[7]*.

Two GaAs nanowire solar cells were studied. Cell 1 has a nanowire length L=2.8µm and a mean nanowire distance 400nm, while cell 2 has a nanowire length L=3.1µm and a mean nanowire distance 500nm.The I-V characteristics of the cells are observed in the table of figure 1.13 *[7].*

Cell	1	2
wire pitch (nm)	400	500
J_{sc} (mA/cm^2)	**21.3**	**16.3**
V_{oc} (V)	**0.906**	**0.923**
Fill Factor (%)	**79.2**	**77.3**
V_{mpp} (V)	**0.767**	**0.791**
area (mm^2)	**1.084**	**1.073**
Efficiency (%)	**15.3**	**11.6**
wire length (μm)	2.8	3.1
~equivalent planar GaAs thickness[2] (nm)	370	270

Figure 1.13: Table with extracted parameters, evaluating the photo-response of axial GaAs nanowire solar cells *[7]*.

Optimization of nanowire solar cell performance

Doping profile

The introduction of dopants in nanowires can enhance the performance of nanowire solar cells. However, in contrast to thin films, doping in nanowires can influence the growth dynamics of nanowires. As a result, a balanced doping is needed to form high-quality and uniform nanowires *[14].*

Geometrical characteristics of nanowires.

The geometrical characteristics of nanowires plays a significant role in solar cell efficiency. Such geometrical characteristics are nanowire diameter, length and nanowire configuration. Initially, as far as nanowire diameter is concerned, the optimized value for a GaAs nanowire is between 150-180nm.The optimized value for nanowire diameter is determined by the bandgap energy of the material and its refractive index. Higher nanowire diameter than the optimized value leads to increased reflectivity of light at the top nanowire surface which increases losses. As a result, the light absorption is decreased. On the other hand, small values in nanowire diameter leads to insufficient light absorption at longer wavelengths. What's more, the nanowire length should also be optimized. As nanowire length increases, light absorption increase as well until the absorbance value reaches a saturation limit. Finally, as for the configuration of nanowires, it has been observed that vertical nanowires absorb sun radiation more effectively than the horizontal ones *[14].*

Recombination losses

It is important to reduce recombination losses for both axial and radial nanowire solar cells to achieve improved efficiency. Most photons are absorbed at the top of the nanowires in or close to the top segment of the p-n junction (emitter). So, minority carriers may recombine with majority carriers from dopant atoms in the emitter region or at the interface with the metallic contact. For this reason, a way should be found to reduce the recombination losses. One solution is doping the nanowire ends near the contact, reducing recombination at the contacts. Moreover, by reducing the thickness of the emitter layer, we can minimize the recombination losses in that region. As for example, it has been found that decreasing the emitter length in an InP nanowire solar cell from 360nm to 60nm increased J_{sc} by two orders of magnitude. Moreover, another solution is to incorporate an intrinsic region forming a p-i-n junction in the case of both radial and axial nanowire solar cells. In this way, recombination at the interface of the p-n junction can be reduced. As for radial nanowire solar cells, doping is demanded to ensure an effective depletion. Nevertheless, controlled doping is demanded regarding with the core and the shell thicknesses, controlling the material quality. What's more, passivation layers can limit recombination losses at the surface of nanowires *[14]*.

CHAPTER 2

Perovskite solar cells

Perovskite structure

Perovskites are materials that have a chemical type of the form: ABX_3 where X is an anion, A and B are cations. Cation A has a larger size than B. The composition of ABX_3 perovskite compound forms a cubic-like structure, as we can see from figure 2.1(a). The position of each ion in the cubic crystal lattice is particular. Especially, B cation is positioned in the center of the cubic structure of perovskite, X anions occupy face-centered cubic positions, while heavier A cations are placed at the corners of the cubic unit cell and their role is to stabilize the perovskite structure electrostatically. Moreover, as can be seen in figure 2.1, X ions form an octahedron where B ion is in the center of the octahedron.

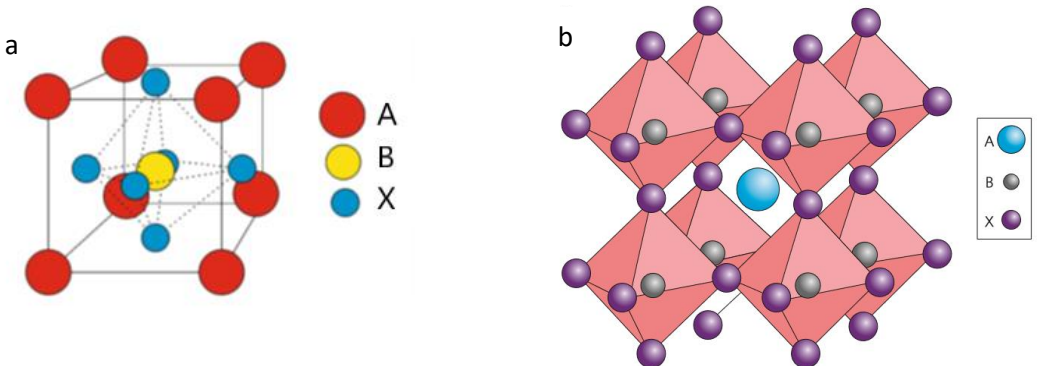

Figure 2.1: (a) Perovskite structure. (b) A different illustration of perovskite structure with cation A being at the center of the structure. X anions form octahedra around cation B *[26].*

The ions in the crystal lattice should have an appropriate radius, so as crystallographic stability is achieved. So, particular parameters are defined like the tolerance factor t and the octahedral factor μ, in order to estimate perovskite stability. The tolerance factor t is defined as the ratio of the distance A-X to the distance B-X. So, taking into account an idealized sphere model, we can define t from the relationship: $t = \frac{R_A+R_X}{\sqrt{2*(R_B+R_X)}}$ where R_A, R_B and R_X are the ionic radii of the corresponding ions A,B and X. As for the octahedral factor μ, it is defined as the ratio of the ionic radii R_B/R_X. In the case of halide perovskites where X: F, Cl, Br, I, the tolerance factor and the octahedral factor μ takes values: $0.81<t<1.11$ and $0.44<\mu<0.9$ respectively. For t values between 0.89-1.0 the cubic structure is likely to be formed. If the tolerance factor takes lower values, this means that the crystallographic structure tends to be less symmetrically tetragonal and it approaches the cubic and orthorhombic structure. So, only specific ions can form perovskite structure having a radius suitable for satisfying the restriction for tolerance factor t (and factor μ), which is determining for the formation of perovskite crystal structure. So, ions that are widely used and form perovskite structure for photovoltaic (PV) applications are the following: For cation A: methylammonium ($CH_3NH_3^+$) or formamidinium ($HC(NH_2)_2^+$) that are organic anions or cesium (Cs) that is inorganic, for cation

B: Pb, Sn and for X anions a halide is chosen (X: Br, Cl, I) *[26].* Because of the fact that both organic and inorganic ions are used, perovskites are called hybrid perovskites. Perovskites are widely used in PV applications, because they have numerous advantages. For example, they have excellent photoelectric properties, relatively low exciton binding energy and high absorption coefficients ($\sim 10^5$ cm^{-1}). Moreover, perovskite materials like $CH_3NH_3PbI_3$ ($MAPbI_3$) have low carrier recombination probabilities, high carrier mobilities, as well as long diffusion lengths and carrier lifetimes. For $MAPbI_3$, the diffusion length is at least 100nm. For these reasons, they can yield high photovoltaic efficiencies with a low cost of fabrication *[22],[26].*

Perovskite solar cells can be mainly divided into two categories. The Mesoscopic solar cells and the planar solar cells. The function of the perovskite structures has not fully been investigated, but there are many assumptions and possible mechanisms which can explain this kind of solar cell function. It is considered that the absorption of sunlight by the photoactive perovskite material produces excitons (that are electron-hole pairs). Due to the relatively low exciton binding energy in perovskite materials, these excitons can form free carriers (free electrons and holes) *[22]*. So, these charges are separated. In this way, the electrons are directed to the electron transport material (ETM), and similarly holes are oriented to the hole transport material (HTM), which directs them to a circuit. In this way, the electron-hole division and determined orientation results in the production of a photocurrent.

Types of Perovskite Solar Cells (PSCs)

Mesoscopic PSCs

Mesoscopic perovskite solar cell architecture has the following structure. Starting from the bottom, there is Fluorine doped Tin Oxide (FTO) electrode which coats a glass substrate, a compact TiO_2 layer, a mesoporous TiO_2 (or Al_2O_3), the perovskite active layer, a hole conducting material and finally the metal electrodes. A schematic illustration of the Mesoscopic structure is given in Fig. 2.2(a).

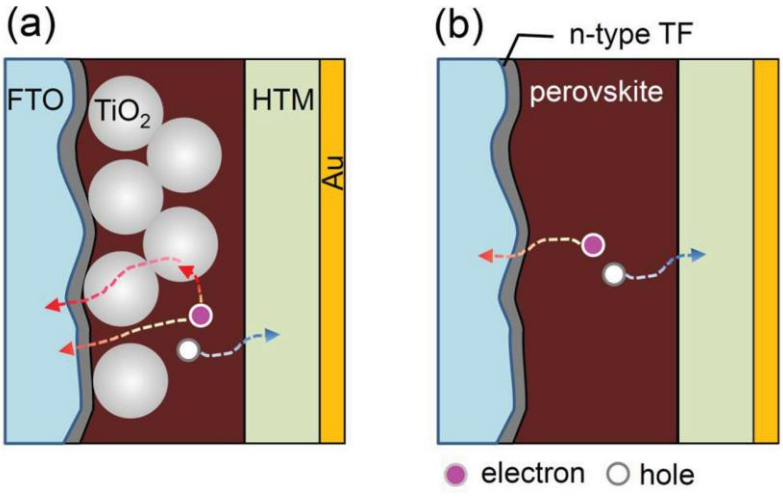

Figure 2.2: Mesoscopic structure compared with planar structure *[17]*

The functions of the above mentioned layers are the following: FTO is a Transparent Conducting Oxide (TCO), which has the role to direct the dissociated electrons into a conducting path to a circuit. The compact layer of titania (TiO_2), which is usually an n-type

doped semiconductor, functions as a blocking layer, by preventing the direct contact of the perovskite with FTO. In this way, the possibility for the holes existing in the perovskite or in the HTM to reach to the FTO electrode is eliminated. Thus, there is no creation of possible leakage current and the holes can only escape to the cathode. So, recombination is prevented to a great extent. The mesoporous TiO_2 layer which is an n-type semiconductor consists of pores, inside which perovskite material penetrates *[19].* This layer acts as a mesoporous matrix whose pores can be fully loaded with perovskite molecules, favoring effective perovskite coverage on the ETL surface and therefore enhancing perovskite growth *[24].* To elucidate on the ability of mesoporous metallic oxide layer to extract the electrons of the perovskite, which is in the layer pores and enhance the charge separation effect, we should bear in mind the energy states of the two materials. To be more specific, the oxide layer should have lower conduction band than the excited state of perovskite, so as the electrons to be transferred to the oxide layer. Titania extracts the electrons to the FTO then via the compact layer. What' s more, other metal oxides can be used as mesoporous layers apart from TiO_2, as for example zinc oxide (ZnO) and alumina (Al_2O_3) *[20].*

In addition, perovskite active layer is placed after the mesoporous layer. Subsequently, a layer of a Hole Transporting Material (HTM) is positioned. HTM is a p-type organic, polymeric or inorganic material *[21].* HTM functions as a hole extractor directing the holes to the cathode. The mechanism of hole extraction from HTLs is related with the energy state of the HTL. Particularly, the HOMO orbital of HTL is in a higher energy state than the valence band of perovskite. So, holes can be extracted by the HTL *[27].* HTMs are necessary to the perovskite solar cell device also, from the aspect that they prevent the back electron transfer and hinter the recombination with holes at the cathode layer. It has been noticed that the HTM layer choice can determine the J-V characteristics of the cell. Specifically, it increases open circuit voltage (V_{oc}) and fill factor values thereby enhancing solar cell efficiency (PCE) *[21],[23].* Below, there is a schematic illustration of a diagram which shows the energy levels of ETL, perovskite, HTL for indicative materials.

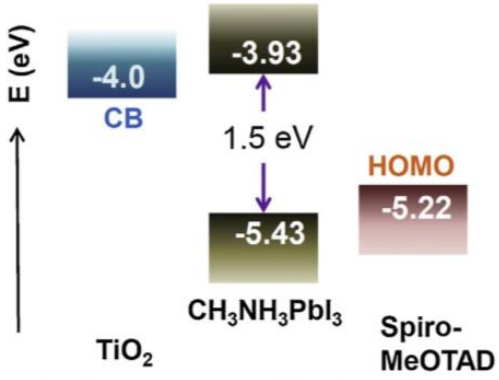

Figure 2.3: Diagram which shows the energy levels of TiO_2 (ETL), perovskite and Spiro-OMeTAD (HTLs) *[27].*

Next, an electrode is placed which collects the electrons from the external circuit and the holes transported by the HTM. Materials used for electrodes are noble metals such as

platinum, silver and gold. Noble metals and generally materials determined for electrodes should exhibit high conductivity for charge transport, good electro catalytic activity and high stability. However, a drawback for such materials (noble metals) is that they are very expensive *[28]*.

Planar perovskite solar cells

A planar perovskite heterostructure for photovoltaic devices in contrast to mesoscopic heterostructures does not include a mesoporous thin (oxide) layer. It has the following structure: FTO (as a Transparent Conducting Oxide-TCO)/Electron Transporting Material (ETM)/perovskite layer/Hole Transporting Material (HTM)/Metal electrode. This is a common planar heterostructure. There is also the inverted planar structure, which is the following: FTO (TCO)/HTM/perovskite/ETM/Metal electrode. Planar perovskite solar cells have demonstrated a PCE of over 15%. However, the lack of a mesoporous scaffold causes problems in perovskite film coverage and growth. Despite this, they can exhibit efficiencies even higher than mesoporous solar cells with an optimization of processing conditions and a careful control of the fabrication process *[24].* Below, a representative illustration of the two planar heterostructures (the common and the inverted one) are depicted compared to the mesoscopic structure.

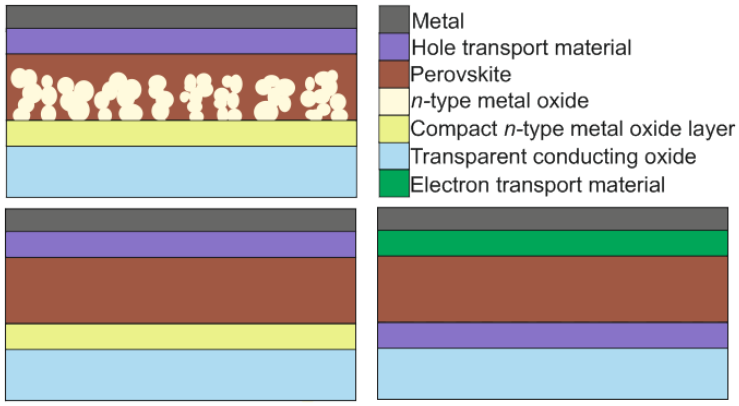

Figure 2.4: Perovskite solar cell structures: a mesoscopic (top), a planar heterojunction (bottom left), and an inverted perovskite (bottom right) solar cell.

An indicative planar perovskite solar cell structure is the one of:
FTO/ETM/$MAPbI_2Cl$/PEDOT:PSS/Ag *[22].* Below, a schematic diagram and SEM images are shown for both structures:

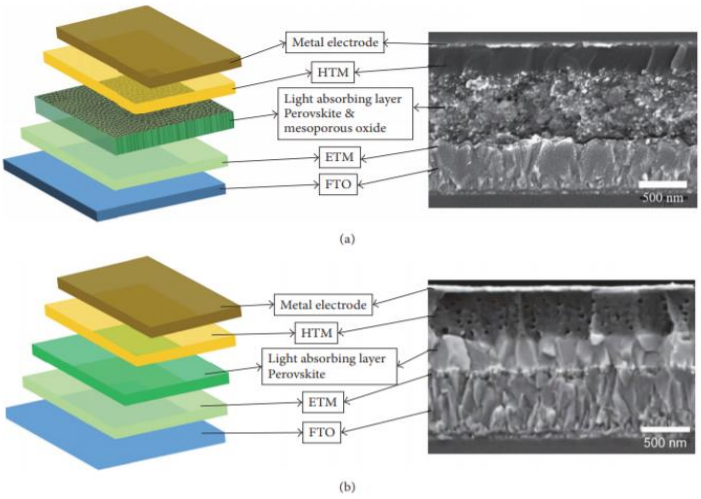

Figure 2.5: SEM images of two indicative types of PSCs structures, the Mesoscopic and the Planar ones *[22].*

Hole Transporting Layer (HTL)

The materials used as hole transport layers (HTLs) play a significant role in solar cell performance. As mentioned previously, HTLs collect and transport holes from the perovskite material leading them to an electrode which is connected with the electrical circuit. Two types of HTLs can be used: organic and inorganic hole transporting materials. One of the most commonly used material as organic HTL is Spiro-OMeTAD, due to the effective matching achieved with the valence band energy of the perovskite. Despite this advantage, the hole mobility is not as high as the one of other organic HTLs. For this reason, p-type doping is enhanced on Spiro-OMeTAD. HTLs with p-type composites such as cobalt compounds or some additives (e.g. bis (trifluoromethane) sulfonamide lithium, LiTFSI and 4-tert-butyl pyridine, TBP) are also used in order to improve the hole mobility of the HTL. In addition, polymer hole transporting materials have attracted more interest due to their better film forming ability of the layer and their higher hole mobility. Commonly used polymer materials as HTLs are PTAA (poly[bis (4-phenyl)(2,4,6-trimethylphenyl)amine), since hole mobility in such materials is one to two orders of magnitude higher than that of other HTLs. Other polymer HTLs are: P3HT, PEDOT:PSS, PCDTBT, PCPDTBT. It has been noticed that the presence of P3HT can reduce the resistance from the HTL, thus improving the stability and the performance of the devices. PEDOT:PSS polymer material is currently being investigated, because it is easy to form the layer by spin-coating. It is also designated for flexible perovskite solar cells.

Contrary to organic HTLs, there are also inorganic ones , such as CuSCN, CuI, NiO, $CsSnI_3$, which are p-type semiconductors and they effectively improve the conductivity in solar cells, as well as the fill factor parameter, which is determinant for PCE effectiveness *[22]*.

Preparation methods

The perovskite production methods that can be used are one-step coating and two steps coating methods. To be more specific, one step coating method includes perovskite formation on a substrate in one step. The techniques used for one step solution process can be solution techniques or thermal evaporation techniques. As for the one step solution technique, both constituents of the precursor solution as for example CH_3NH_3I and PbI_2 are dissolved in an appropriate solvent (such as a polar aprotic solvent like N,N-dimethylformamide (DMF), gammabutyrolactone (GBL) or dimethyl sulfoxide (DMSO). So, the solution of CH_3NH_3I and PbI_2 dissolved substances can be dropped on the substrate and form a coating solution. Then spin coating, drying and annealing processes follows. In this method, both the solution and the substrate should be heated. For this reason, this solution method is called otherwise hot-casting. As far as thermal evaporation technique is concerned, both components of perovskite structure are heated at different temperatures under vacuum conditions and the vapor of the substances are simultaneously deposited on the substrate, through a dual source of vapor. The thermal evaporation by vacuum method seems to be better than the solution process, because better uniformity of the film is achieved and the thickness of the film can be under control *[24],[18].*

As for the two-step coating method or otherwise named as sequential solution processing technique, the inorganic component (e.g. PbI_2) is first deposited on the substrate and after that the substrate is thermally annealed. The second component, the organic part of the reaction can be either: (i) deposited via spin-coating on the substrate, (ii) it can be in the form of a dipping solution or (iii) it can be in the form of vapor. In case (i), both the organic and inorganic parts are spin-coated on the substrate sequentially. After spin-coating, thermal annealing follows. In case (ii), we first have inorganic part deposition (e.g. PbI_2) on the substrate. After thermal annealing, the substrate is dipped in the organic (e.g. CH_3NH_3I) solution. The dipping solution incorporates a solvent that does not dissolve the inorganic component. So, a reaction takes place between the organic and the inorganic constituents, so perovskite layer is formed. At a last stage, thermal annealing of the sample follows. In case (iii) the perovskite is formed after exposing the organic (MAI) vapor on the substrate at an elevated temperature, on which the inorganic (e.g. PbI_2) layer was deposited. In the following figure (fig. 2.6), an illustration of the two kinds of preparation methods for perovskite solar cells is shown, as they are described above *[24].*

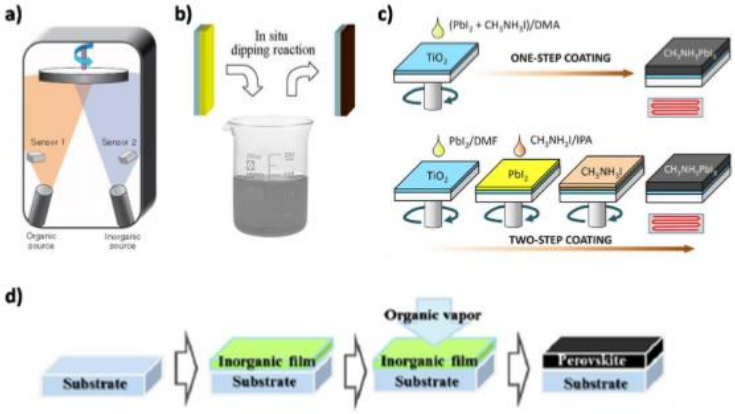

Figure 2.6: Preparation processes: (a) Thermal evaporation method for perovskite formation in one step. (b) Two-step method via dipping PbI_2 deposited substrate in MAI solution. (c) One-step and sequential solution process. (d) Sequential process via organic vapor deposition on an inorganic substrate *[24].*

If we compare the two above-mentioned methods, we have to say that the two-step coating method ensures higher efficiency of the perovskite solar cells than the one-step coating method. That can be attributed to the fact that with the second described method, the morphology and the interface between the films deposited are better formed with better homogeneity than the first described method. So, one basic criterion taking into account for high efficiency perovskite solar cell construction is morphology control. Moreover, we should bear in mind other preparation conditions, as well, during the perovskite solar cells fabrication such as spinning rate and time, temperature, solution wettability and viscosity etc.

Two-step method

In the two-step method, the perovskite $CH_3NH_3PbI_3$ ($MAPbI_3$) is formed in two steps: Initially, the first reactant for the formation of perovskite that is PbI_2 is spin-coated on the substrate. After drying, the film is dipped in CH_3NH_3I (MAI) solution that constitutes the other component of the reaction. During dipping, PbI_2 is transformed to the perovskite phase. The formation of perovskite and its crystal structure depends on the dipping time in the MAI solution. According to a report, different films were studied with varying dipping time between 5sec to 2h. Then, complete solar cell devices were fabricated and were electrically characterized. The configuration of these devices was: FTO/compact TiO_2/mesoporous TiO_2/perovskite/Spiro-OMeTAD/Au. Characterization results showed that an increase in dipping time from 5s to 15min resulted in an increased current density and open circuit voltage (V_{oc}). The optimum values were J_{sc}= 15.1Ma/cm^2, V_{oc}= 1.036V, with a conversion efficiency of 9.7% corresponding to a 15min dipping time. However, at higher dipping times the solar cell performance decreased. Particularly, after a 2h dipping time the current density decreased to 9.7 mA/cm^2 and V_{oc} decreased to 846 mV. Therefore, the degree of conversion of PbI_2 to $MAPbI_3$ is set as a significant parameter for high efficiency, rather than the full conversion to the perovskite compound *[42].*

X-ray diffraction spectra were taken from samples with varying dipping times (Figure 2.7).

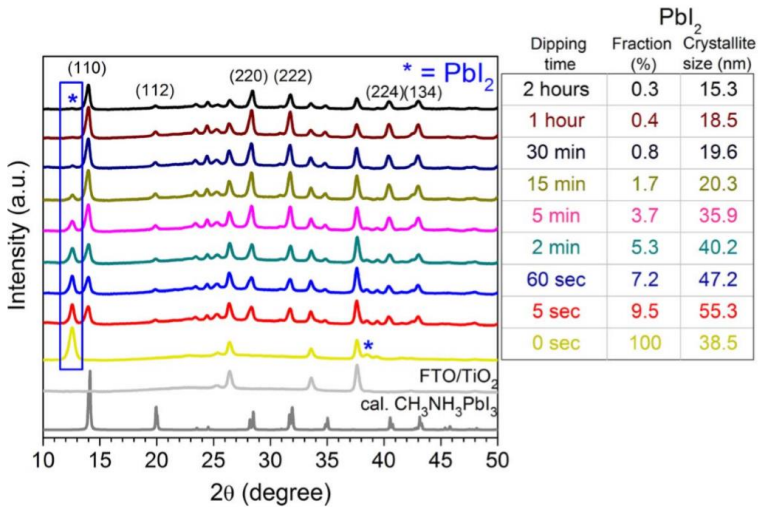

Dipping time	PbI2 Fraction (%)	PbI2 Crystallite size (nm)
2 hours	0.3	15.3
1 hour	0.4	18.5
30 min	0.8	19.6
15 min	1.7	20.3
5 min	3.7	35.9
2 min	5.3	40.2
60 sec	7.2	47.2
5 sec	9.5	55.3
0 sec	100	38.5

Figure 2.7:X-ray diffraction spectra for samples with different dipping times. The dipping time varied between 0sec and 2h *[42].*

From X-ray diffraction spectra, we can see that only the β-phase of perovskite was formed, independently of the dipping time. In addition to this, unconverted PbI_2 is present as well. The

PbI_2 peaks in the X-ray diffraction spectra are marked with *. The presence of PbI_2 is confirmed via the (001) and (003) reflections at $2\theta = 12.56^o$ and 38.54^o respectively. We notice that as the dipping time increases, the PbI_2 peak intensity decreases, while that of $MAPbi_3$ peak increases. Moreover, the PbI_2 peak width increases as well. This indicates a decrease in the grain size of PbI_2 and an increase in $MAPbI_3$ grain size. So, according to this observation it can be suggested that the conversion of PbI_2 to $MAPbI_3$ starts from the surface of the PbI_2 crystallites and proceeds to the center where crystallites of $MAPbI_3$ phase increases, while that of PbI_2 diminishes.

In figure 2.8, we can see the absorption spectra of $MAPbI_3$ films as a function of the fraction of unconverted PbI_2. Pure PbI_2 has a bandgap Eg=2.4eV that is consistent with the PbI_2 absorption spectrum (yellow spectrum).

As the fraction of PbI_2 decreases and therefore PbI_2 is converted to perovskite, the bandgap energy is decreased from Eg=2.4eV to 1.6eV. This shift can be observed by the absorption spectra. The $MAPbI_3$ bandgap appears at 1.6eV, which deviates from the conventional value of 1.55eV possibly due to the presence of quantum confinement effects that are related with the grain sizes of TiO_2 and $MAPbI_3$ crystallites and their interfacial interactions. In the absorption spectra, we also notice a second absorption shift. There is a red-shift of the energy bandgap from 1.9 to 1.5 eV that correspond to 9.5% and 0.3% remnant PbI_2 respectively.

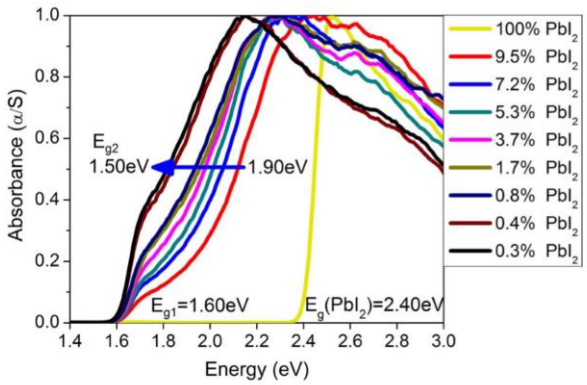

Figure 2.8: Absorption spectra of $MAPbI_3$ corresponding to different fractions of unconverted PbI_2 *[42].*

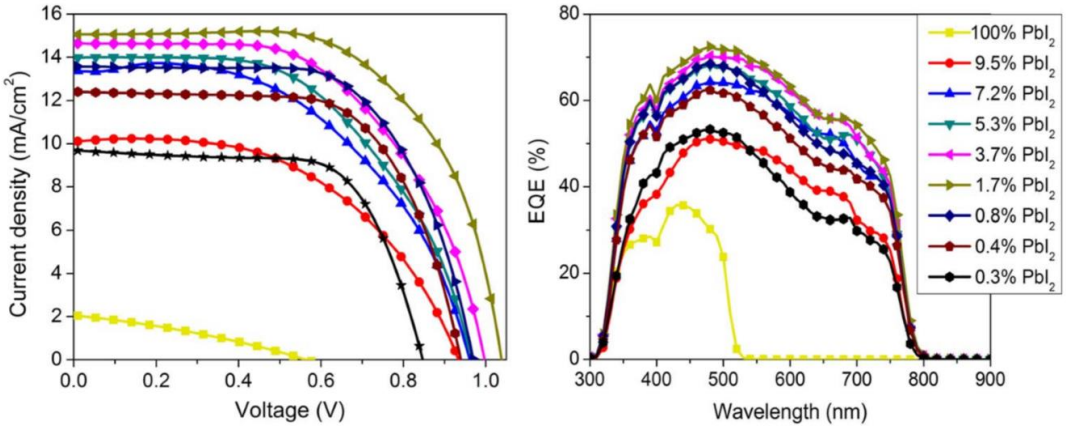

Figure 2.9: (a) Photo J-V curves and (b) EQE of $MAPbI_3$ devices as a function of the remnant PbI_2 fraction *[42]* .

Based on the experimental results (Figure 2.9), we can correlate the current density and the V_{oc} values with the fraction of the remnant PbI_2 for the films studied. As we can see from figure 2.10, two regions can be distinguished. The first region shows an increase in the J_{sc}, V_{oc} values as the remnant PbI_2 fraction decreases to 1.7%. The other region shows a decline in these

values with a further decrease in the fraction of the remnant PbI_2. As far as the first region is concerned, the increase in J_{sc} can be attributed to the enhanced absorption due to the increase in perovskite absorbing layer thickness. Moreover, the elimination of PbI_2 favors electron injection from perovskite to the TiO_2 ETL, since PbI_2 layer may act as a barrier hindering the electron transport to the ETL. Moreover, the increase in V_{oc} is attributed to the positive shift in the quasi-Fermi level of TiO_2 due to the increase in photo-injected electrons. As far as the second region is concerned, by further decreasing the PbI_2 concentration the decrease in J_{sc} and V_{oc} can be attributed to the PbI_2 layer thickness. Particularly, the remnant PbI_2 acts as a blocking layer, preventing the back transfer of electrons from the TiO_2 to the perovskite. As a result, the recombination of the electrons with holes either in the perovskite material (charge recombination) or the HTL (charge interception) is limited. In other words, the remnant PbI_2 hinders charge recombination.

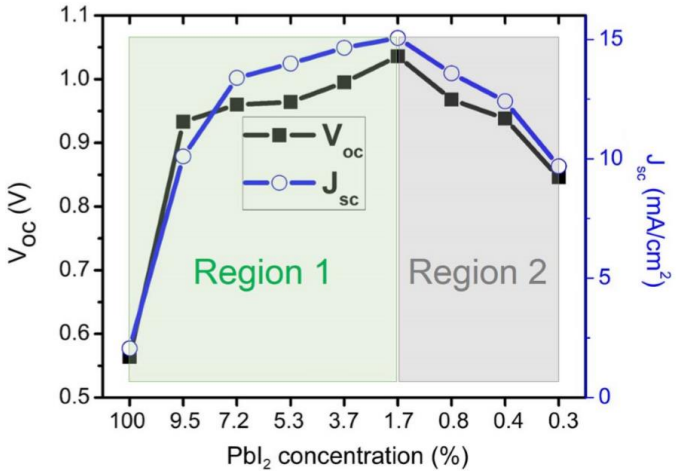

Figure 2.10: Current density and open-circuit voltage as a function of the unconverted PbI_2 concentration *[42]*

To verify the role of PbI_2 as a blocking layer, we consider that the PbI_2 layer is sandwiched between the TiO_2 and the perovskite. So, PbI_2 can act as a blocking layer, provided that the conduction band edge of PbI_2 is higher than that of TiO_2. As we can see in figure 2.11, the conduction band edge of PbI_2 is 0.26eV higher than that of TiO_2.Therefore, we infer that this suggestion is correct.

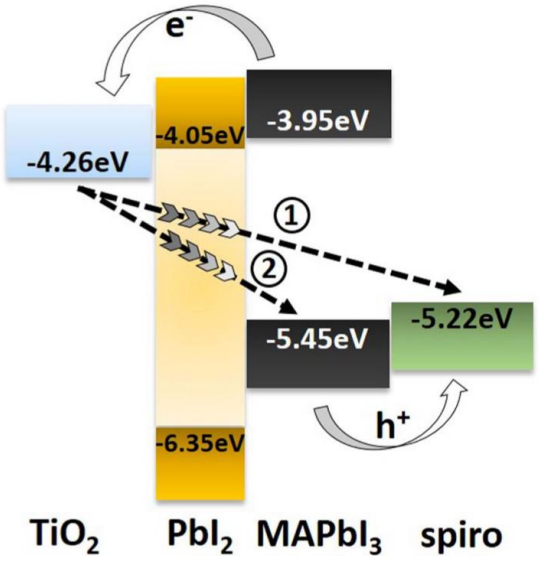

Figure 2.11: Model of charge-interception/recombination retardation by the unconverted PbI_2 layer in $MAPbI_3$-based solar cells *[42]*

Moreover, the ability of PbI_2 to act as a blocking layer can be verified by dark I-V measurements, which refer to electrons flow from TiO_2 to the HOMO of the HTL. It was noticed that as the dipping time increases, the dark current increases while voltage values get lower. According to this, someone would expect that the open-circuit voltage value would decrease as the remnant of PbI_2 fraction gets lower. Instead, the photocurrent density and the open-circuit voltage are both increased until a fraction of 1.7% of remnant PbI_2 is achieved. Consequently, as the perovskite thickness increases, net-injection yield is higher, but at high dipping times for which the PbI_2 layer is very thin there are significant recombination losses, so PbI_2 does not act as a blocking layer. In Figure 2.12, dark I-V curves are illustrated which relate to the various dipping times.

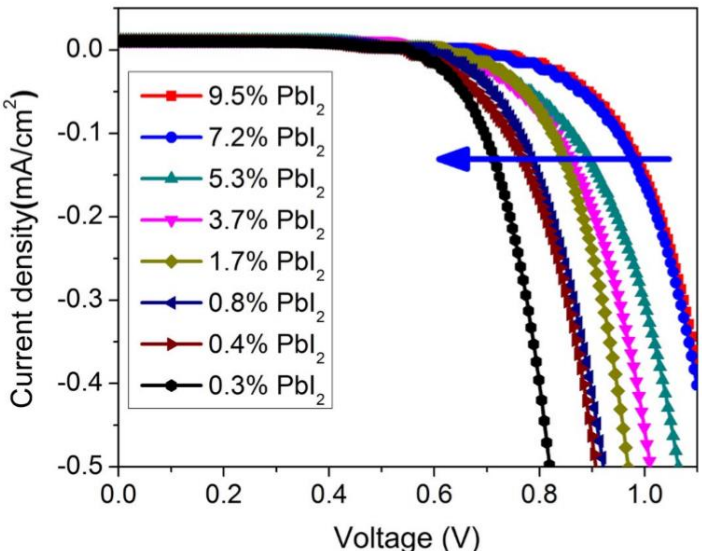

Figure 2.12: Dark I-V curves of $MAPbI_3$ solar cell devices as a function of unconverted PbI_2 phase fraction *[42].*

In figure 2.13, we can see SEM images which show the structure of perovskite at different dipping times. As we can see from the SEM images there are two structural regions. The first region (area1) included TiO_2 network/perovskite as well as the remnant PbI_2 layer. Whereas, the other region (area 2) includes solely the perovskite phase that has grown above area 1. The area 2 initially contains 200nm thickness. The perovskite crystal becomes larger and with different morphology as dipping time increases. However, at high dipping times, small perovskite crystals dissolve and re-deposit onto larger perovskite crystals. So, at higher dipping times the contact area between the perovskite and the HTM gets larger. So, recombination (interception) phenomena between the perovskite and the HTM layer are favored, since the possibility of carrier recombination-interception increases. Therefore, at smaller dipping times where the remnant PbI_2 layer is still apparent recombination (interception) phenomena at the interface between the perovskite and the HTL are limited, a fact which indicates the role of remnant PbI_2 to act as a blocking layer *[42]*.

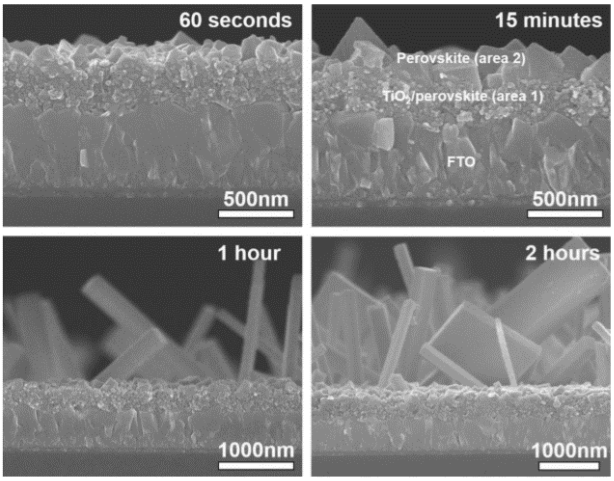

Figure 2.13**:** Cross-section SEM images of $MAPbI_3$ film with different dipping time *[42]*

In figure 2.14, the I-V characteristics are shown for the different fractions of unconverted PbI_2.

Dipping time	PbI_2 concentration[a]	J_{sc} (mA/cm^2)	V_{oc} (V)	Fill factor (%)	Efficiency (%)
0 s	100%	2.1	0.564	32	0.4
5 s	9.5%	10.1	0.933	52	4.9
60 s	7.2%	13.4	0.960	52	6.7
2 min	5.3%	14.0	0.964	55	7.4
5 min	3.7%	14.7	0.995	57	8.3
15 min	1.7%	15.1	1.036	62	9.7
30 min	0.8%	13.6	0.968	64	8.5
1 h	0.4%	12.4	0.938	65	7.6
2 h	0.3%	9.7	0.846	68	5.5

Figure 2.14: I-V characteristics of samples with different fractions of unconverted PbI_2 *[42]* .

For perovskite film formation, various precursor solvents are used. Such precursor solvents are: dimethylformamide (DMF), gamma-butyrolactone (GBL), methyl-2-pyrrolidinone (NMP), dimethylsulfoxide (DMSO), DMF-DMSO, GBL-DMSO, and NMP-DMSO. These precursor

solvents can influence solar cell properties like quantum efficiencies, charge transport behaviors, intermediate-phase formation of the perovskite compound and perovskite film morphology. Speaking for p-i-n type planar perovskite solar cells, different studies have been made to evaluate the degree of influence of different solvents on solar cell performance. An indicative geometry of planar solar cells which was investigated (according to a study) is the following: indium tin oxide/nickel oxide (NiO_x)/ $CH_3NH_3PbI_3$ perovskite/[6,6]-phenyl-C_{61} butyric acid methylester ($PC_{61}BM$)/bathocuproine (BCP) and Ag. Different solvents have been used for perovskite composition.

According to investigations in the particular work, DMF and GBL solvents exhibited highly inhomogeneous and incomplete surfaces of the perovskite films with many voids. The main cause of this poor perovskite morphology is attributed to the solubility difference of the solution constituents that are CH_3NH_3I (or MAI) and PbI_2. The solubility difference induces a different growth rate, between MAI and PbI_2, leading to inhomogeneous growth. What's more, the solvents evaporation rate is faster than NMP and DMSO, leading to less uniform solutions. In contrast to DMF and GBL solvents, NMP, DMSO, GBL-DMSO and NMP-DMSO showed an improved solar cell performance and the perovskite surfaces were relatively flat and uniform. As far as DMSO is concerned, it showed a better solar cell response, due to a better perovskite film uniformity and a more stable intermediate-phase for perovskite film formation. This solvent behavior is due to the relatively low evaporation rate of DMSO compared to DMF and GBL *[18].* Moreover, improved film uniformity can be attributed to the capability of DMSO to produce a precursor solution with constituents in high concentrations, thereby favoring dense films fabrication, in comparison with other solvents like DMF *[24].* Finally, DMF/DMSO combination of solvents showed even better perovskite film formation with the largest grains, in comparison with the other solvents referred. So, DMF-DMSO based planar solar cells exhibited the best efficiency of 15.05%. Below, SEM images are illustrated, where perovskite film structure is shown, using different precursor solvents *[18].*

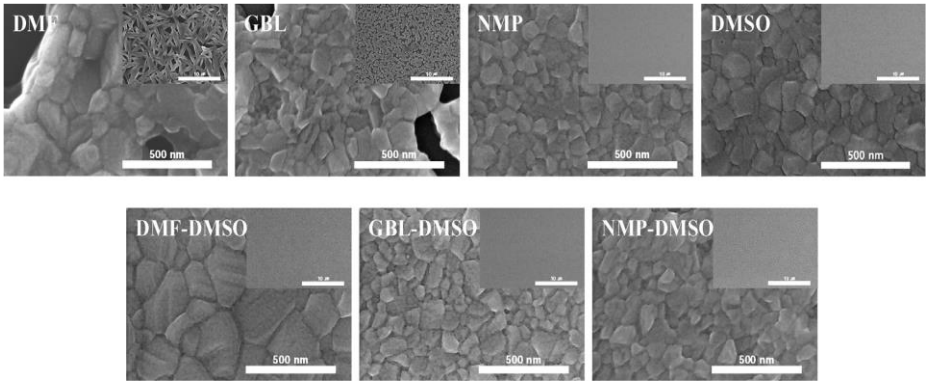

Figure 2.15: The SEM images of $CH_3NH_3PbI_3$ films fabricated using different solvents. Insets are an enlarged SEM image of the corresponding SEM images with scale bars of 10 nm *[18].*

Another "solvent" that can be used is chlorobenzene. After spinning the precursor solution in DMF, when the substrate is even wet, chlorobenzene is added. Chlorobenzene is in fact an "anti-solvent", which reduces the solubility of perovskite materials in DMF solvent. Reduced solubility entails rapid crystallization (that is fast nucleation/growth of crystals) in the film. So, a flat and a uniform film is formed with grain sizes up to microns *[24]*.

Moreover, a mixed solvent of γ-butyrolactone and dimethylsulphoxide (DMSO) was used followed by toluene drop-casting. This technique led to extremely uniform and dense perovskite layers. DMSO is used to reduce the solubility of the solution by retarding the rapid reaction between PbI_2 and CH_3NH_3I (for $CH_3NH_3PbI_3$ perovskite PV formation), thereby forming an intermediate compound of CH_3NH_3I-PbI_2-DMSO. After the creation of this compound, toluene is used to remove excess DMSO solvent from the wet film. However, rapid crystallization results in the formation of different crystal sizes (on the hole-blocking layer), thus leading to inhomogeneity in grain size and stoichiometry. However, homogeneity of the grain sizes can be achieved by submitting the perovskite layer to annealing at 100^0C. As a result, flat homogeneous perovskite layers are fabricated *[18],[24].*

In general, using specific substrates/solvents, rapid crystallization can be achieved, which means that crystal grains can be nucleated fast. However, rapid crystallization entails inhomogeneity in crystal grain sizes. We can remedy this and fabricate homogeneous layers by annealing the films (at 100^0C). So, we can create flat, thin, uniform films which entails high perovskite solar cells performance *[18],[24].*

Phase transition in perovskite structure

Methylammonium (MA:$CH_3NH_3^+$) based halide perovskite materials can undergo a phase transformation in the structure of the perovskite with temperature. Owing to its low lattice energy, and weak atom bonding, there is a motion of methylammonium molecule ($CH_3NH_3^+$) along the C-N axis. The degree of methylammonium rotational motion was investigated using ^1H and ^{14}N NMR spectra. As the temperature increased, rapid rotation has been notified and this motion was restricted significantly as the temperature decreased. The structural phases which occur with temperature drop is cubic→tetragonal→orthorhombic and they occur owing to confined molecular motions which result in a more ordered organic cation of the molecules along the C-N axis *[1].* For $CH_3NH_3PbI_3$, we have: (a) an orthorhombic to tetragonal phase transition at a temperature of 162K (-111,15^{0}C) and (b) a tetragonal to cubic phase transition at 327K (54^{0}C) *[25].*

Flexible perovskite solar cells

Flexible thin film solar cells are suitable for various potential applications, like portable electronic chargers and bendable display devices, because of their high bendability, light weight, as well as easy shape modulation. Flexible perovskite solar cells present a wide interest nowadays, because they can be very efficient and materials are used that demand low temperature conditions for their preparation (below ~ 150 ^{0}C). But still, flexible perovskite solar cells are in a development stage.

For flexible perovskite solar cells ITO-coated poly (ethylene terephthalate) (PET) substrates can be used. PET is a polymer which has thermoplastic properties. So, its shape changes under heat or pressure and it is also light weight. On these substrates, p-i-n structures are composed of PEDOT:PSS/perovskite/PCBM architectures (as can been seen in fig. 2.16).

The advantage of using such materials as transporting layers, such as PEDOT:PSS and PCBM is that they are able to be deposited at low temperature (below 150^0C), which makes the fabrication of flexible solar cells feasible. On the contrary, if ETM such as a TiO_2 compact layer were used for the fabrication of flexible solar cells, according to the conventional method, high temperatures (over ~400^0C) would be demanded for its preparation and thus the solar cell fabrication would be impossible. Speaking for flexible solar cells, they can also be formed by a

n-i-p structure (planar structures) consisting of ZnO ETM deposited on a substrate at a low temperature. (Particularly, ZnO materials can be deposited at a temperature below 150^{0}C). Generally, it has been investigated that an n-i-p structured flexible perovskite solar cell can achieve a power conversion efficiency (PCE) of 10.2%.

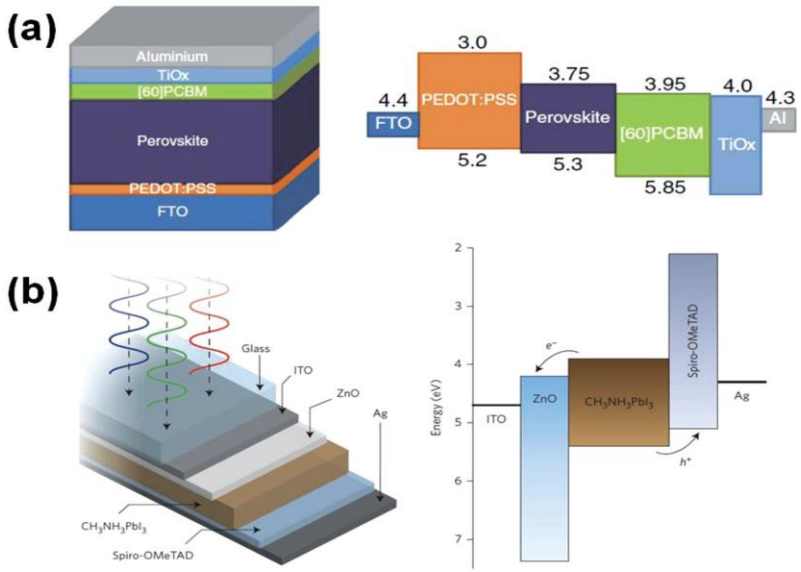

Figure 2.16: Structure for flexible PSCs *[17]*

Moreover, high efficiency flexible solar cells can reach a PCE over 12% by using a TiO_x compact layer deposited using atomic layer deposition (ALD).It has been noticed that such materials are very resistant. Their PCE does not change after 1000 cycles of bending. So, these materials can be used for flexible solar cells.

Long-term stability

Despite many advantages and significant properties of flexible perovskite solar cells, a very important issue that has not been entirely solved is the long term stability issue. After a long period of time, a degradation mechanism on solar cells operation has been noted. For dealing with this problem, many efforts have been made. For example, P3HT/single-walled carbon nanotubes (SWCNT)-PMMA double layer has been used as an HTM. By using this double layer, remarkable thermal and moisture stability has been observed. Comparing this P3HT polymer-based HTM with a single-molecule based spiro-OMeTAD as materials used in perovskite solar cells, the use of the former showed an increased stability of perovskite PVs compared to the latter. However, the PCE dropped to 20% of initial efficiency after heating the cell at 80^{0}C for 20 min (with a temperature coefficient of ~0.33%/^{0}C) *[17]*.

CHAPTER 3

Hybrid Nanowire/perovskite solar cells

The theme of the present thesis is hybrid GaAs nanowire/perovskite solar cells. In the present work, GaAs nanowires are used as an electron transporting material (ETM) in perovskite solar cells, replacing conventional electron transporting materials like titanium dioxide (TiO_2). The role of GaAs nanowires is to extract electrons that are generated by the perovskite material. In this chapter, I will focus on the optical and electrical properties of both polycrystalline TiO_2 and crystalline GaAs and explain the reasons why GaAs nanowire structures would be a better choice for using them as an ETM.

3.1 Electrical and optical properties of polycrystalline TiO2

Titanium dioxide (TiO_2) or otherwise titania can be single crystalline or polycrystalline. Polycrystalline TiO_2 is used as electron transporting material (ETL) in solar cell applications. Polycrystalline material is a material that consists of separate domains (grains) of crystalline material. The interface between the grains is called a grain boundary *[35].* The existence of grain boundaries determines the quality of crystalline materials. TiO_2 has three natural crystal structures: rutile, anatase and brookite, as shown in the following figure:

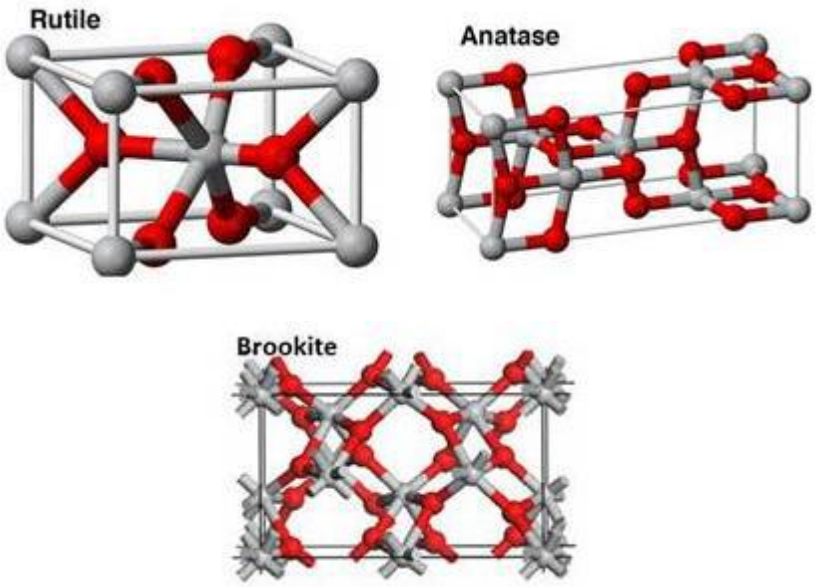

Figure 3.1: Crystal structures of rutile, anatase and brookite. Titanium atoms are depicted as grey spheres, while oxygen atoms are depicted as red spheres [39].

Rutile is considered to be the most stable of the three structures. It is also chemically inert. It can be excited by visible and ultraviolet light. The other two structures that are brookite and anatase are metastable formations of titania. Anatase can be excited only by ultraviolet light and it turns into rutile by heating. Anatase or rutile forms are used in mesoscopic solar cells and rutile structure has higher electron diffusion coefficients and lower electron recombination *[39].*

TiO_2 is an n-type semiconductor. It is used as an ETL, since band alignment is fulfilled between TiO_2 LUMO orbital with the conduction band of perovskite. Therefore, electrons that are generated in the perovskite absorbing material can be extracted to TiO_2.The energy diagram which indicates the band alignment of TiO_2 with perovskite is shown in the figure 3.2 *[27].*

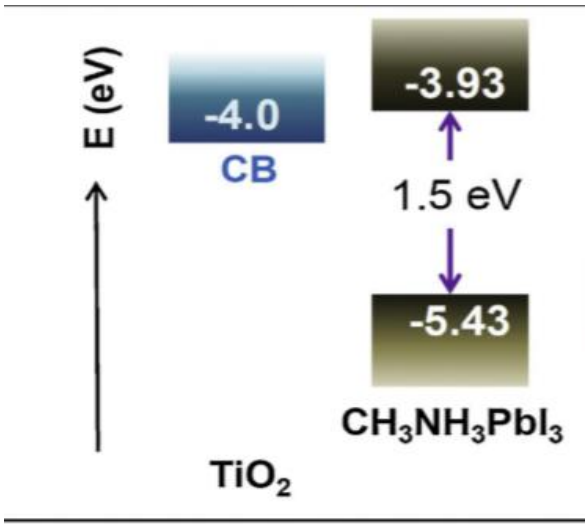

Figure 3.2: Energy diagram which shows the energy levels of TiO_2 with perovskite. The conduction band of TiO_2 (LUMO orbital) is energetically lower than the conduction band of perovskite thereby favoring band alignment *[27]*.

TiO_2 has a bandgap energy $E_g = \sim 3eV$. Due to its high bandgap energy, TiO_2 has electrochemical-photocatalytic properties. Nevertheless, TiO_2 is a very stable material, resisting to photo-decomposition *[38].*

Parameters that determine the electrical properties of TiO_2 are electrical conductivity and mobility of electrons and holes, under the application of an external electric field.

Electrical conductivity σ is expressed by the formula:

$$\sigma = e * (n * \mu_n + p * \mu_p) \quad (eq. 3.1)$$

Where μ_n ,μ_p: mobility of electrons and holes respectively
n, p: concentrations of electrons and holes respectively
e: the electronic charge *[33]*

Mobility of electrons and holes expresses the ease of carrier motion in the semiconductor crystal lattice. It is defined as:

$$\mu = \frac{\bar{v}}{E} \quad \text{(eq.3.2)}$$

Where $\bar{v}$ is the average drift velocity of the carriers under the influence of the electric field $\vec{E}$.

$$\bar{v} = \frac{q*\tau_c}{m^*}\vec{E} \quad \text{(eq.3.3)}$$

Where τ_c: mean free time between carrier collisions
m*: carrier effective mass

Therefore, mobility is defined as *[29,31,34]* :

$$\mu = \frac{q*\tau_c}{m^*} \quad \text{(eq.3.4)}$$

Carrier mobility values can be extracted by eq. 3.1. So, both values for electrical conductivity and carrier concentration should be determined. Electrical conductivity and concentrations of electrons and holes depend on the existence mainly of oxygen defects and other defects in the crystal lattice. Examples of defects can be oxygen vacancies, titanium vacancies, titanium interstitials, as well as electronic defects. Therefore, the electrical properties of TiO_2 depend on defects in TiO_2 lattice and can be modified based on the defect concentration in the crystal lattice *[33]*.

In figure 3.3, we can see a diagram which illustrates mobility of electrons and holes as a function of temperature, in the case of high-purity single crystalline (SC) and polycrystalline (PC) TiO_2.

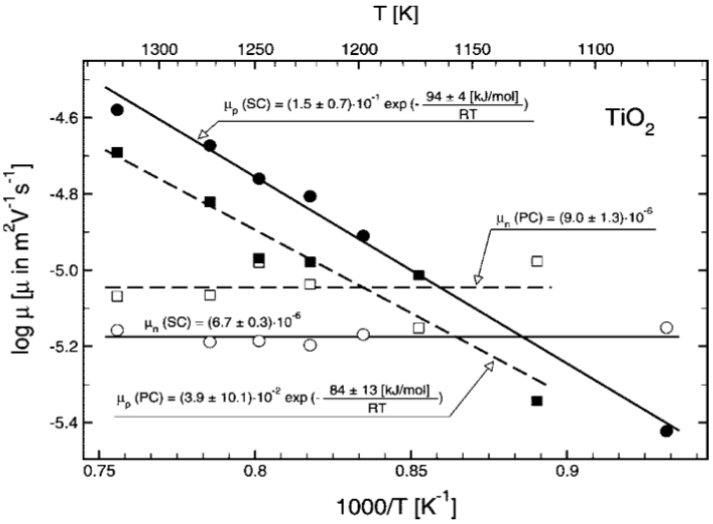

Figure 3.3: Carrier mobility as a function of temperature, for single crystalline (SC) and polycrystalline (PC) TiO_2 [33].

As for polycrystalline TiO_2 which is of interest in our case, electron and hole mobility at room temperature is *[33]*:

$$\mu_n(TiO_2/PC) = (9.0 \pm 1.3) * 10^{-6}\ (m^2 * V^{-1} * s^{-1})$$

$$\mu_p(TiO_2/PC) = (3.9 \pm 10.1) * 10^{-2} * \exp\left(-\frac{84 \pm 13\left(\frac{kJ}{mol}\right)}{R*T}\right) (m^2 * V^{-1} * s^{-1})$$

Where $RT=N_A*k_B*T$ in units J/mol

k_B : the Boltzmann constant and N_A: the Avogadro constant.

So, we can estimate mobility values for polycrystalline TiO_2 at 300K as follows:

$\mu_n(TiO_2/PC) = 0.09\ (\frac{cm^2}{V*s})$, $\mu_p(TiO_2/PC) = 7.5 * 10^{-13}(\frac{cm^2}{V*s})$, which is negligibly small.

3.2 Electrical and optical properties of crystalline GaAs

GaAs semiconductor is a III-V semiconductor of direct bandgap. It has zinc blende crystal structure, as can be seen in figure 3.4 *[29],[30].*

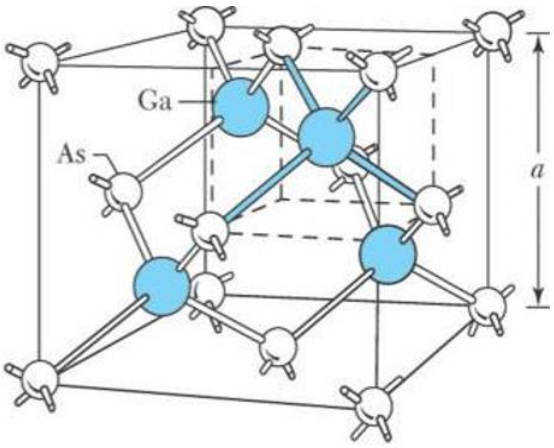

Figure 3.4: Zinc blende crystal structure of GaAs *[37].*

GaAs has such electrical and optical properties, that render it a suitable material for optoelectronic applications, especially in solar cells. Such properties are optimum bandgap energy, high absorption coefficient, low non-radiative energy losses, which means that energy losses due to non-radiation recombination are limited. Moreover, GaAs has very high electron mobility, high thermal stability and relatively high values in carrier lifetimes. However, the fabrication of single crystalline GaAs has a high cost of fabrication *[32].*

To elaborate more on GaAs properties, some optical characteristics of GaAs are the following: GaAs has a bandgap energy of 1.42eV. Also, it has electron affinity of 4.07eV *[29],* which is similar to TiO_2. In figure 3.5(a), we can see the energy diagram of GaAs bands. GaAs has a conduction band energy significantly lower than the conduction band of perovskite ($CH_3NH_3PbI_3$) (190meV) and therefore band alignment is favored. This means that electrons which are generated by the perovskite can easily be collected by GaAs semiconducting material. Therefore, GaAs can be used as an electron transporting material (ETM) in perovskite solar cells. In figure 3.5(b), we can see schematically the band energy levels for GaAs and the perovskite $CH_3NH_3PbI_3$. The energy levels of GaAs were positioned taking into account GaAs electron affinity and its bandgap energy *[29]*.

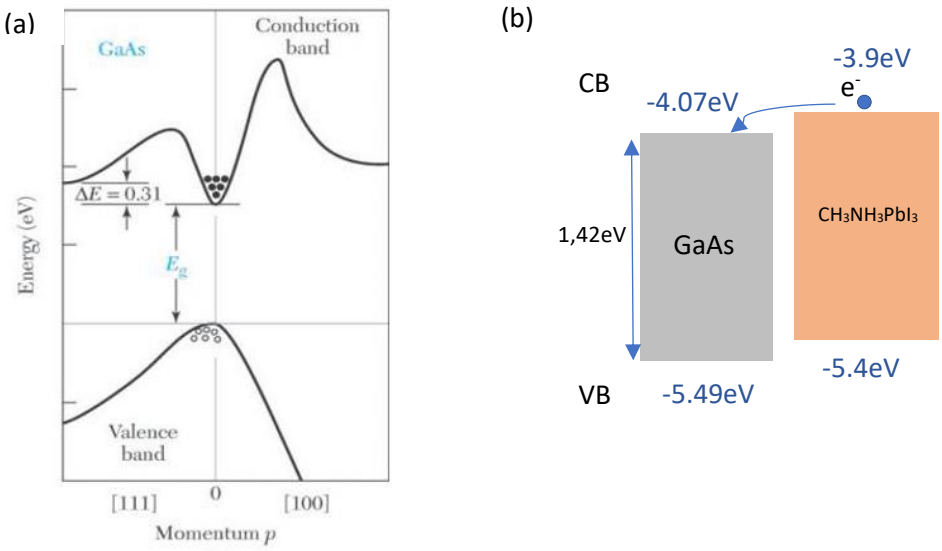

Figure 3.5: (a)Energy diagram of bands for GaAs. GaAs is a direct semiconductor, since conduction band (CB) maximum and valence band (VB) minimum occur at the same momentum (p=0) *[37].* It has a bandgap energy of Eg=1,42eV. (b) Schematic representation of the energy levels, CB and VB for GaAs and Homo-Lumo for $CH_3NH_3PbI_3$ which shows a band alignment favorable for electron extraction via the GaAs.

In addition, the electron mobility of GaAs is $8500\left(\frac{cm^2}{V*s}\right)$ at 300K and the hole mobility is $400\left(\frac{cm^2}{V*s}\right)$ at 300K *[29].* In figure 3.6, we can see a diagram of electron and hole mobility as well as diffusivity D as a function of doping carrier concentration at 300K for GaAs. Diffusivity describes the ability of carriers to diffuse in the semiconducting material due to the existence of a carrier concentration difference.

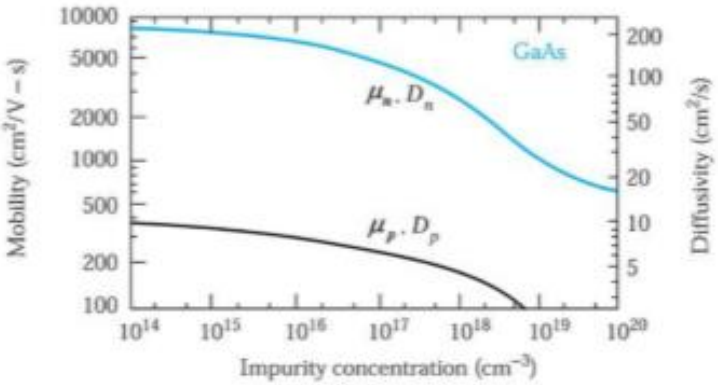

Figure 3.6: Mobility for electrons (μ_n) and holes (μ_p) and carrier diffusivity vs impurity concentration at room temperature *[37].*

We observe that GaAs has a sensitively much higher electron mobility compared to TiO_2, by a factor between 10^4 and 10^5. This means that GaAs can efficiently extract electrons as an ETL. As we can see from the above figure, mobility of electrons and holes is maximum at low doping concentrations, due to reduced carrier scattering with impurity atoms *[31],[37].*

3.3 Advantages of GaAs Nanowires compared to TiO_2

GaAs is an appropriate semiconducting material that can be used as an electron transporting material (ETL) in perovskite solar cells, instead of TiO_2 for a number of reasons. One reason is the orders of magnitude higher values in carrier mobility compared to TiO_2. Particularly, GaAs exhibits an electron mobility value that is up to five orders of magnitude higher than the corresponding value for TiO_2 at 300K. One reason for this difference lies in the crystalline quality of the two semiconducting materials. Specifically, TiO_2 is polycrystalline, while GaAs is single crystalline. The grain boundaries in polycrystalline materials like TiO_2 influence the charge transport and carrier mobility values of the material. Particularly, the grain boundaries are the interfaces dividing the crystallite grains. They include defects or dislocations, creating a compositional inhomogeneity in that region *[35]*. These defect sites can act as charge traps for carriers, forming space charge regions in the grain boundary. Therefore, a potential barrier is created that can hinter charge transport, under the application of an electric field *[36]*.

Moreover, the lower mobility values of TiO_2 can be explained, taking into account its bandgap energy. Owing to the fact that TiO_2 has a much higher bandgap energy compared to GaAs, the effective mass of carriers is bigger. As a result, the mobility values of TiO_2 will be lower, as can be extracted by equation 3.4. Generally, the difference in the mobility values between the two materials translates to a discrepancy in the electron motion between GaAs and TiO_2 electron transporting materials. Therefore, electron mobility is a property of paramount importance that should be taken into account for the choice of the ETL.

In addition, as can be inferred by the energy diagram for GaAs, favorable band alignment of the (LUMO) energy levels between the GaAs and the perovskite material is achieved. Therefore, effective carrier separation can occur, which is a prerequisite property for the choice of the electron transporting material.

Finally, as we know, GaAs is a semiconducting material with a high fabrication cost. For this reason, GaAs nanowire structures can be used as an ETL in perovskite solar cells instead of bulk GaAs, reducing significantly the cost of fabrication.

CHAPTER 4

Basics of Impedance spectroscopy

For impedance measurements, alternating (AC) voltage signal $V_{ac}(t)$ is applied and alternating current response I_{ac} is measured.

V_{ac} and I_{ac} are frequency-dependent functions expressed as:

$$V(t) = V_o * \sin(\omega * t) = V_o * e^{i*\omega*t} \quad (4.1)$$

$$I(t) = I_o * \sin(\omega * t + \varphi) = I_o * e^{i(\omega*t+\varphi)} \quad (4.2)$$

V_o, I_o value is the amplitude of voltage and current signal respectively, ω is the angular frequency, ϕ is the time delay between V(t) and I(t). So, impedance can be defined as:

$$Z(t) = \frac{V(t)}{I(t)} = Z_o * e^{-i*\varphi} \quad (4.4),$$

where $Z_o = \frac{V_o}{I_o}$ (4.5)

Impedance Z function describes the complex resistance of the sample as a function of frequency, considering a representative equivalent circuit. Particularly, the impedance Z describes the resistance from the contribution of all the elements of the equivalent circuit. By varying the values of frequency, impedance values change as well in the frequency domain. Impedance can be represented as a conjugate:

$Z = Z' - i * Z''$, where Z'=Z(ϕ=0) and corresponds to the resistance of the sample (according to Ohm's law), while Z''=Z(ϕ=90^0) corresponds to the reactance X. Z'' describes the resistance of the sample to changes in current flow.

$$Z = R + j * X \quad (4.6)$$

In the case that the equivalent circuit includes a capacitor element apart from resistors, X is defined as: $X = \frac{1}{\omega*C}$ (4.7). In figure 4.1, there is a time-domain representation of V(t) and I(t) and a representation of impedance Z *[40].*

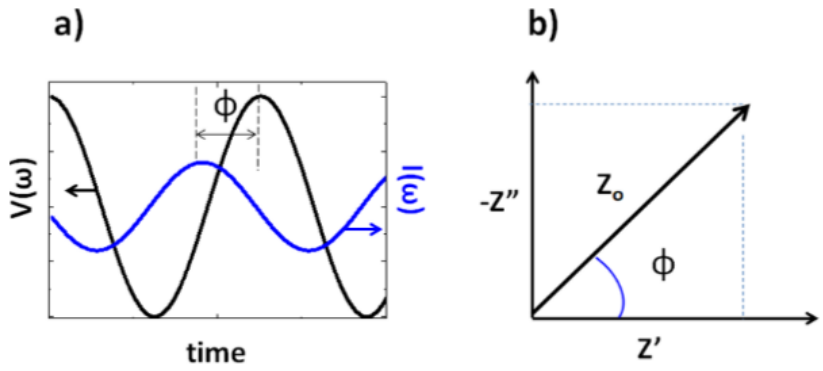

Figure 4.1:(a) Time-domain representation of V(t) and I(t). The angle ϕ expresses the time delay between the voltage input and the current response (b) Representation of impedance Z *[40].*

Admittance (Y) is defined as $Y = \frac{1}{Z}$ (4.8).

It is the reverse of impedance and it expresses the conduction of carriers. It has a real and an imaginary part.

So, $Y = Y_r + Y_{im} = G + jB$ (4.9),

where G, B represent the real and the imaginary part of the admittance respectively. Specifically, G is the conductance and B is the Susceptance.

Moreover, the magnitude of Admittance is $|Y| = \sqrt{G^2 + B^2} = \frac{1}{|Z|} < \vartheta$ (4.10),

where $\theta = \arctan\left(\frac{|B|}{G}\right) = -\varphi$ is the phase of the admittance. Admittance vector is represented in figure 4.2.

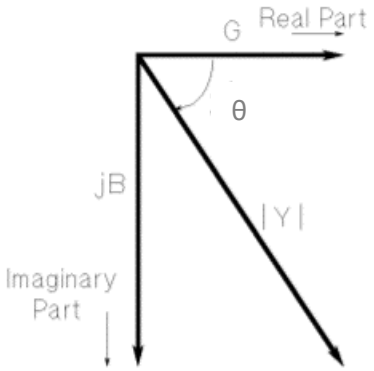

Figure 4.2: Vector representation of admittance (Y)

Another parameter can be defined, the dissipation factor D which is defined as the ratio of the real to the imaginary part of admittance *[41]*:

$D = \frac{Y_r}{Y_{im}}$ (4.11)

The measurements of impedance, admittance and dielectric spectroscopy are called immitance measurements.

In impedance measurements, voltage application in a passive metal-semiconductor material results in a depletion of mobile charges. A static capacitor is created due to the voltage stimuli. So, a depletion region from carriers is built in with characteristic capacitance. When the applied voltage changes, the width of the depletion region shifts as well, resulting in a different capacitance, which is considered frequency independent over a well defined frequency range in C-f spectrum. Therefore, impedance measurements can give us information of the doping concentration at each depletion width. Moreover, in dielectric spectroscopy immitance measurements can be used to gain insight on the material properties. That's because the perturbation caused by the voltage signal induces relaxation processes, such as lattice distortions, electrode polarization, and possibly dipole rearrangement and electrical-ionic conduction *[40].*

One model that can be used for impedance measurements in semiconductors is Agilent model. It is considered that a diode is represented with an equivalent circuit that incorporates

only resistor and capacitor elements. Agilent model describes two kinds of equivalent circuits, either the parallel circuit or the series circuit. The selection between the two circuits representative for the diode is based on some assumptions that should be taken into account. Particularly, if the capacitance of the circuit is small, meaning high impedance values, parallel resistance R_p (to the capacitor element) is more significant than the series resistance R_s. Therefore, the equivalent circuit is simplified to a parallel circuit. On the contrary, if the capacitance of the circuit is large (low impedance value), series resistance (R_s) is more significant than the parallel resistance (R_p). In figure 4.3, we can see a description of the assumptions considered to select an equivalent circuit model (either parallel or series circuit).

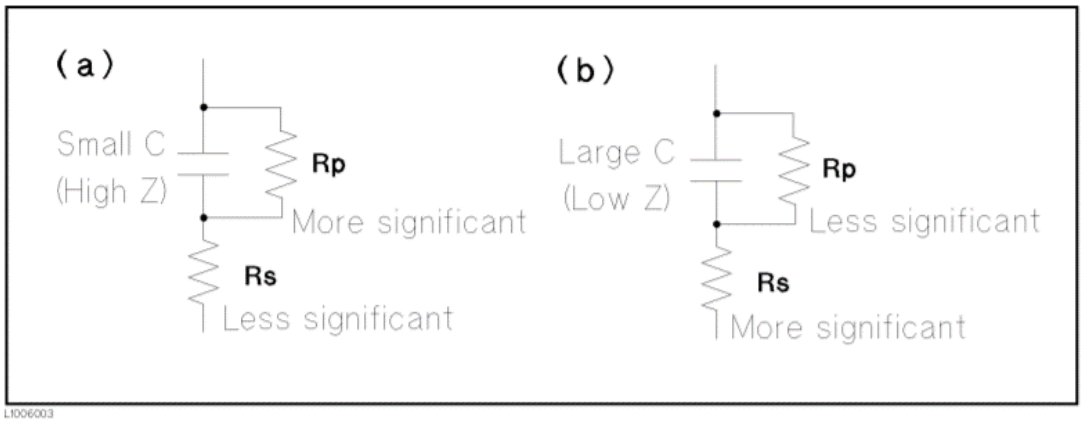

Figure 4.3: The criterion considered for the selection of the equivalent circuit. The equivalent circuit model is simplified to the parallel and the series circuit based on the assumptions considered in case (a) and (b) respectively.

For the parallel model: $Y = \frac{1}{R_p} - j\omega C_p$ (4.12).

So, $Y_r = G = \frac{1}{R_p} \rightarrow R_p = \frac{1}{Y_r}$ (4.13)

and $Y_{im} = B = -\omega * C_p = -2\pi f C_p \rightarrow C_p = -\frac{Y_{im}}{2*\pi*f}$ (4.14)

For the series model: $Z = R_s - \frac{1}{j*\omega*C_s}$ (4.15)

So, $R = R_s$ and $X = -\frac{1}{\omega*C_s}$.

Because $Z = \frac{1}{Y} = \frac{(G-jB)}{(G^2+B^2)}$ (4.16), it is extracted that $R_s = \frac{G}{(G^2+B^2)} = \frac{Y_r}{({Y_r}^2+{Y_{im}}^2)}$

and $C_s = \frac{G^2+B^2}{2*\pi*f*B} = \frac{{Y_r}^2+{Y_{im}}^2}{2*\pi*f*Y_{im}}$

So, the parameters of the circuit C_P, C_S,R_p, R_s can be determined for each voltage value at a particular signal frequency.

Dissipation factor (D) value determines the circuit model which is representative for the diode. Specifically, if D<<1 ($Y_r \ll Y_{im}$) or otherwise the reactance X is higher than R_p, parallel circuit model dominates. In the vice-verse case $Y_r \gg Y_{im}$, the series circuit model is predominant. When Y_r and Y_{im} values are comparable with each other, it is suggested that the equivalent

circuit is more complex, involving both shunt and series resistance, as can be seen in figure 4.3 *[41].*

CHAPTER 5

Experimental part

Nanowire templates

The nanowire samples that were studied were grown with Molecular Beam Epitaxy (MBE) technique, using Vapor-Liquid-Solid (VLS) growth in an MBE chamber under high vacuum conditions. A vapor of Ga and As atoms is diffused in the liquid Ga droplet. Then, nucleation of GaAs takes place in the interface between the solid substrate and the liquid droplet. So, GaAs crystal starts to grow and GaAs core nanowire structure is formed. The liquid Ga droplet is led to the top of the nanowires and it is removed under appropriate conditions. For instance, Ga droplet is removed by introducing As in the chamber. So, Ga droplet crystallizes in GaAs and As destroys Ga droplet, while determining a trigonal shape of nanowire tip.

Nanowire samples that were used for the fabrication of hybrid nanowire/perovskite structures are samples 445, 448, 586, D0449.

Initially, sample 445 has the following structure:

It consists of GaAs nanowires with a bare core structure grown on a n^+ silicon substrate. Nanowire sample 445 has two regions, region L and region R. Region L is a region with dense nanowires (high nanowire density) and region R is a region with sparse nanowires (low nanowire density). The geometrical characteristics of nanowires are the following: For sample 445L, nanowire mean diameter is <d>=33nm and mean height is <h>=1.2μm. The average nanowire density in this sample is 3.4 $*10^9$ NWs/cm^2. For sample 445R, nanowire mean diameter is <d>=58.5 nm and mean height is <h>=1.3μm. The average nanowire density in this sample is 6.4 $*10^7$ NWs/cm^2. In figure 5.1 we can see schematically the nanowire structure for sample 445.

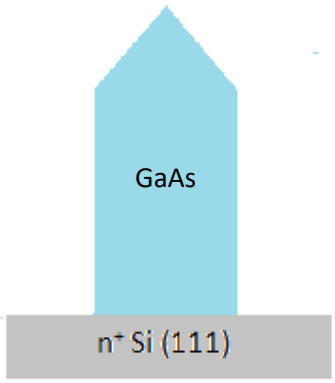

Figure 5.1: Structure of nanowires for sample 445.

In figure 5.2 we can see SEM images of sample 445L,R:

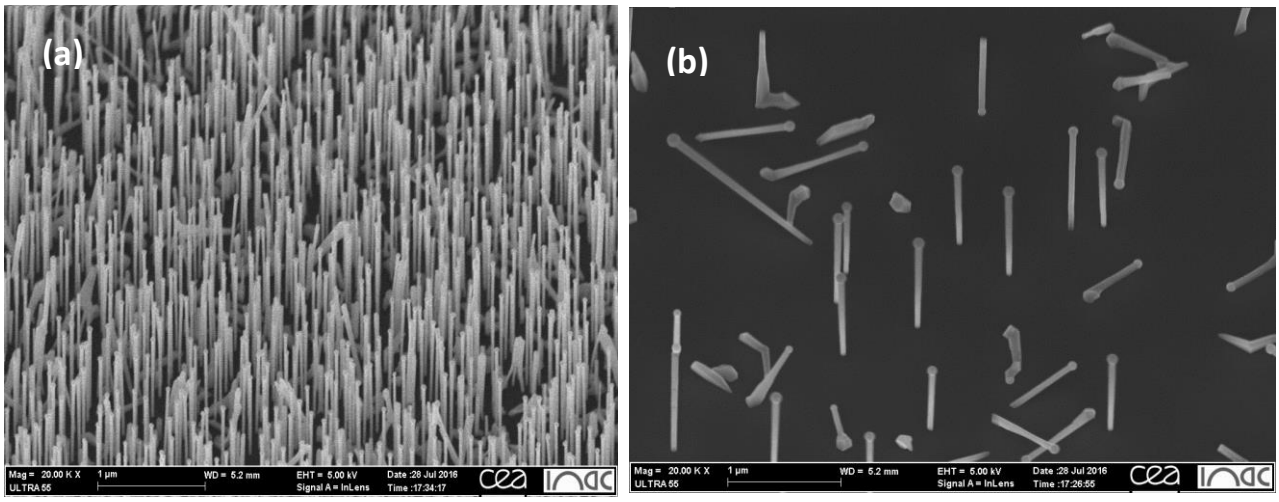

Figure 5.2: SEM images of nanowire sample 445 under a tilt of 30^0. Regions L and R are illustrated respectively.

As for sample 448, it has nominally the same nanowire structure as sample 445:

The geometrical characteristics of nanowires are the following: For sample 448L, nanowire mean diameter is <d>=46nm and mean height is <h>=1.2µm. The average nanowire density in this sample is $8*10^8$ NWs/cm^2. For sample 445R, nanowire mean diameter is <d>=55 nm and mean height is <h>=1µm. The average nanowire density in this sample is $4.1 *10^7$ NWs/cm^2.

In figure 5.3, SEM images are illustrated for sample 448L,R:

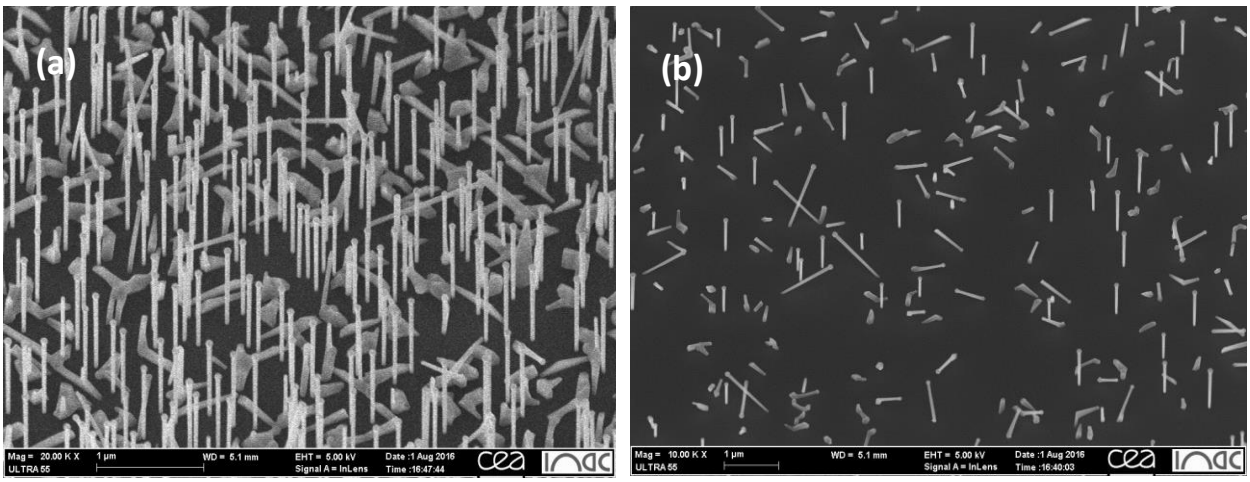

Figure 5.3 : SEM images of nanowire sample 448 under a substrate tilt of 30^0. Regions L and R are illustrated respectively.

As for sample 586, it has the following structure:

It consists of a core-shell nanowire structure on a n^+ silicon substrate. The core consists of p-type GaAs of 45nm thickness. A thin capping layer of p^+ AlAs is then deposited of thickness 0.1nm. Subsequently, the shell is deposited which consists of p^+-doped InGaAs of 35nm

thickness. Moreover, there is a thin layer around the shell which consists of p^+-doped AlGaAs that is 0.5nm thick and a subsequent layer of p^+-doped GaAs of 3nm thickness. Nanowire mean diameter is <d>=122.3nm and mean height is <h>=2.88μm. The average nanowire density in this sample is $2.8*10^8$ NWs/cm^2.In figure 5.4 we can see schematically the nanowire structure of this sample.

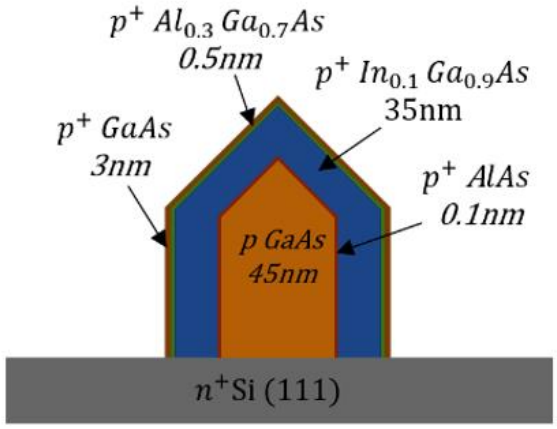

Figure 5.4: Structure of sample 586.

In figure 5.5, we can see a cross- section SEM image of sample 586:

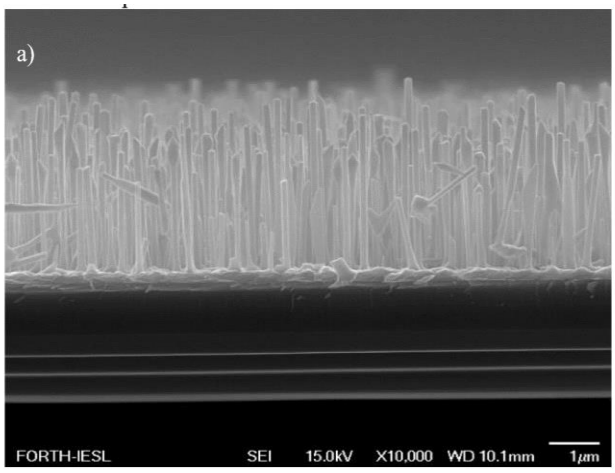

Figure 5.5: Cross-section image of sample 586. Nanowire mean diameter is <d>=122.3nm, mean height is <h>=2.88μm and parasitic length is <P.L.>=279.5nm. Average nanowire density is $2.8*10^8$ NWs/cm^2.

As for sample D0449, it has the following structure:

It consists of GaAs nanowires with an axial structure made of GaAs and AlGaAs on a n^+-doped silicon substrate. Nanowires are not doped, they are intrinsic. The axial structure consists of two 10nm-thick GaAs QWs separated by 20nm-thick AlGaAs barriers. Moreover, the nanowire mean height is <h>~1.2μm and their mean diameter is <d>~30nm. The average nanowire

density in this sample is $3*10^8$ *NWs/*cm^2. In figure 5.6, we can see schematically the nanowire structure of this sample.

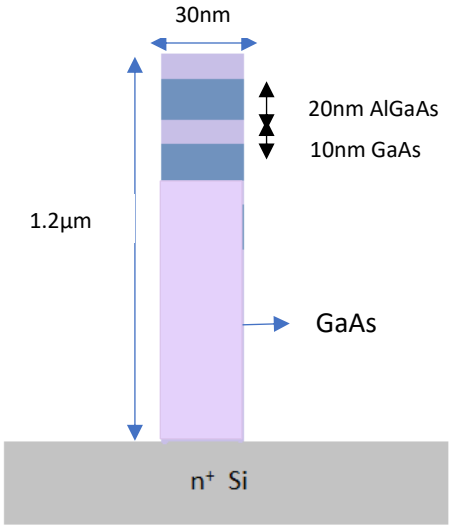

Figure 5.6 : Nanowire structure and dimensions of sample D0449

In figure 5.7, we can see a cross- section SEM image of sample D0449.

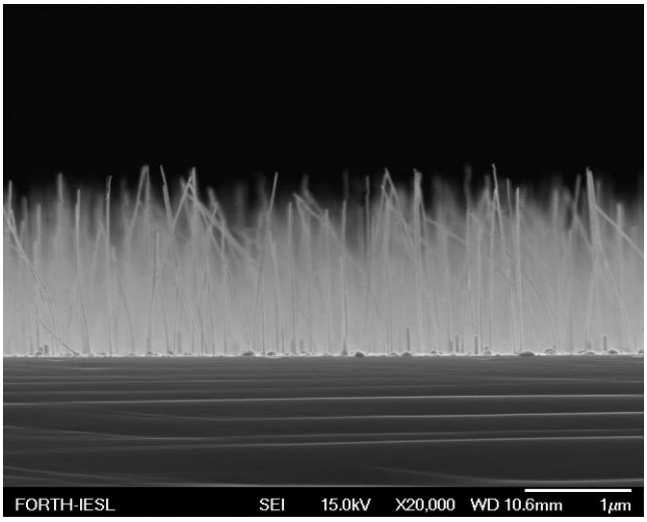

Figure 5.7: A cross-section SEM image for sample D0449, where we can see nanowires before processing. Nanowire length is *h=1.2-1.4µm, nanowire* diameter is *d=30-40nm.* The average nanowire density is *3*10^8 NWs/cm^2.*

A typical hybrid nanowire/perovskite structure incorporates a nanowire template, which consists of an n-type substrate on which nanowire structures are grown. In our case, the substrate is made of n^+-doped Silicon. Nanowires are covered by a dielectric polymer, BCB which acts as an insulating layer by preventing the direct contact of the upper perovskite layer with the silicon substrate. So, short-circuiting effect is averted. After BCB deposition, etching

of BCB in oxygen plasma follows, until the tips of the nanowires to emerge from the BCB layer. Then, the perovskite layer is formed covering the nanowires. After that, a p-type hole transporting material (HTL) is deposited, which is CuSCN in our case. As a result, an n-i-p junction is formed. Subsequently, a thin layer of Au is deposited, for contacting purposes.

Below, in figure 5.8, we can see a schematic illustration of a typical hybrid nanowire-perovskite solar cell device.

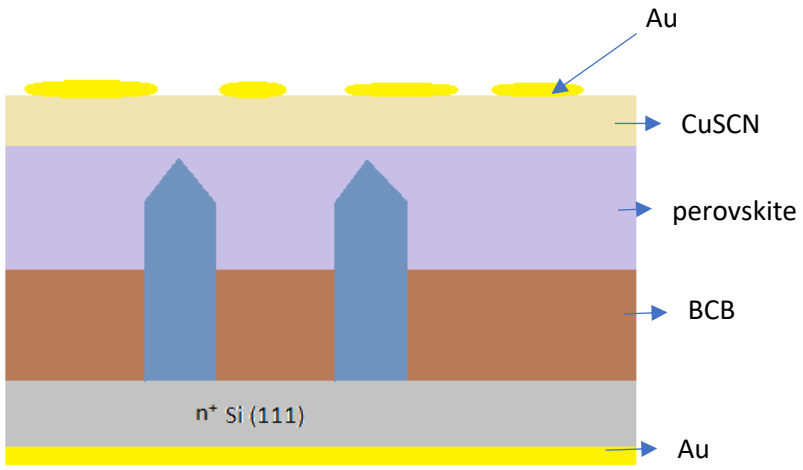

Figure 5.8 : Schematic illustration of a typical hybrid nanowire/perovskite solar cell device

It should be noted, that in this configuration the Au metal layer should be semitransparent, so that incident light can reach the perovskite absorbing layer. This is bothersome and in order to bypass this issue, p-type metal oxide transparent in most of the visible spectrum needs to be developed. Alternative designs to be tested would be inverted p-i-n structure, where:

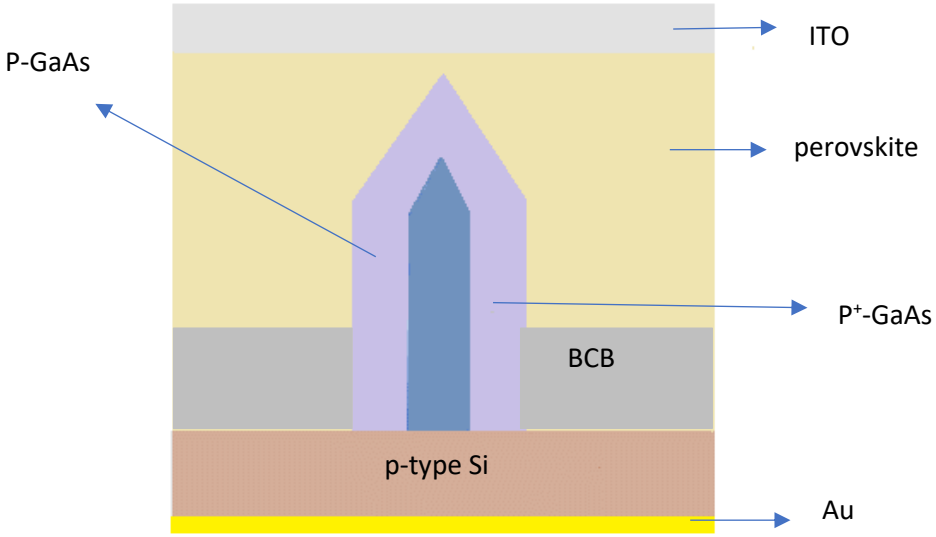

Figure 5.9: Inverted p-i-n nanowire/perovskite solar cell structure

Samples synthesis

Solution composition

For the preparation of perovskite via hot-casting technique, we used PbI_2 and CH_3NH_3Cl as reactants in 1:1 mole ratio. Specifically, we added 290mgr of PbI_2 in 3ml DMF, so as to fabricate a solution of C=0.22M and then added 43mgr of CH_3NH_3Cl. After the fabrication of the precursor solution, infiltration of the solution follows. Infiltration means that the solution is isolated from dust particles that have not dissolved. So, perovskite is going to be formed, which incorporates both $CH_3NH_3PbCl_3$ and $CH_3NH_3PbI_3$ perovskite compounds.

The preparation of the perovskite precursor solution which is used for the formation of $CH_3NH_3PbI_3$ perovskite via 2-step method is the following: Initially, PbI_2 solution is prepared in DMF solvent in concentration of C=1M or C=1.5M. Subsequently, CH_3NH_3I (MAI) solution in pentanol is composed in a proportion: 10mgr/ml. MAI solution is the dipping solution. So, about 15 ml of solution were fabricated. After the solutions synthesis, PbI_2 was deposited on nanowire substrates via spinning, in spinning conditions:300rpm, 300rpm/s for 10sec. After spinning,we wait for a minute and then the nanowire film is spinned again at 3000rpm, 300rpm/s for 40sec.These mild conditions were adjusted to achieve effective coverage of perovskite around the nanowires, avoiding nanowire breaking that could occur at high rpms or high speed rates. For FTO substrates the spinning conditions of PbI_2 are: 6000rpm,1000rpm/s for 60s. After spinning, the films are dried in 75^0C for 15min in air and after cooling they are dipped in MAI solution. So, perovskite starts to be formed.The time in the dipping solution is determinant for the perovskite structure and perovskite thickness. Finally, the samples are dried in a hot plate at 75^0C for 15min *[42].*

We used CuSCN as a hole transporting material (HTL). For the preparation of CuSCN solution, 25mgr/ml of CuSCN are used in diethylsulfide solvent. Stirring of the solution follows at 50^0C for 1h. Then, the solution is left to cool down at room temperature. After that, the CuSCN solution is filtered by using a 0.45 μm pore size filter, before solution spinning on thin films. CuSCN solution includes diethylsulfide, a solvent which is photosensitive and exposure to illumination can cause photocatalytic reactions leading to solution degradation. For this reason, CuSCN solution should not be exposed to light much, and should be stored in a shaded place.The spinning conditions for CuSCN solution are: 2000rpm, 1000rpm/s for t=30sec *[43].*

After the synthesis of our samples, measurements of optical characterization are taken to examine the optical characteristics of the samples and estimate their photovoltaic response. Specifically, dark and photo current-voltage (I-V) measurements and capacitance-voltage (C-V) measurements were taken. Moreover photoluminescence (PL) measurements were carried out to examine the optical emission of samples that we fabricated.

Samples characterization

Experimental set-up for dark and photo I-V measurements

For dark and photo I-V measurements of nanowire samples the experimental set-up is the following:We used a xenon (Xe) lamp of 150W of Hamamatsu company, which is ozon free. We also used a Keithley 6517A multimeter as a voltage source that also operates as a current meter.

The measurement for light intensity (power) is implemented with the power meter instrument of Newport company, which is spectrally calibrated (1830C model).

The power density of the sample was adjusted to ~100 mW/cm^2 with a spot diameter of 3mm.

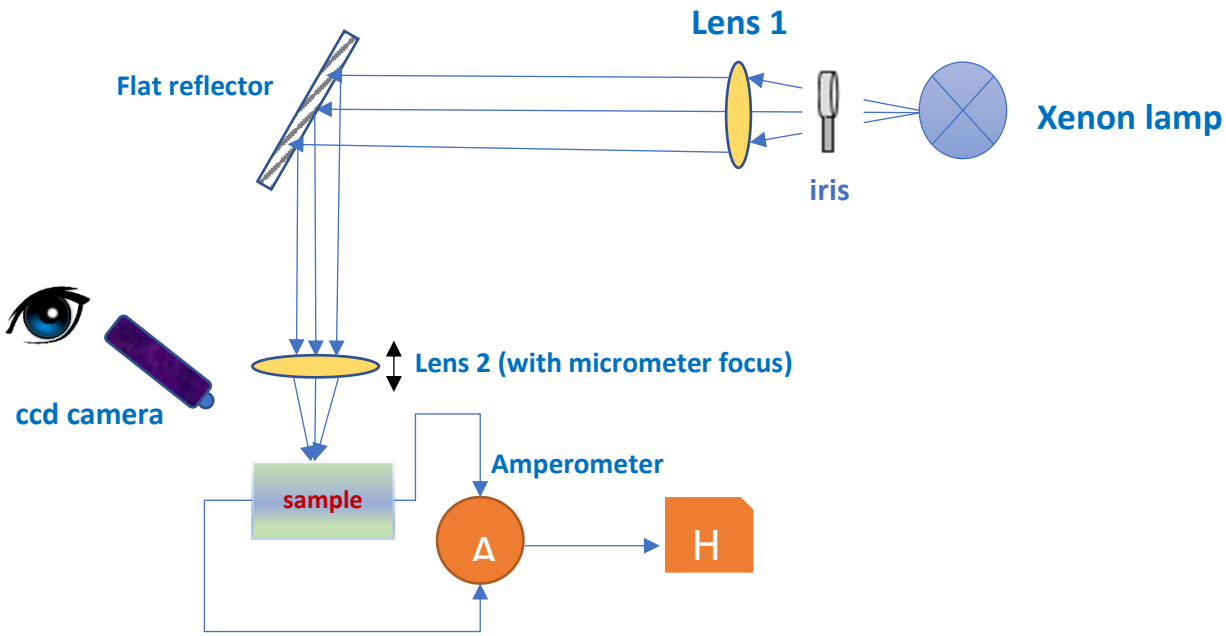

Figure 5.10: Experimental set-up for dark and photo I-V measurements of nanowire samples.

The description of the experimental set-up shown in figure 5.10 is the following: In front of the xenon lamp an iris is placed, so as to control the beam intensity that exits from the lamp. Subsequently, the light beam falls into a converging lens of focal length f=15cm and comes out in parallel. Then, the collimated beam falls onto a flat reflector, whose role is to direct the parallel beam down to our sample. A second converging lens is then placed that has a focal distance f=5cm, which focuses the parallel beam on our sample, as we can see in the figure. The beam spot at the sample had a diameter of 3mm. Finally, our sample is connected with a voltage and amperometer source, as we can see in figure 5.11. So, we take current-voltage measurements, which we use for the analysis of our experimental data.

In figure 5.11, we can see the circuit connection for the nanowire device structure depicted in figure 5.8. The circuit closes via the gold metallic contacts which are placed above and below the sample.

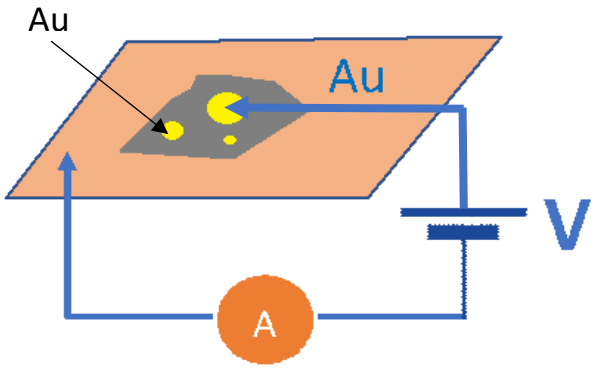

Figure 5.11: Connection of the nanowire sample in a voltage source.

PL measurements

Photoluminescence (PL) measurements were carried out at room temperature (T=295K). The laser beam had a wavelength λ_χ=325nm. Moreover, a ND1 filter was used that reduces the power of the initial beam, so as $P = \frac{P_O}{10}$ .Micro-PL measurements were carried out at room temperature (T=295K). Laser beam had a wavelength λ_χ=532nm. The initial power was P_o=4μW. A filter was used to reduce the power of the initial beam.

Analysis of the experimental part

First experimental efforts that have been made on nanowire templates were based on the hot-casting technique. Nanowire sample 448R/L was used for the first tests, before BCB deposition. L,R symbols mean that the nanowire sample has two regions, a region with nanowires of high density (L) $\sim 10^9 cm^{-2}$ and a region with sparse nanowires (nanowire density$< 10^8 cm^{-2}$), R region. In sample 448L/R a parasitic GaAs-based layer has been formed on the Si surface in-between nanowires, during nanowire growth. For this reason, we coated nanowires with compact TiO_2 as an insulating layer, in order to eliminate current leakage through the parasitic layer. So, nanowire substrates from 448L and 448R samples were coated with TiO_2 by spinning in conditions of 2000rpm, 4000rpm, 6000rpm and at 1500rpm/s for 20s. In figure 5.12, we can see SEM images from sample 448R/L after coating with TiO_2 and after annealing the film at 400^0C for 15min.

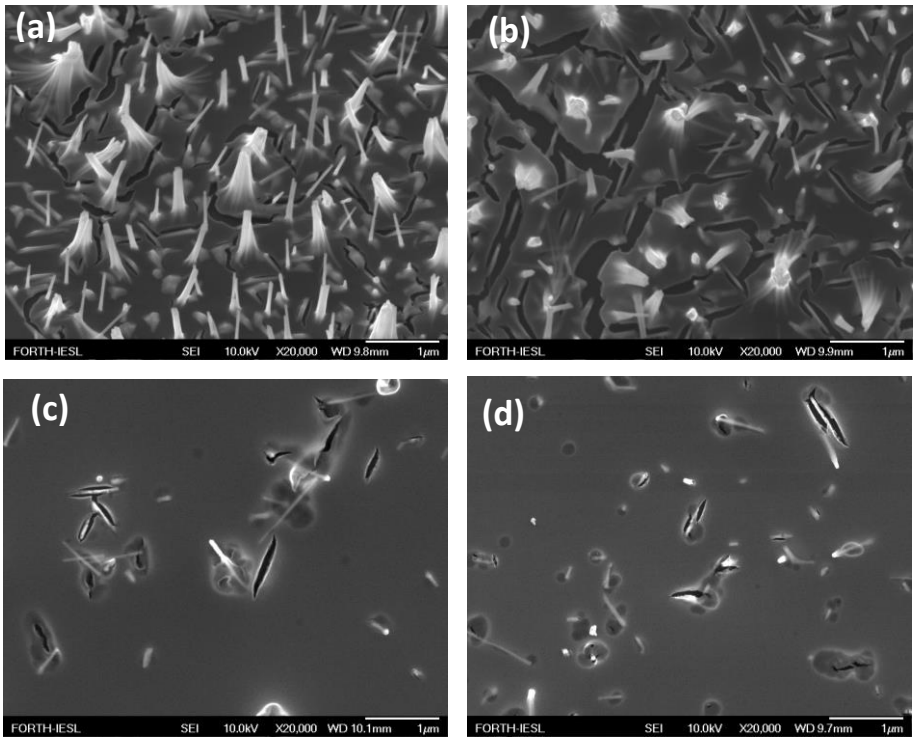

Figure 5.12: (a),(c) SEM images after coating the nanowire samples 448L and 448R with TiO_2 (at 2000rpm spinning conditions).(b),(d) SEM images after annealing them in furnace at 400^0C for 15min.

As we can see from SEM images of figure 5.12, after TiO_2 deposition, cracks were created on the film surface. These cracks got larger after annealing the films in a furnace at 400^0C. Moreover, we can see that nanowires have fallen, possibly due to the high-speed spinning conditions. In addition, HCl which is a constituent of the solution for the deposition of compact TiO_2, may have influenced the GaAs nanowires. Specifically, the Ga ball that was formed on the tips of nanowires was destroyed by HCl acid. Additionally, we further noticed that neighbor nanowires got stuck with each other, most likely due to some reaction during TiO_2 deposition. The chemical modification of the nanowires is further supported by an unexpected PL emission at 600nm. For this reason, we concluded that a kind of chemical reaction occurred on the GaAs nanowires, during TiO_2 spinning, and henceforth we looked into alternatives for insulating the nanowire arrays, such as using BCB.

BCB is Benzocyclobutene, a polycyclic aromatic hydrocarbon. A BCB-based polymer Cyclotene 3022-46 BCB was used for insulating the nanowires. The deposition of this polymer on the nanowire template is made by spinning at the following spinning conditions: 1st step: 300rpm revolution and 300 rpm/s acceleration, t=10sec and 2nd step: 3000rpm revolution and 300 rpm/s acceleration, t=40sec. Subsequently, BCB is baked at 110^0C for 1 min. After that, BCB undergoes to thermal annealing. The steps of the thermal treatment are the following: 1) A gradual temperature increase (ramp) to 20^0C in 2 sec and a stay in this temperature for 2 sec. 2) A ramp to 100^0C in 15min and a stay in this temperature for 15min. 3) A ramp to 150^0C in 15min and a stay in this temperature for 15min. 4) A ramp to 250^0C in 1h and a stay in this temperature for 1h. 5) A gradual temperature decrease (ramp) to 20^0C in 30min and a stay in this temperature for 2 sec. Subsequently, BCB etching with oxygen plasma follows until nanowires to emerge from

the BCB layer. The conditions of this process are the following: Power is 200W, Pressure is 140mTorr, and the process time is 11min. Below, SEM images are shown before and after BCB deposition for the nanowire sample 448L.

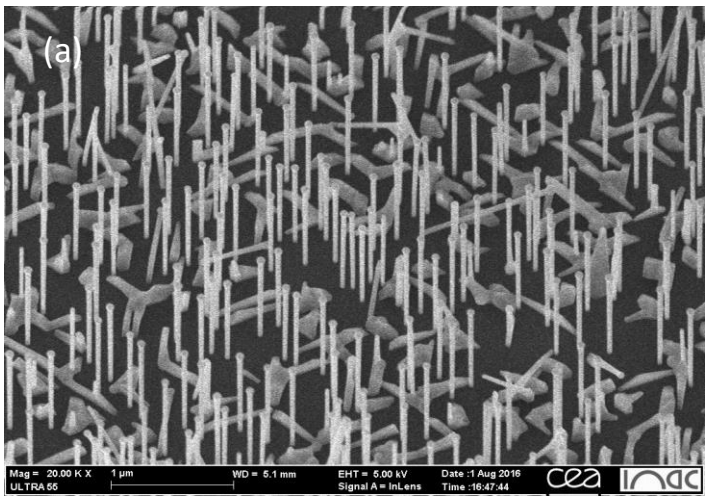

Figure 5.13: SEM image for sample 448L before the deposition of BCB.

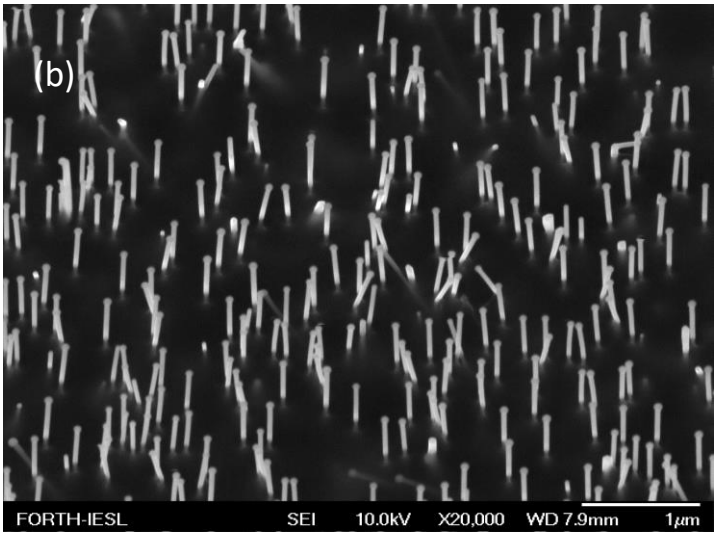

Figure 5.14: SEM image for sample 448L after the deposition of BCB.

The next step was to learn to deposit perovskite using the hot-casting technique either on silicon substrate or on GaAs nanowires /Si substrate, both covered with BCB. In both cases, the surface of the BCB did not favor perovskite formation on the film. For this reason, we tested different surface treatments, so as to "functionalize" the BCB surfaces and enhance effective perovskite formation on them. Specifically, these treatments are oxygen plasma treatment and treatments with ozone cleaner or a chemical solution called HMDS. Samples PV36-38 were fabricated which have the following structure: Si/BCB/perovskite. Before perovskite deposition, Si/BCB substrate was processed with oxygen plasma, ozone or HMDS treatment, respectively. In this run, both the precursor solution and the substrate were heated at 135^0C. Comparing the perovskite structure of these samples for the different BCB treatments, Asher oxygen plasma treatment seems to favor perovskite formation as can be seen in figure 5.15.

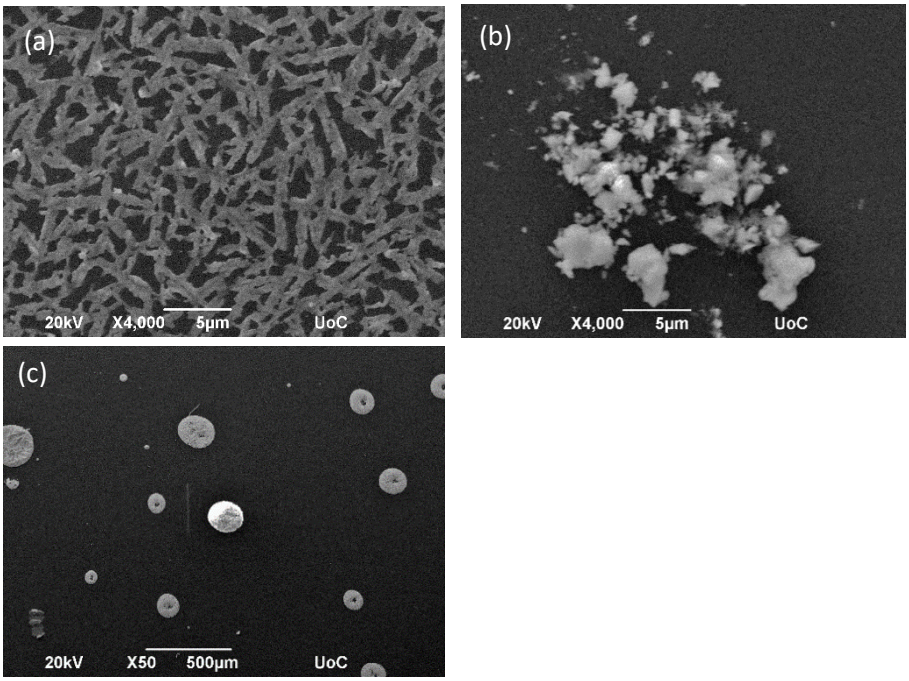

Figure 5.15: SEM images for samples PV 36-38, having the Si/BCB/perovskite structure. Prior to perovskite formation the BCB surface has been submitted to (a) Asher, (b) ozone and (c) HMDS treatment, respectively. In this run, the perovskite deposition occurred via the hot-casting technique, where both solution and substrate were heated at 135^0C.

The temperature conditions of solution and substrate may also influence the perovskite growth. For this reason, new samples were fabricated in order to examine the perovskite structure on Si/BCB substrates using different solution and substrate temperatures and various surface treatments (Figure 5.16).

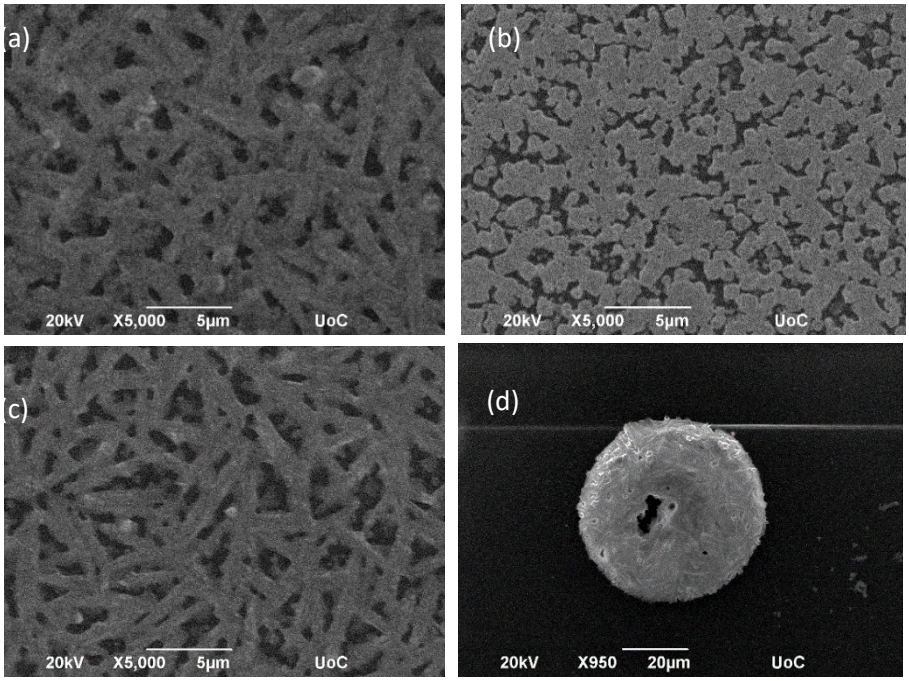

Figure 5.16: Perovskite formation on Si/BCB substrates using (a,b) Asher surface treatment, (c) Ozone treatment, (d) HMDS treatment and using a solution temperature of 70^0C and a substrate temperature of 135^0C.

We observe that better perovskite structure has been achieved, at a solution temperature of 70^0C and a substrate temperature of 135^0C, using an oxygen plasma (Asher) surface treatment. As shown in figure 5.16b, perovskite layer forms with a relatively good film coverage, despite some voids. We should mention that two samples were fabricated under the same temperature conditions and oxygen plasma treatment, in order to test the reproducibility of the process, which exhibited slightly different perovskite structure (Figure 5.16a,b).

Based on the above results, we tested the formation of perovskite using the hot-casting technique on nanowire templates of sample 448L with BCB coverage. Pre-treatment of the BCB surface with oxygen plasma had preceded. The precursor solution was heated at 70^0C before solution deposition. So, nanowire samples PV93 and PV94 were fabricated using different spinning conditions. PV93, 94 were spinned at 6000rpm, 1000rpm/s for 30s and at 2500 rpm,1000rpm/s for 30s, respectively. In figure 5.17 we can see SEM images of the samples PV93,94.

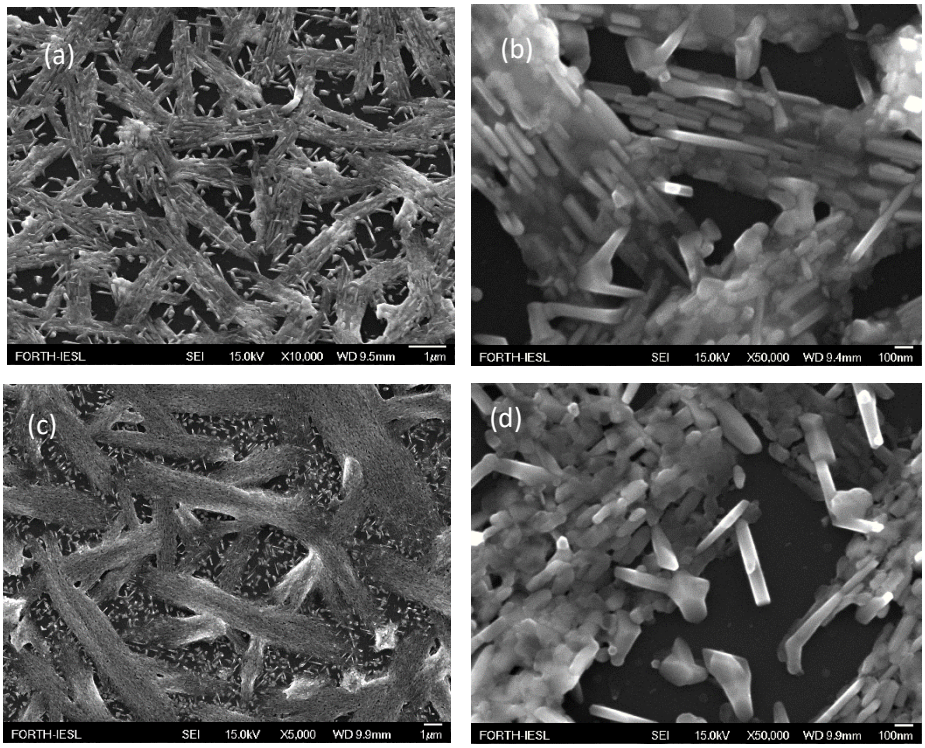

Figure 5.17: SEM images at different magnifications of nanowire samples PV93 (a,b) and PV 94 (c,d) at a tilt of 30^0. These samples were spinned at 6000rpm and 2500 rpm respectively.

As we can see from the SEM images, the perovskite structure is grown somewhat randomly and does not enclose all nanowires. Moreover, many nanowires appear fallen possibly due to high speed spinning conditions. In addition, the perovskite structure seems poorly formed, requiring further optimization.

However due to the fact that in the hot-casting technique, spinning takes place under high speed and high acceleration rate conditions, which tend to damage the nanowire array as observed in the SEM images of figure 5.17, we decided to test an alternative fabrication technique, avoiding such harsh spinning conditions.

For this reason, we tested a new experimental technique for perovskite growth, the so-called two-step method. The two-step method is compatible with our experiments on nanowire substrates, considering that it can achieve effective perovskite growth around the nanowires, without the problems caused by the hot-casting technique. By using this technique, mild spinning conditions were adjusted for the deposition of PbI_2 on nanowire templates. Particularly, the spinning conditions of PbI_2 are: 300rpm/s, 300 rpm, for 10sec. 1min waiting and 3000rpm, 300rpm/s, for 40sec. These spinning conditions are the same with the ones used for BCB deposition on nanowire templates. Therefore, we suggest that the nanowires won't be harmed, which can be confirmed by SEM images mentioned later on.

Initially, we applied the two-step method on Si/BCB substrates. The samples were immersed in MAI solution for various dipping times. From the SEM image in Fig. 5.18a for a 40min dipping time, we can see that the perovskite structure is inhomogeneous. PL spectra showed different PL peaks, also suggesting inhomogeneity in the structure, possibly due to other intermediate

phases created during perovskite formation. Moreover, the PL spectra vary between different points of the sample, showing that the sample is also inhomogeneous at large scale.

White spots that formed on the sample surface indicated that iodine salt residues have been left in our film during dipping in MAI solution. In order to remove the solvent and the salt residues from the sample, we tried to blow the sample with a dry air pistol, after dipping in MAI solution. Accordingly, a new set of samples were fabricated with the same fabrication conditions but using the blow-drying technique. From SEM images, we infer that white spots have been limited. In figure 5.18, we show characteristic SEM images from each set of samples for a 40 min dipping time (samples PV159 and PV178), as well as the corresponding PL spectra. Comparing the perovskite structure in the two samples, we notice that the perovskite structure is more homogeneous in the second set of samples (PV178) (Figure 5.18(b)). Moreover, the PL spectrum taken on this sample, showed a single emission peak around λ=760nm and at different points of the sample Figure 5.18(d). The existence of a unique PL peak indicates that there is no formation of other intermediate phases in the perovskite structure. Therefore, we infer that remnant iodine salts (white spots) on the perovskite film affect the perovskite structure, favoring the formation of intermediate phases.

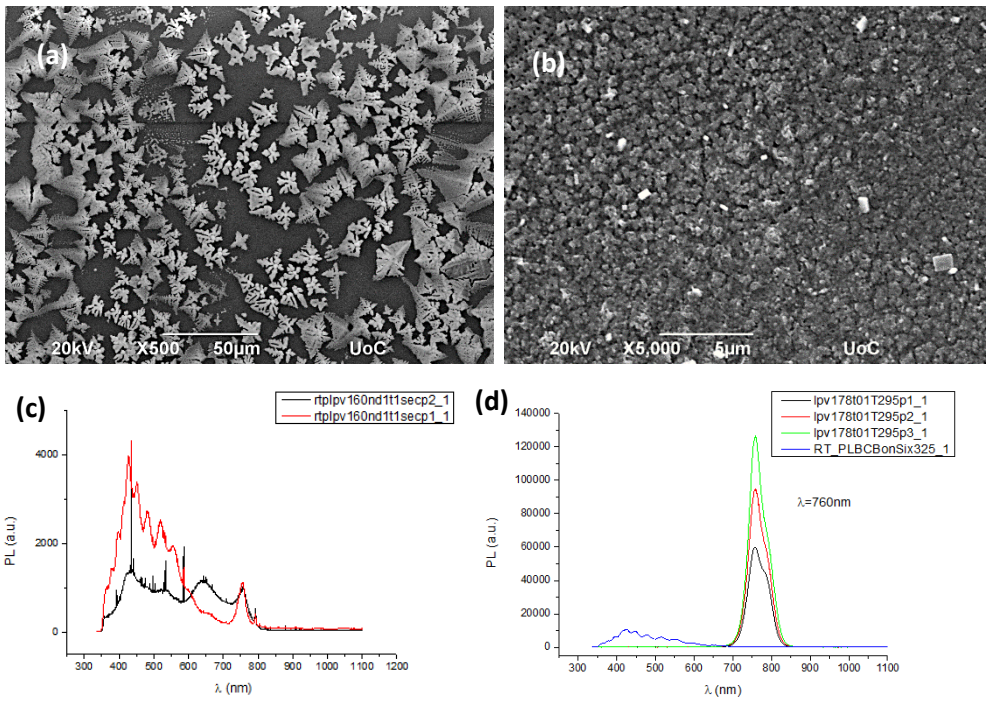

Figure 5.18: (a) SEM image of sample PV159 in dipping time of 40min.(b) New sample, PV178 has been fabricated using a blow-drying technique after a dipping time of 40min. (c,d) Respective PL spectra of these samples.

In addition, micro PL measurements were performed on sample PV178, in order to examine the PL emission in different regions of the sample, investigating possible differences in the structure. In figure 5.19, micro-PL spectra are illustrated for two different regions of the sample.

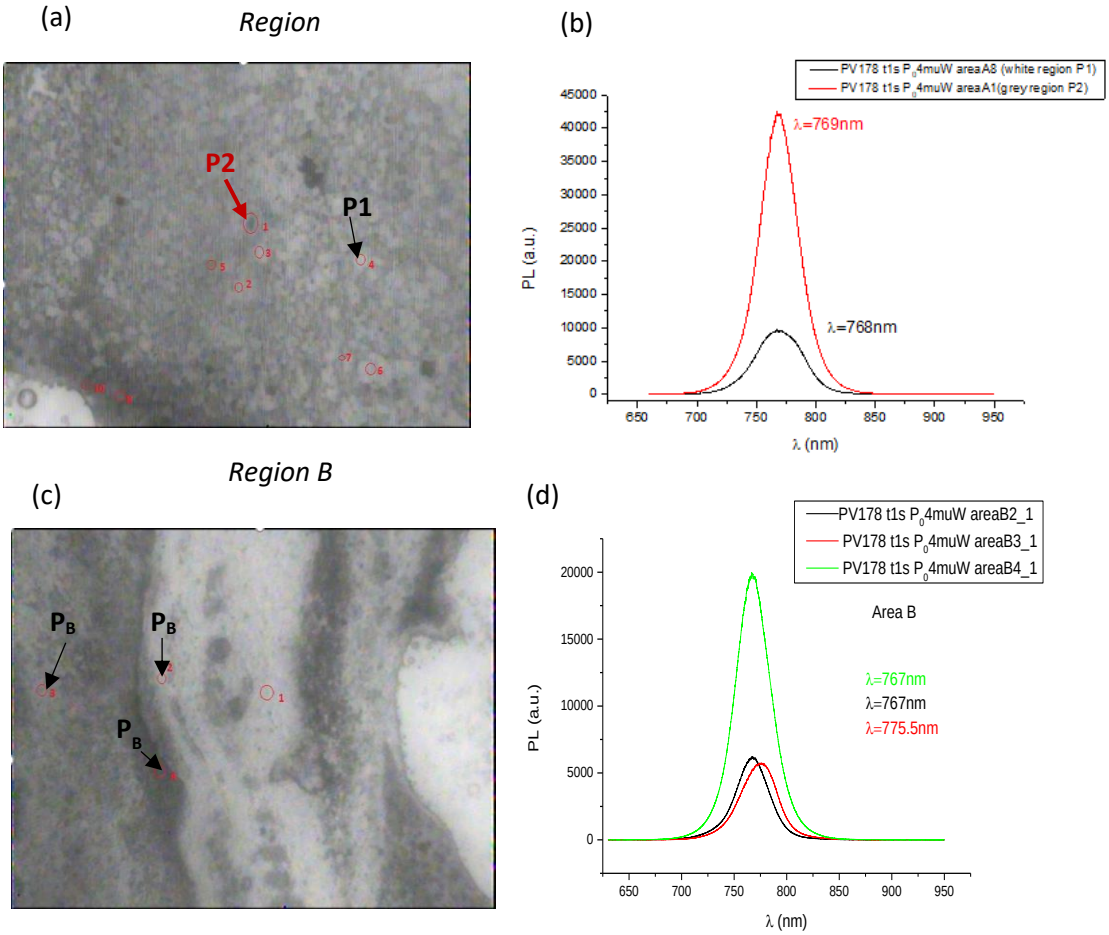

Figure 5.19: (a,d) Spectral maps and micro-PL spectra are shown for two different regions of the sample. The images show the points (P) from where the μ-PL spectra were taken.

According to the images showing the different regions of the sample that were studied (Figure 5.19a,c), we can distinguish two areas: grains of perovskite (white area) and another intermediate region (grey area). Grey areas show a relatively stronger emission while PL intensity in white regions is sensibly lower. In region A, both PL spectra show a PL peak around 770 nm. In region B, the PL emission corresponding to the various areas of the sample fluctuates between 767nm and 775nm. Therefore, in all cases, the PL emission appears at a wavelength range close to the 775nm, which is the expected wavelength for the $MAPbI_3$ perovskite structure. This confirms that the perovskite structure of sample PV178 is not only homogeneous but also that intermediate phases have not formed. To compare with the micro-PL spectra, the emission in macro-PL spectra peaks around λ=760nm. This difference in emission wavelength between the two experiments is presently not understood.

Subsequently, we applied the two-step method on nanowire templates, in order to observe the perovskite morphology around the nanowires. Samples PV184, 186, and 187 were fabricated which consist of Si/NWs (NW Sample 586)/perovskite. Dipping times varied between 20min, 60min and 4h for the above samples respectively. PbI_2 solution concentration was 1M. Moreover, the spinning conditions for PbI_2 deposition in the nanowire samples were milder compared to those used for PbI_2 deposition on Si/BCB substrates, in order to prevent nanowires from falling. Particularly, the spinning conditions of PbI_2 were 300rpm, 300rpm/s, t=10 sec, 1min

waiting and then spinning at 3000 rpm, 300 rpm/s, t=40 sec. In figure 5.20, SEM images show perovskite deposition on nanowire templates for PV184 and 187.

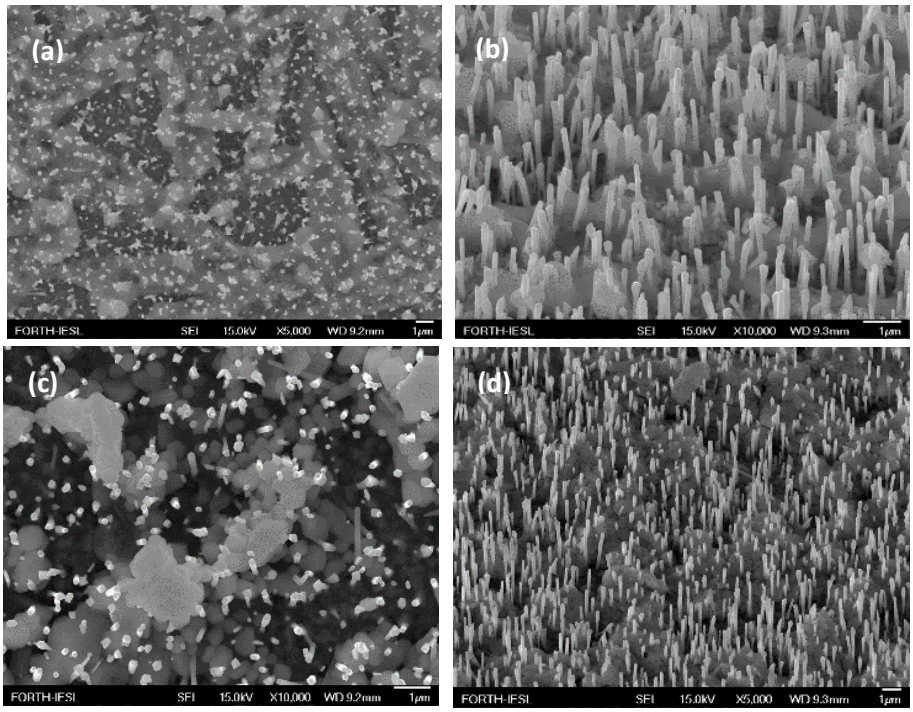

Figure 5.20: SEM images for (a,b) PV 184, (c,d) 187 in dipping times: 20 min and 4h respectively. The images were taken in planar view and under a tilt of 30^0.

As we can observe from the SEM images, perovskite material has formed around the nanowires, but there are regions in the samples that do not seem covered. Nanowires are mostly erect, except for some regions where they have fallen, possibly due to potential mishandling during the experimental process. In general, perovskite seems to form in thicknesses comparable to the height of nanowires. Moreover, perovskite crystals have formed at high dipping times (4h), something not compatible with our intention to have the perovskite embracing the nanowires. These first experiments showed promise about the growth of perovskite on nanowire arrays, but the perovskite morphology needs further optimization.

Hence, the following step was to change the PbI_2 solution concentration and see how perovskite forms at different PbI_2 thicknesses. For this reason, in a first stage we fabricated samples that consist of PbI_2 on Si/BCB substrates (PV188-191) with PbI_2 solution concentration varying between 0.3M, 1M, 1.5M, 2M.

In figure 5.21, we present SEM images for PV188-191, from which we can estimate the PbI_2 thickness for the different concentrations used.

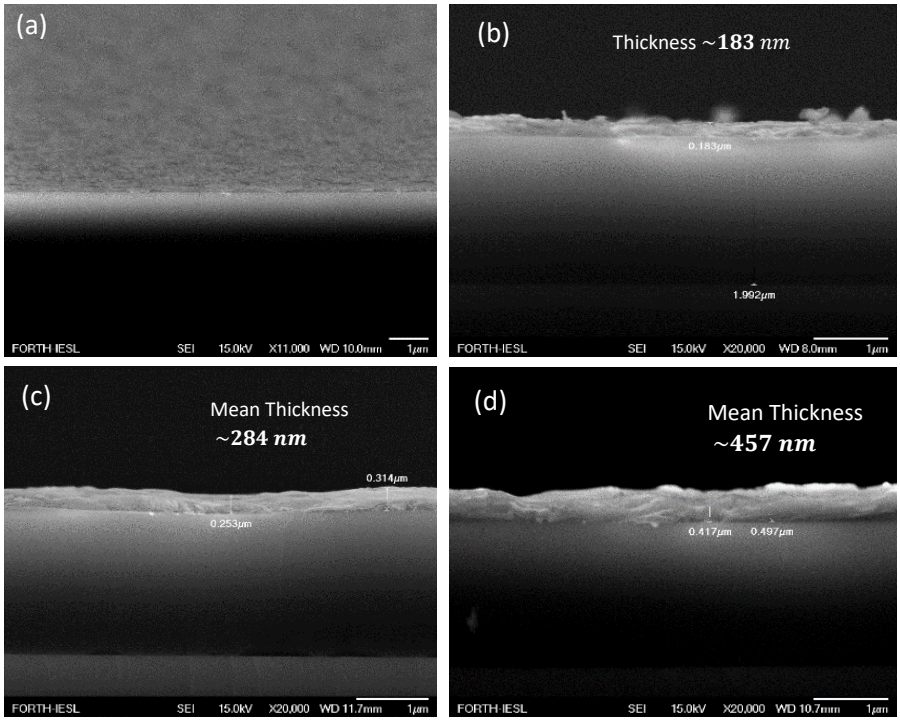

Figure 5.21: Cross section images in which PbI_2 thickness is observed for PbI_2 concentrations of (a) 0.3M, (b) 1M, (c) 1.5M,(d) 2M respectively.

For PbI_2 concentration of 0.3M, the layer of PbI_2 that formed was so thin that we could not extract any thickness value. For the various PbI_2 concentrations of 1M, 1.5M and 2M, the PbI_2 thickness was estimated to be about $183nm$, $284nm$ and $457nm$, respectively.

The PL spectra of samples PV188-191 are depicted in Figure 5.22. Compared to the bare Si/BCB sample, the PL emission in the Si/BCB/PbI_2 samples is largely modified, both in terms of spectral features and PL intensity. The BCB emits under 325nm excitation broadly, in the range 340-550nm (see curves in Figure 5.22). When PbI_2 is deposited on BCB, the PL intensity drops significantly in the 1M and 1.5M cases. In the 0.3M and 2M samples, the intensity does not vary so much, but the PL emission is narrowed-down in the 450-550nm range. This could be either due to PbI_2-related emission, expected around 510nm, or could be due to BCB emission modified by the PbI_2-absorption at wavelengths shorter than 450nm. At this stage, we cannot disentangle the two mechanisms.

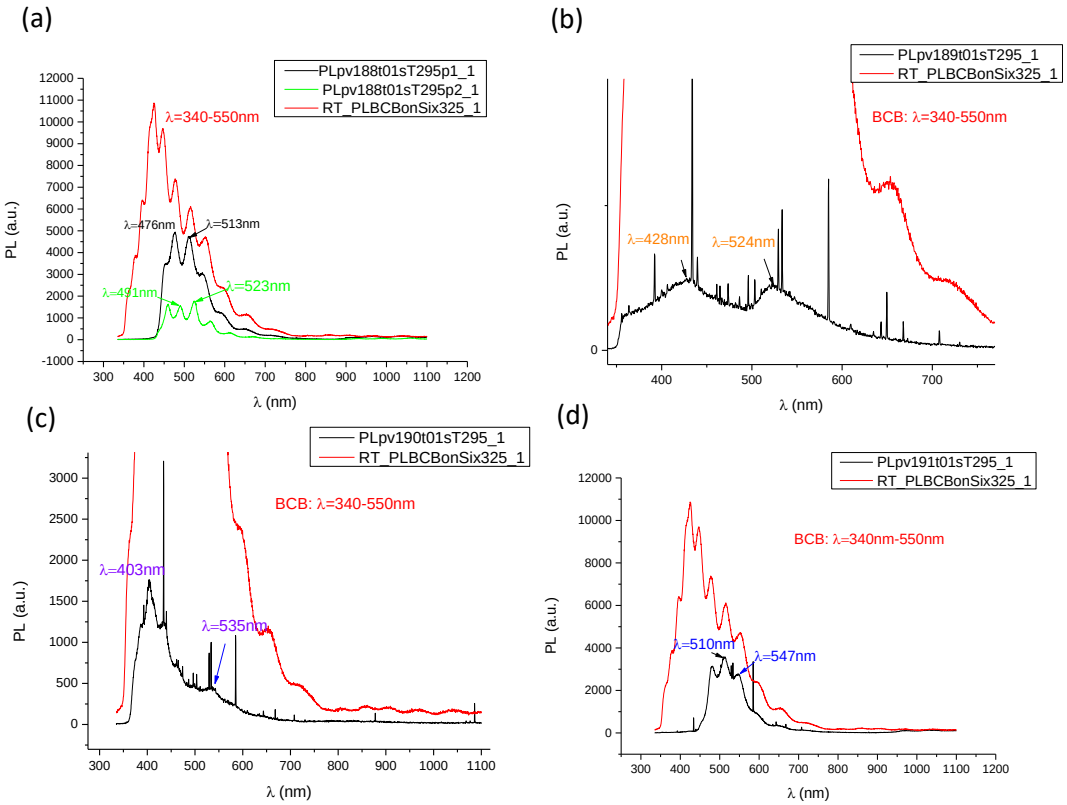

Figure 5.22: PL spectra for PV188-191 which are composed in PbI_2 concentrations of (a)0.3M, (b)1M, (c)1.5M, (d)2M respectively.

Next, we fabricated a new series of samples, PV213-216 which consist of Si/BCB/perovskite. They were fabricated via the two-step method using a solution concentration of 1.5M for PbI_2. In these samples, planar SEM images were taken first, in order to examine the morphology of the perovskite structure as a function of the dipping time in MAI solution.

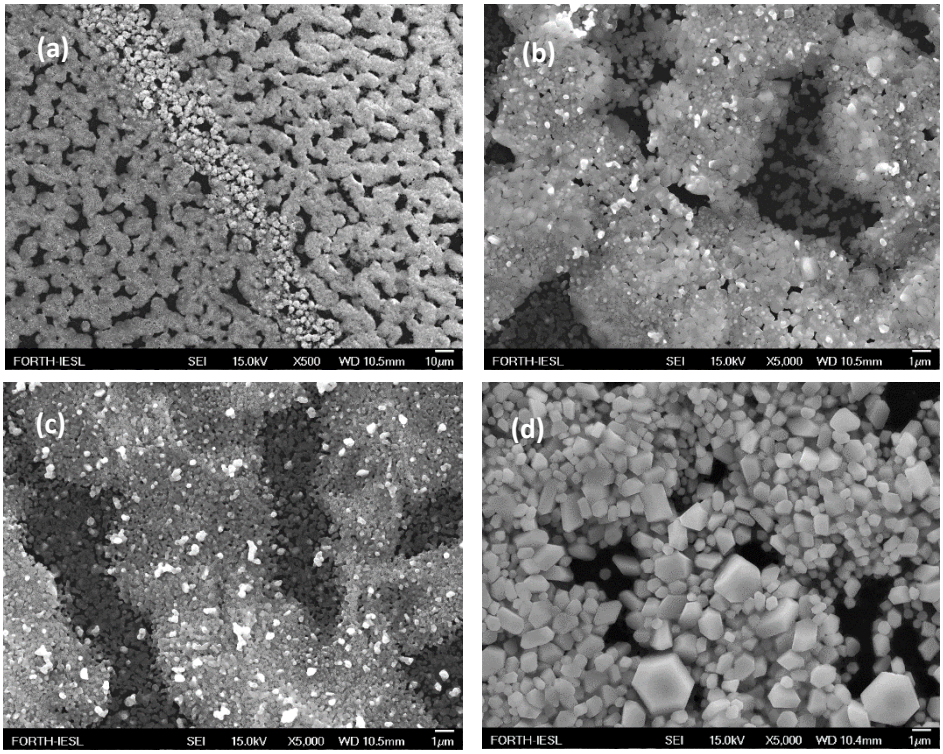

Figure 5.23: SEM images for samples PV213-216 which consist of perovskite on Si/BCB substrates in different dipping times. The time in dipping solution is 23min, 42min, 65min, 4h which correspond to fig.(a-d) respectively.

In the SEM images of figure 5.23, we observe perovskite formation in different dipping times in MAI solution for samples PV213-216. The dipping time was 23min, 42min, 65min and 4h respectively. These films came out macroscopically homogeneous and with a good film coverage. The perovskite morphology has improved in this series in terms of structure homogeneity and film uniformity compared to the samples fabricated at 1M PbI_2 solution concentration (see Figure 5.18b). In high dipping times (4h) perovskite crystallites formed, as can be seen in figure 5.23(d). The typical size of large crystals is $\sim 1.8\mu m$, while that of small crystals is $\sim 0.75\mu m$.

In figure 5.24 cross-section SEM images are shown for PV213-216, from which we extract a perovskite mean thickness of 581nm, 619nm, 775nm and 281nm for dipping times 23min, 42min, 65min and 4h respectively. We notice an increase in perovskite grain size and therefore perovskite thickness, as dipping time increases. For high dipping times, perovskite crystals formed. However, when they increase much in size, they collapse and perovskite structure is reconstructed. As a consequence, overall perovskite film thickness is decreased.

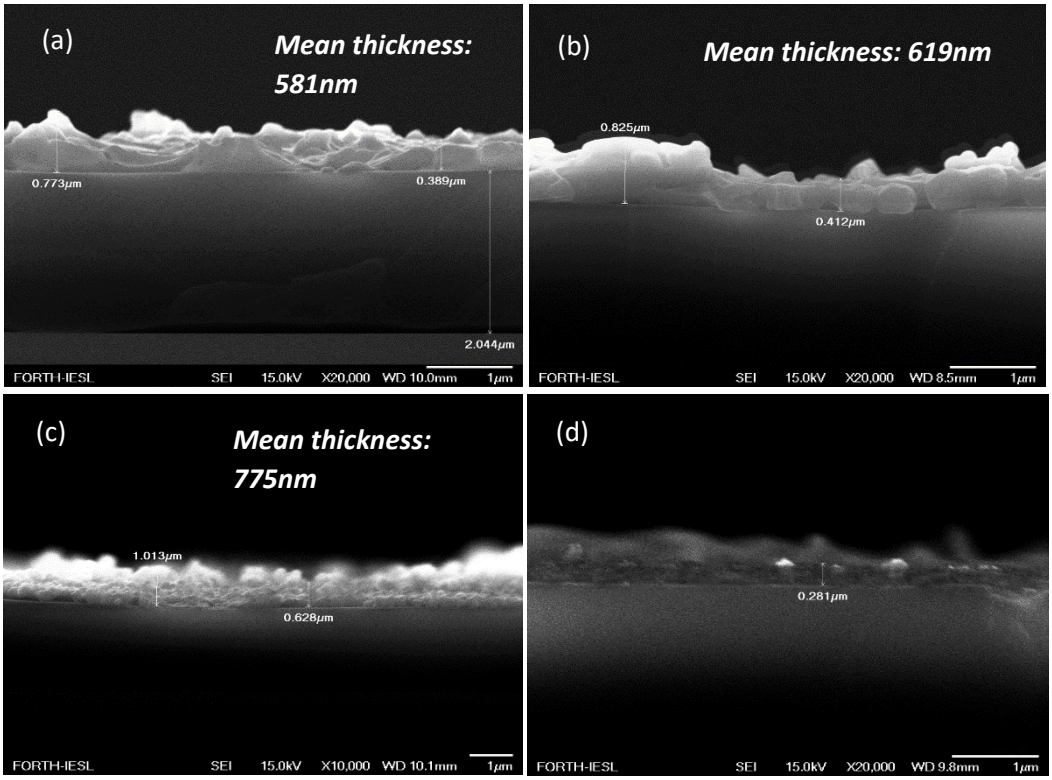

Figure 5.24: Cross-section SEM images for samples PV213-216.Perovskite is formed in dipping times (a) 23min, (b) 42min, (c) 65min, (d) 4h. Perovskite thickness is estimated for the various dipping times.

Photoluminescence spectra were taken from these samples. PL spectra showed a clean photoluminescence emission around λ=765nm in the different points of the samples, with some small deviations. In figure 5.25, we can see the PL spectrum for sample 215 (dipping time 65min) as an example.

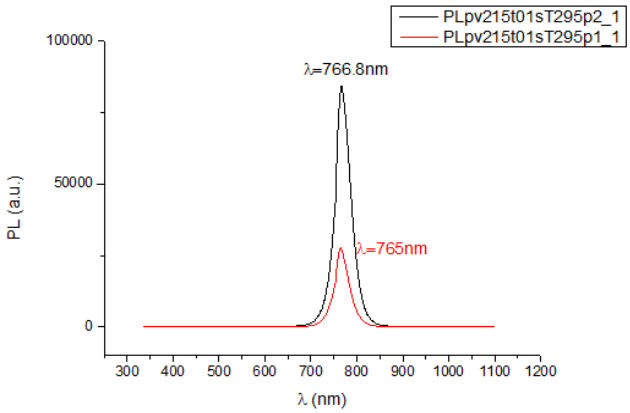

Figure 5.25: Photoluminescence (PL) spectra for PV 215 for dipping time 65min.

Owing to the fact that the two-step perovskite structure in the case of PbI_2 solution concentration of 1.5M showed better morphology and limited structural inhomogeneities,

compared to the solution concentration of 1M, we chose to carry on our next experiments in this concentration (C=1.5M). Therefore, we fabricated complete solar cell-like devices on NW templates via two-step method in 1.5M PbI_2 solution concentration. Accordingly, samples PV217-220 and PV225,226 were fabricated. As for samples PV217-220, the substrate was an n^+-type Si, on which GaAs nanowires have been grown. The nanowire template is sample 445L/R with BCB coverage. It is worth mentioning that after BCB coverage of the nanowire template, a subsequent step follows, namely BCB plasma-etching, in order to make the nanowires re-emerge from the BCB. In the case of nanowire samples 445L/R, due to a mistake in the etching process, the nanowire tips were destroyed after processing. Therefore, the nanowire templates 445L/R had only nanowires embedded in the BCB. A perovskite layer and successively a CuSCN layer were deposited on the BCB/nanowire templates. Then, an electrode made of semi-transparent 30nm-thick Au, was also deposited to complete the device. Electro-optical characterization was carried out in these samples to evaluate their photovoltaic response.

Samples PV217-220 consist of the following device configurations:

PV 217: Si/ NWs (NW sample 445L)/BCB/perovskite/CuSCN/Au (the dipping time in MAI solution is 55min)

PV 218: Si/ NWs (NW sample 445L)/BCB /perovskite/CuSCN/Au (dipping time is 2h)

PV219: Si/ NWs (NW sample 445R)/BCB /perovskite/CuSCN/Au (dipping time is 55min)

PV220: Si/ NWs (NW sample 445R)/BCB /perovskite/CuSCN/Au (dipping time is 2h)

The next set of nanowire samples that were fabricated are PV225,226. Nanowire sample D0449 was used as a nanowire template for these samples. The nanowire structure for sample D0449 is described in figure 5.6. Perovskite was deposited on the nanowire template via the two-step method using a 1.5M PbI_2 solution. Methylammonium iodide (MAI) dust had been dried at 200^0C for about 20 min, one day before the composition of the dipping solution, in order to remove water molecules that have potentially been absorbed by the atmosphere and made bonds with the hygroscopic MAI compound. After perovskite formation, the CuSCN and semitransparent 30nm-thick Au layers were deposited. The difference between PV225 and 226 lies in the spinning conditions during the deposition of CuSCN. CuSCN was spinned at 2000rpm, 1000rpm/s for 30sec for PV225, according to a conventional recipe. On the contrary, for PV226, CuSCN was spinned at 2000rpm,500rpm/s for 30s. The spinning rate was decreased in PV226, in order to test if it influences the nanowires. The configuration of samples PV225 and PV226 is the following:

PV 225: Si/BCB, NWs (NW sample D0449) /perovskite/CuSCN/Au (dipping time is 20min)

PV 226: Si/BCB, NWs (NW sample D0449) /perovskite/CuSCN/Au (dipping time is 20min and CuSCN is spinned at a lower acceleration)

Electro-optical characterization of the samples followed. Various dark and photo I-V curves were extracted, which can be seen in figure 5.26 below.

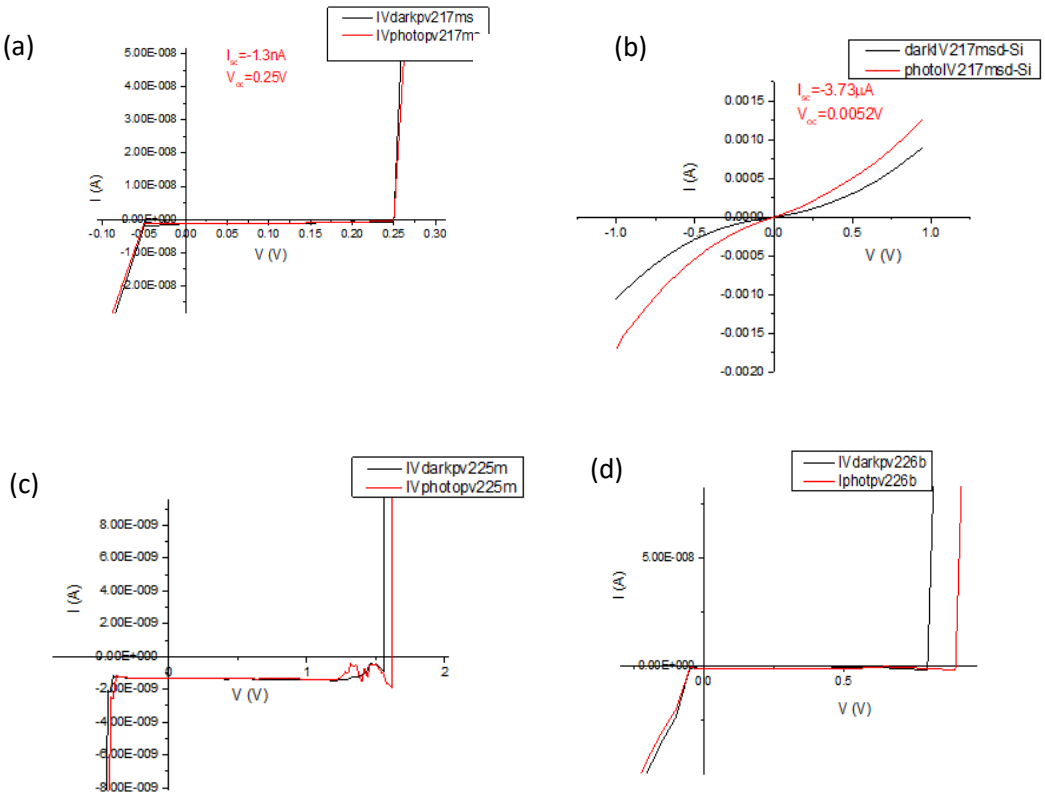

Figure 5.26: Electro-optical characterization of samples PV217,225,226. Dark and photo I-V curves are shown for each sample. For sample PV217, two diodes with different diameters are examined in (a) and (b).

With the exception of the I-V curves in Figure 5.26b, which were taken by scratching the top surface of the device and taking the bottom contact with the tip directly in the Si-substrate, the other I-V curves of Figure 5.26 showed very small currents, no photo-response and an unusual "zero-current" region. This behavior is quite unusual and suggests that this set of measurements were unreliable. Most probable reason for this behavior is the imperfect contact on the semitransparent Au-contact.

The small thickness of the Au layer (30nm), in order to keep it semitransparent with a transmission level of $\sim 30\%$, makes its contacting problematic, considering on one hand that the Au forms grains with typical grain size of tens of nm, i.e. comparable to the layer thickness in this case, and on the other hand the small thickness of the Au layer makes it likely that the tip scratches through the Au layer and dips inside the underneath CuSCN and perovskite layers, without forming an Ohmic contact. Another possible reason is the relatively rough surface of the underneath CuSCN/perovskite surface, where the 30nm of gold do not suffice to smoothen out this roughness and form a continuous metallic layer. At any rate, in the following, we abandoned the idea of using a semitransparent Au-layer and adopted the use of thicker-Au layers ~ 100nm for top contact.

As a next step and in order to evaluate the photovoltaic properties of the two-step $MAPbI_3$ perovskites, we have fabricated full diodes on FTO substrates (i.e. without nanowires). A schematic of the perovskite diodes is shown in Figure. 5.27.

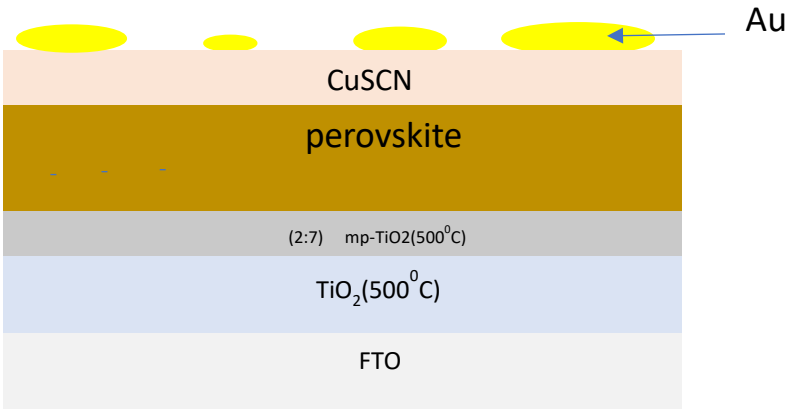

Figure 5.27: Device configuration for samples PV227-230 on FTO substrates

The time in dipping solution varied in these samples. Dipping time was 5min, 20min, 35min and 1h for samples PV227-230, respectively. Characteristic dark and photo I-V curves are illustrated in the following figure:

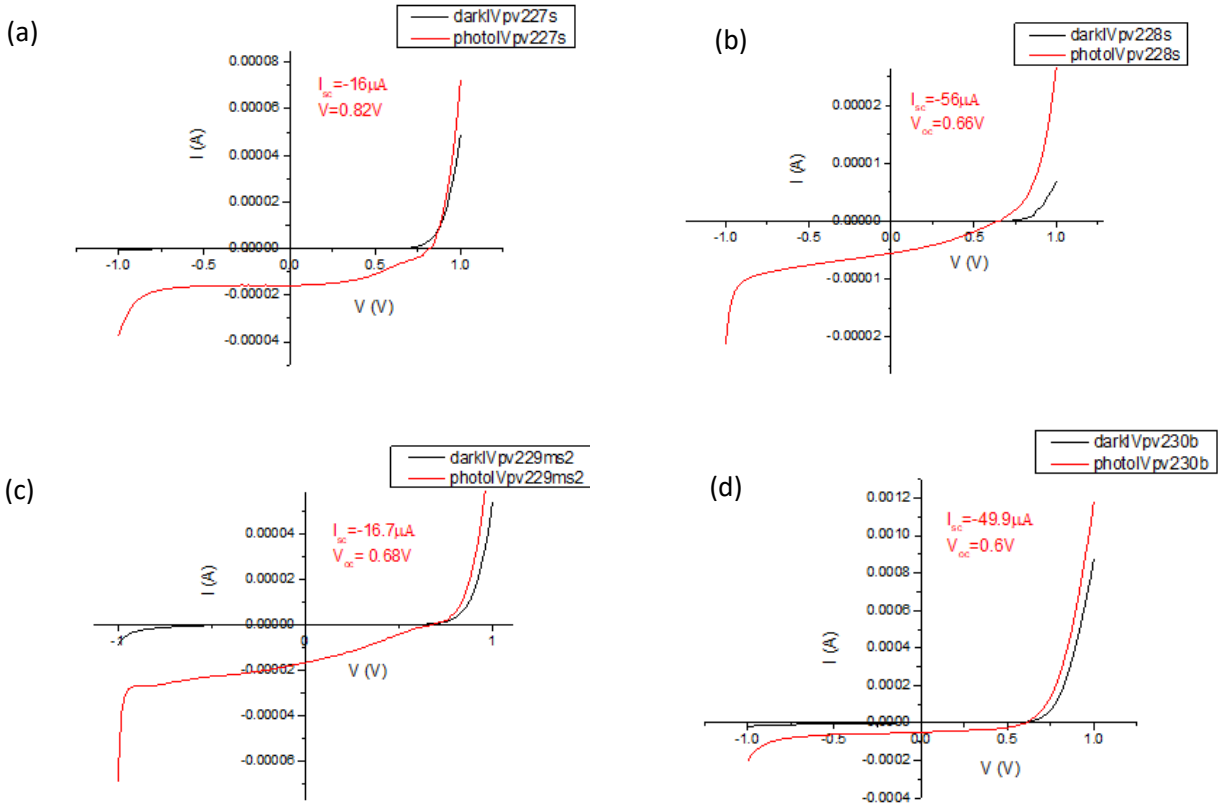

Figure 5.28: Dark and photo I-V curves for samples PV227-230, in dipping times: 5min, 20min, 35min and 1h, respectively.

Photo I-V analysis

From the analysis of the photo I-V curve we can extract characteristic parameters of the solar cell, like short circuit current (I_{sc}), open-circuit voltage (V_{oc}), fill factor (FF) and the device's efficiency (η). For the diode pv227s, I_{sc}=-16μA, V_{oc}=0.82V. In addition, fill factor is one parameter than can determine the maximum power (P_{max}) generated in the solar cell. It is expressed by equation 1.11. To extract the FF value, we plot the power (P) of the solar cell that is the product of current and voltage values as a function of voltage. P_m expresses the maximum point in the power vs Voltage (P-V) curve. For the diode pv227s, $P_{max}=5.5*10^{-6}$ W and the fill factor value is 0.42 or otherwise 42%, as it is estimated by the above equation.

Finally, the efficiency of the solar cell device is an important parameter that expresses the fraction of the incident power converting to electricity. It is expressed as:

$$\eta = \frac{P_m}{P_{in}}$$

P_{in} is the incident power which is equal to 1 sun (100mW/cm^2). The incident power P_{in}, given that the area of the diode pv227s is 0.006cm^2 is estimated to be $6*10^{-4}$ W. Moreover, $P_{max}=5.51*10^{-6}$W, so the extracted efficiency is η=0.0092 or 0.92%.

The results from photo I-V analysis on several diodes from each sample are summarized in the following table:

Sample	Diode	Diode area (cm^2)	Isc(μA)	J_{sc} (mA/cm^2)	V_{oc}(V)	FF	*η (%)*
PV227	b	0.0725	-8.78	-0.12	0.49	0.39	0.023
	ms1	0.0073	-6.83	-0.94	0.39	0.49	0.18
	ms2	0.0073	-48.9	-6.7	0.85	0.41	2.34
	s	0.006	-16	-2.67	0.82	0.42	0.925
PV228	b	0.0725	-25.7	-0.35	0.28	0.27	0.027
	s	0.006	-5.6	-0.93	0.66	0.32	0.2
PV229	b	0.0725	-28.3	-0.39	0.59	0.32	0.0746
	ms1	0.0073	-8.45	-1.16	0.49	0.32	0.179
	ms2	0.0073	-16.7	-2.29	0.68	0.28	0.434
	ms3	0.0073	-16	-2.19	0.59	0.41	0.53
	s	0.006	-5	-0.83	0.69	0.31	0.18
PV230	b	0.0725	-49.9	-0.69	0.6	0.46	0.192
	ms1	0.0073	-27.5	-3.77	0.58	0.37	0.82
	ms2	0.0073	-21.6	-2.96	0.6	0.39	0.7
	ms3	0.0073	-19.2	-2.63	0.54	0.38	0.54
	s	0.006	-7.12	-1.19	0.71	0.42	0.35

Table 1: Extracted parameters from photo I-V analysis for samples PV 227-230

The highest efficiency achieved was 2.34% for sample PV227 which corresponds to a dipping time of 5 min. We assume that the other samples did not exhibit higher efficiencies possibly due to other factors which affected perovskite formation during fabrication process. For example, a critical factor is PbI_2 thickness which varied significantly from sample to sample. Several factors can induce a non-uniform PbI_2 formation with inhomogeneous thicknesses, such as for instance an overly rough surface of the pre-deposited compact TiO_2 and mesoporous TiO_2 ETL layers. Moreover, humidity has an effect on PbI_2 formation. Particularly, humidity affects the solubility of PbI_2 in solution and thus affects the formation of the PbI_2 film. Moreover, apart from the non-uniform PbI_2 thickness, the perovskite structure is determined by CH_3NH_3I as well, which is the other constituent for the formation of perovskite. However, the CH_3NH_3I solution is also influenced by humidity. As it was previously referred, $CH_3NH_3^+$ can easily make bonds with H_2O molecules from the atmosphere. Therefore, the existence of H_2O molecules in CH_3NH_3I solution can distort the perovskite structure. All these factors affect the I-V characteristics and photo-response of the solar cell devices.

According to the photo I-V analysis of table 1, we notice that the short-circuit current values are low. Moreover, the open-circuit voltage (V_{oc}) values fluctuate between 0.5-0.8V, which are also below the values mentioned in literature. The values mentioned in literature for the two-step method are J_{SC}=15.1mA/cm^2, V_{oc}=1.036V, FF=0.62, efficiency (PCE)=9.7%, for remnant PbI_2 concentration of 1.7% at a dipping time of 15min *[42].* These literature values refer to the following solar cell configuration: FTO/compact TiO_2/mesoporous TiO_2 (2:7)/perovskite/Spiro-OMeTAD/Au, which is similar to our case. Possible reasons explaining the lower photo-response of our devices will be discussed below.

Dark I-V analysis

By analyzing dark I-V data, series (R_s) and shunt (R_{sh}) resistances were extracted for samples PV227-230. R_s and R_{sh} are parameters that contribute to power losses in the solar cell device. The existence of resistances can be represented in an external circuit, as in the schematic of figure 5.29.

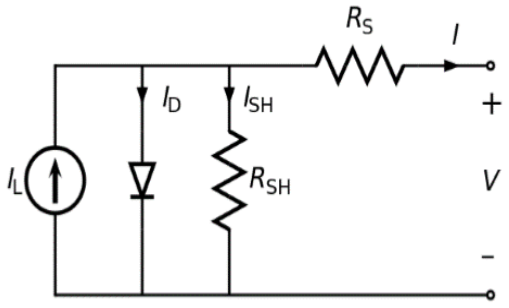

Figure 5.29: Representation of series and shunt resistances in an external circuit.

In a solar cell, there is the need to minimize the series resistance and maximize the shunt resistance, in order to eliminate power losses and enhance the current flow in the external circuit. Series resistance usually has an effect on short-circuit current (J_{sc}) values, while shunt resistance affects mainly the open-circuit voltage. The estimation of these resistance values will be analytically described for an indicative diode, PV229b. A dark I-V curve of this diode is illustrated in figure 5.30.

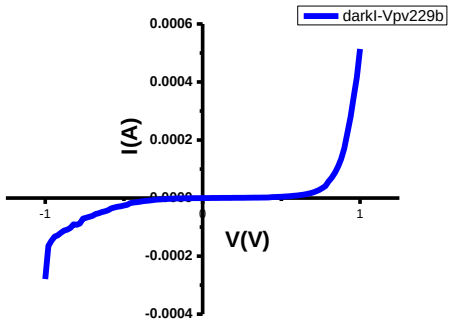

Figure 5.30: Dark I-V curve for the diode pv229b

The current equation of the diode under no illumination is given as: $I = I_O * \left(e^{\frac{q*V}{n*k_B*T}} - 1\right)$ $(eq.5.1)$. For V>50-100mV, the term -1 of the eq.(6.1) can be ignored. So, the equation is simplified as: $I = I_O * \left(e^{\frac{q*V}{n*k_B*T}}\right)$ $(eq.5.2)$, where: I_0 is the dark saturation current, q the electron charge, k_B the Boltzmann constant, T the absolute temperature. It is assumed that T=295K. I,V are the measured current and voltage respectively. In order to extract the ideality factor n, we log eq.(5.2). So, the equation

transforms to $\ln I = lnI_o + \frac{q*V}{n*k_B*T} * V$ $eq.(5.3)$. By plotting lnI-V from eq. (5.3), the slope of the linear curve equals with $\frac{q*V}{n*k_B*T}$ and the interception equals to lnI_o. Therefore, the ideality factor n and I_o can be extracted by the slope and the interception of the linear curve. Particularly, n and I_o can be obtained by linearly fitting the semi-log I-V diagram at low voltages, as shown in figure 5.31. It is worth mentioning that the ideality factor n is a parameter that changes at different voltages. Therefore, the ideality factor of different diodes should be always compared at a given voltage value.

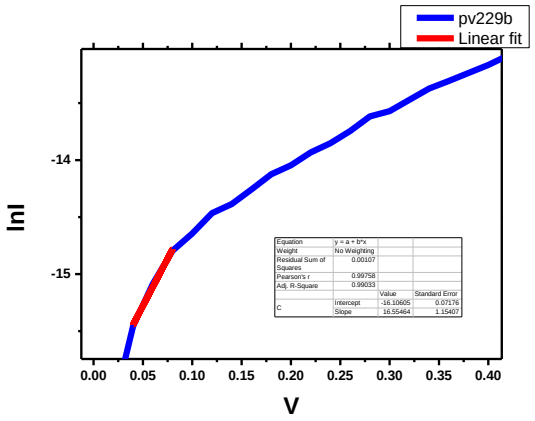

Figure 5.31: lnI-V curve for diode pv229b. The linear fit shown in red was used for the extraction of n and Io.

As we can see from figure 5.31, the linear fit for an indicative diode (diode PV229b) is expressed by the equation y=16.55-16.1 from which we extract that n=2.42 and I_O=1.02*10^{-7}A. Moreover, series resistance values can be extracted taking into account the relation: R_{series}=ΔV/I (eq.5.4), where ΔV=V_D-V is the voltage difference between the values of the linearly fitted equation (V) and the experimental values (V_D), at high voltages, where power losses become significant. In figure 5.32(a), we can see ΔV-I plot. The slope of the linear curve equals with R_{series}. For the diode at hand, R_{series}= 0.16 MΩ.

In figure 5.32(b), lnI-V curve is depicted representing the voltage difference ΔV.

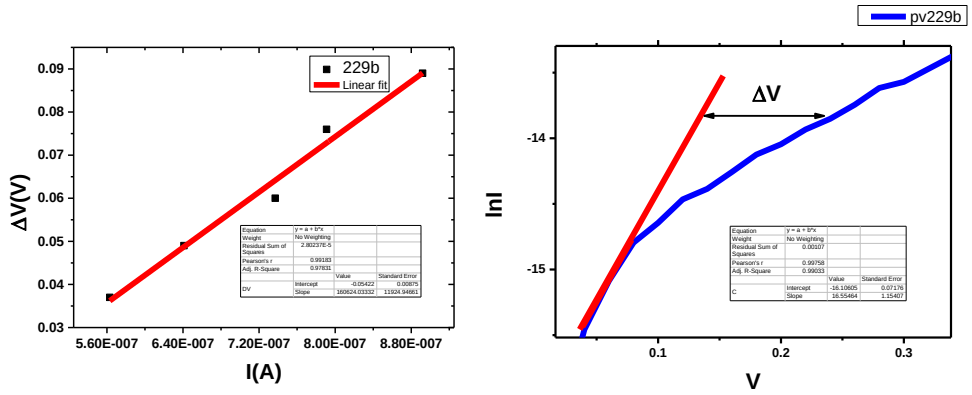

Figure 5.32: (a) Diagram ΔV-I for the extraction of R_{series} for the diode pv229b. (b) The voltage difference ΔV indicated in the ln I-V curve for the same diode.

As far as R_{shunt} is concerned, it dominates at low voltage. To extract R_{shunt} value, we consider a linear region from the dark I-V curve at very low voltages (close to zero).The slope of the curve that occurs by linearly fitting that region gives us information about the shunt resistance value. Particularly, $R_{sh} = \frac{1}{slope}$ $eq.(5.5)$ at low voltages. For the diode pv229b, R_{sh}=0.21MΩ. In figure 5.33, we can see the linear fit to the dark I-V curve at low voltage for the extraction of R_{sh}.

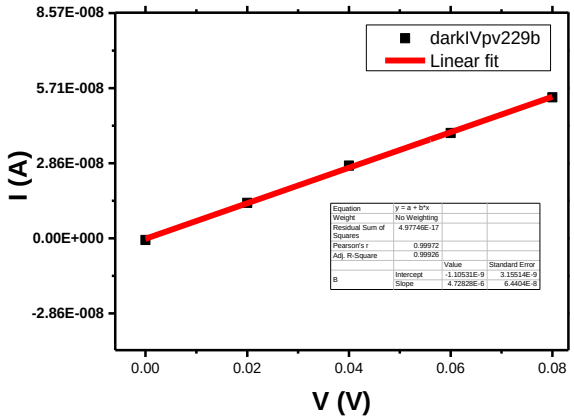

Figure 5.33: Linear fit to the dark I-V curve at low voltages to extract R_{sh} value for the diode pv229b.

The results from dark I-V analysis are shown in the following table:

Sample	*Diode*	R_{series}	R_{series}*A (Ω*cm^2)	R_{shunt}	R_{shunt}*A	*ideality factor n*
PV 227	b	376.1 Ω	27.3	-	-	3.58
	ms1	164 Ω	1.2	668 kΩ	4.9 kΩ*cm^2	5.1
	ms2	572 Ω	4.17	-	-	2.18
PV 228	ms	11.7 kΩ	85.4	19.2 kΩ	0.14 kΩ*cm^2	

PV 229	b	160 kΩ	11600	210 kΩ	15.2 kΩ*cm^2	2.42
	ms1	2.4 kΩ	17.5	138 kΩ	1 kΩ*cm^2	3.24
	ms2	-	-	0.44GΩ	3.26MΩ* cm^2	-
PV 230	ms3	-	-	680 kΩ	4.96 kΩ*cm^2	-
	s	408 Ω	2.45	490 MΩ	2.94 MΩ*cm^2	2.07

Table 2: Extracted parameters from dark I-V analysis for samples PV 227-230

From table 2, we can notice that most shunt resistance values are high as we would expect, with an optimum value of R_{sh}=2.94 MΩ*cm^2 for diode PV230s. As for series resistance, the optimum value is R_s=2.45 Ω*cm^2 for the same diode (230s). In table 2, dash means that the extraction of resistance was not feasible. Nevertheless, we note that in many diodes the series resistance acquires higher values compared to the literature.

To compare, literature values of shunt and series resistances are referred below: R_s=2.4 Ω*cm^2, R_{sh}=369,1 Ω*cm^2, demonstrating an efficiency of 13.8%. It is worth mentioning that the perovskite was formed by two-step method and the device configuration studied in that work was FTO/TiO_2(+$TiCl_4$)/mp-TiO_2 (2:7)/perovskite/Spiro-OMeTAD, which is similar to our case *[45]*. Therefore, we can suggest that series resistance value may have an effect on the I-V characteristics of the solar cell. However, other factors may also influence the solar cell performance. We should bear in mind that perovskite is formed by the reaction of the PbI_2 film with CH_3NH_3I solution. Thin PbI_2 film entails a low perovskite thickness, which results in limited light absorption. Moreover, as it is mentioned in chapter 2, remnant PbI_2 is essential for the effective photo-response of the solar cell. A thin layer of remnant PbI_2 that has not reacted to form perovskite can improve the efficiency of the solar cell. In our case, the high dipping times (35min, 1h) in combination with the low PbI_2 thicknesses possibly led to a total transformation of PbI_2 to perovskite thereby not maintaining a remnant PbI_2 layer, affecting solar cell efficiency.

To sum up, the insufficient absorption due to the low thickness of the perovskite absorbing layer, as well as the possible absence of remnant PbI_2 layer can justify the degraded efficiency of the solar cell, as well as the I-V characteristics of the photovoltaic device.

Impedance (C-V) measurements were taken for sample pv230s to examine the capacitance of perovskite materials vs voltage. In figure 5.34,C-V curves are illustrated at a signal frequency of 1MHz.

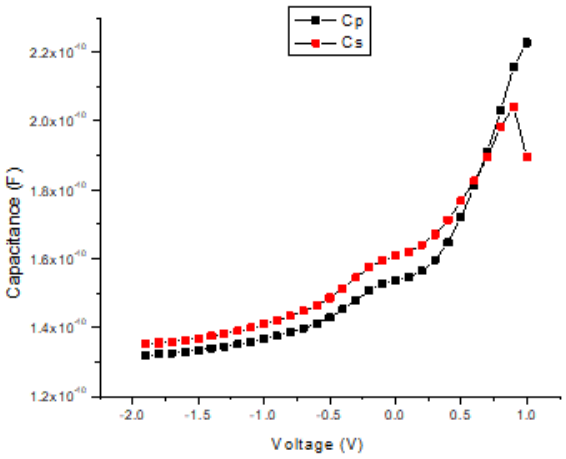

Figure 5.34: Capacitance measurements vs voltage in the case of parallel and series circuit model at a signal frequency of 1MHz for the diode pv230s.

As voltage increases, capacitance increases as well, due to charge depletion effect in the perovskite material.

As far as nanowire samples are concerned, as previously mentioned, the next thought was to improve Au contacts in order to examine the reliability of the results obtained in the previous nanowire devices (PV225,226). Particularly, we improved the front contact by depositing a 100nm thick Au, instead of a thin Au of thickness 30nm, in order to examine the dark I-V response. Au of 100nm is not transparent, because it is too thick. Therefore, we do not expect to study photo I-V response in this case and extract PV efficiency value. We deposited such a thick Au contact just to investigate whether bad contacts were responsible for the unexpected dark I-V response observed in samples PV225,226.

So, we fabricated a nanowire solar cell device (PV242) that consists of a nanowire template of sample D0449 after BCB coverage, on which perovskite is formed via two-step method. Subsequently, CuSCN is deposited as the hole transporting material and last metallic electrodes of Au are deposited. The device configuration is the one depicted in figure 5.8. The fabrication process is the same with samples PV 225,226. Dipping time for this sample is 15min.

Dark I-V curves have improved compared to the previous nanowire samples. Below, dark I-V curves are illustrated that were taken in two different setups.

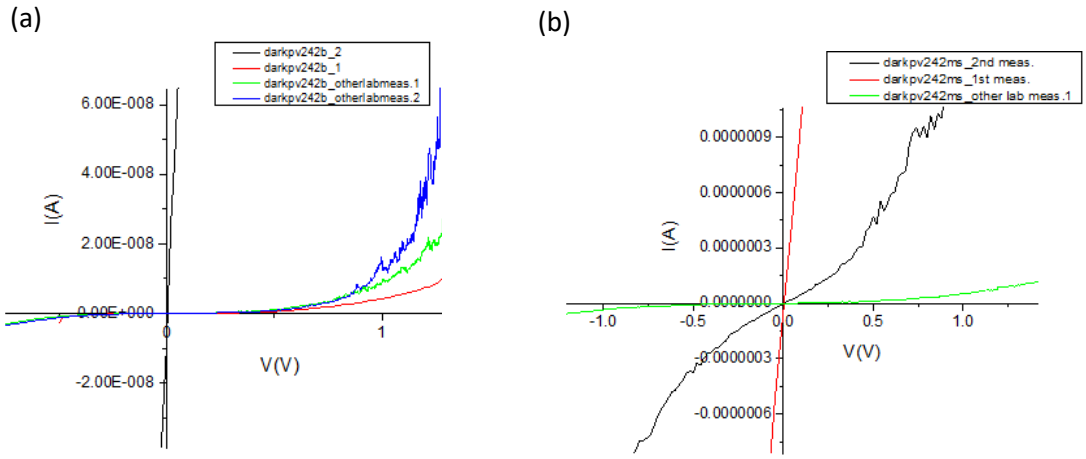

Figure 5.35: Dark I-V measurements taken in two different setups for diode (a) b and (b) ms of sample PV242. The various curves indicate repeated measurements for the particular diode.

We notice that the sample showed a very reasonable dark I-V response after increasing the thickness of the front Au contact. At zero voltage, we have zero current value. However, we notice that repeated I-V curves present different I-V response for measurements taken in both setups. This phenomenon is attributed to changes in material properties due to the polarization effect in the perovskite material,under the application of an electric stress. Moreover, we notice that current values are in the order of μA, which means that there is important carrier conduction and current generation.

The results from dark I-V analysis are the following:

Diode	***Measurements***	***Rs***	***R_{shunt}***	***Ideality factor n***
b	Meas.1	$1.23*10^8$ Ω	1.7GΩ	1.15
	Meas.2	$9.74*10^8$Ω	1.9GΩ	1.54
ms	Meas.1	3.92MΩ	0.16GΩ	1.96
	Meas.2	5.8MΩ	16MΩ	2.26

Table 3: Extracted parameters from dark I-V analysis for the diodes b and ms of sample PV242

We notice that values for both series and shunt resistances are high and they are comparable to each other.

The value of series resistance R_S is high, as indicated by our results. Particularly, $R_s \sim 10^8$ Ω for diode b. Series resistance values from bibliography for perovskite material is about 380Ω *[46].* Therefore, we tried to explain the value of series resistance and interpret the deviation from corresponding values of perovskite material from bibliography. We considered that device series resistance occurs from the contribution of series resistance both of perovskite material and nanowires. The general formula for resistance is:

$$R = \rho * \frac{l}{S} \qquad \textit{(eq. 5.6)}$$

In the case of nanowires, l represents the nanowire length, S the nanowire area and ρ the resistivity of GaAs nanowires. The nanowire density is $3*10^8$ NW/cm^2. Given that nanowire diameter is d~ 30nm, nanowire length is $l{\sim}1.2\,\mu m$ and the resistivity of intrinsic GaAs is $\rho=3.3*10^8$ Ω*cm at room temperature, we can extract that the series resistance of each nanowire is:

$R_{NW}=5.6*10^{15}$ Ω

Considering that nanowires are ordered in parallel with each other, the resistance of all nanowires is:

$\frac{1}{R_{total}}=\frac{N}{R_{NW}}$, where N is the number of nanowires.

The number of nanowires is the product of nanowire density with the area of the the diode. Particularly, N=<NW Density>*A_d. (A_d=0.0725cm^2 for b diode).

So, we extract that $\frac{1}{R_{total}}=\frac{3*10^8\frac{NWs}{cm^2}*0.0725cm^2}{5.6*10^{15}\Omega}=3.88*10^{-9}\Omega^{-1}\rightarrow R_{total}=2.6*10^8\Omega$, which reproduces fairly well the experimental value of series resistance for the diode b of sample PV242.

As for perovskite material, we estimate series resistance theoretically by using the formula of eq.5.6. Given that perovskite thickness is around 400nm, resistivity is $\rho=2*10^7$ Ω*cm at room temperature for $MAPbI_3$ perovskite *[44]* and S=0.0725cm^2, the area of diode b ,

$Rs_{(perov.)}=11*10^3$ Ω.

This means that the resistance from the nanowires is predominant, while the resistance from perovskite is negligible.

As noted earlier, we cannot take I-V measurements under illumination for sample PV242. However, we wanted to check if the diodes of this sample are photosensitive at all. So, we illuminated with a spot size larger than the Au contact. Below, there is a schematic illustration of the illuminated area. The spot diameter of the beam was 5mm.

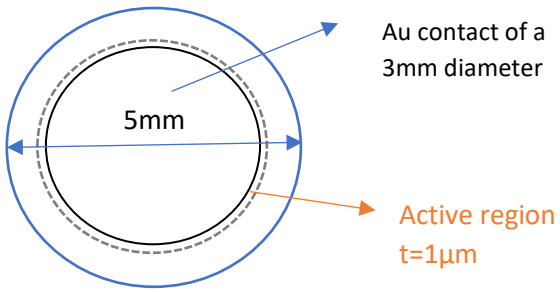

Figure 5.36: A schematic illustration of the illuminated area and the active region. The beam spot size is 5mm.

We consider that only a ring area of thickness $t{\sim}1\mu m$ is able to collect photocarriers and constitutes thus the active area. The diffusion length of carriers in good quality perovskite is estimated about 1μm. So, carriers that travel a distance longer than 1μm will recombine and

will not be able to reach the electrode. Au contacts have different sizes. The big (b) contact has a diameter of 0.3cm and the "medium small" (ms) contact has a diameter of 0.096cm. So, we can calculate the ring area that is the active region for diodes b and ms based on figure 5.36. So, the active area is A_b=9.42*10^{-5} cm^2 for the b contact and it is A_{ms}=3*10^{-5} cm^2 for the ms contact.In figure 5.37 dark and "photo" I-V curves are depicted for the diodes b and ms of sample PV 242.

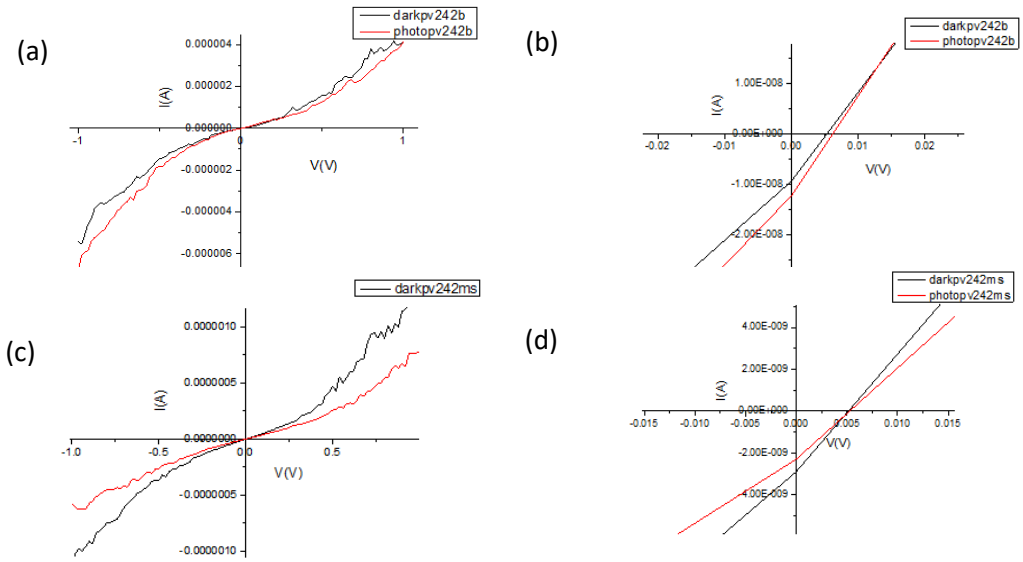

Figure 5.37: (a),(c)Dark and "photo" I-V curves for diode b and ms of sample PV242 respectively.(b),(d) A zoom at a region near zero values for diodes pv242b and ms respectively.

We can see from figure 5.37 that dark I-V curves and I-V curves under illumination are almost identified. The results from the analysis of photo I-V curves are shown in the following table:

Diode	*I_{sc}(nA)*	*V_{oc}(V)*	*FF*	*η (%)*	*P_{max}(W)*	*J_{sc}(mA/cm^2)*	*Ring Area (cm^2)*
b	-12.3	0.0062	-3.6*10^{-6}	2.9*10^{-9}	2.75*10^{-16}	-0.131	9.42*10^{-5}
ms	-2.3	0.0053	-4.2*10^{-6}	1.7*10^{-9}	5.13*10^{-17}	-0.07667	3*10^{-5}

Table 4: Extracted parameter from photo I-V analysis for sample PV242.

According to table 4, we infer that the sample PV242 is not photosensitive. Carriers cannot be collected from a region around metallic contacts. This could be related to the limited diffusion length of our perovskite material.

So, there is the need to improve front contact or finding alternative solutions to implement illumination measurements on the nanowire samples. Moreover,efforts need to be made to

reduce the series resistance of the nanowires.This can be achieved by increasing the nanowire diameter and modifying its doping profile. For instance, by increasing the nanowire diameter by a factor of 5, the series resistance can be reduced by a factor of 5^2. More importantly if one increases the doping level of the GaAs core up to 10^{16} cm^{-3}, the resistivity is expected to drop by many orders of magnitude. Specifically, the resistivity for GaAs at room temperature at a doping concentration 10^{16} cm^{-3} can be estimated by the relation: $\sigma=1/\rho=q*\mu_n*n$ where ρ the resistivity, μ_n the mobility of electrons for GaAs equal with $8500cm^2/(V*s)$ and n the doping concentration. So, we obtain $\rho=0.074\ \Omega*cm$, a value 10 orders of magnitude lower than the intrinsic case.

Conclusions

In this thesis, nanowire/perovskite solar cell devices were fabricated via the two-step method. Moreover, samples with the structure Si/BCB/perovskite were also fabricated to optimize the perovskite morphology on Si/BCB substrates. PbI_2 solution concentrations in C=1M and C=1.5M were examined in our experiments. SEM images were taken for the samples. Moreover, solar cell devices were fabricated on FTO substrates. Finally, the samples were electro-optically characterized. Specifically, I-V measurements and PL measurements were implemented. In conclusion, we infer that the thickness of Au contacts is the main factor which influences I-V response in our nanowire samples. By improving front contact, the nanowire sample (PV242) showed up the expected I-V response. Nevertheless, we need to find a way to illuminate the diode while at the same time ensuring improved Au contacts. One possible way is to use a conducting oxide instead of Au as a front contact that is transparent and therefore permits illumination through the diode. The other solution is an inverse design where the holes will be evacuated through a p^+-Si substrate and the electrons from a top ITO contact. Moreover, efforts need to be made in order to reduce the series resistance of the nanowires. This can be achieved by increasing the nanowire diameter and modifying its doping profile. Another way is to control the thickness and quality of perovskite which may result in improved I-V characteristics and optimized values in shunt and series resistances. Finally, we need to elaborate more on the polarization effect, in order to interpret the instability of I-V under repeated measurements.

REFERNECES

[1] S.L.Tan, Y.Genuist, M.J. den Hertog, E.Bellet Amalric , H.Mariette and N.T.Pelekanos, “Highly uniform zinc blende GaAs nanowires on Si(111) using a controlled chemical oxide template”, Nanotechnology, vol 28,no.25,p.255602, Jun.2017

[2] Chito E.Kendrick, Joan M. Redwing, Semiconductors and Semimetals, “Silicon Micro/Nanowire solar cells”, vol. 94, p.185-225, 2016

[3] Lorenzo Morresi, Silicon Based Thin film solar cells, “Basics of Molecular Beam Epitaxy (MBE) technique, p.81-107,2013

[4] Raul J.Martin-Palma, Akhlesh Lakhtakia, “Vapor-Deposition Techniques”-chapter 15,Engineered Biomimicry, p.383-398, 2013

[5] Moratis et al., “Strained GaAs/InGaAs Core-Shell nanowires for PV Applications, Nanoscale Research Letters, vol.11,no.1, p.176, 2016

[6] Jesper Wallentin et al., “InP Nanowire Array Solar Cells Achieving 13.8% Efficiency by Exceeding the Ray Optics Limit”, Suppl.material,Science,339(6123),p.1057-1060, 2013

[7] Ingvar Alberg et al., “A GaAs Nanowire Array Solar Cell with 15.3% Efficiency at 1 Sun”, EEE Journal of Photovoltaics, vol.6, no.1, p.185, Jan.2016

[8] S.Noor Mohammad, “Understanding quantum confinement in nanowires:Basics applications and possible laws”,J.Physics: Condensed Matter 26,423202, 2014

[9] Lichun Zhang et al., “Self-catalyzed molecular beam epitaxy growth and their optoelectronic properties of vertical GaAs nanowires on Si(111), Materials Science in Semiconductor Processing,52, 68-74, 2016

[10] Erik C.Garnett, Mark L.Brongersma, Yi Cui and Michael D.McGehee, “Nanowire Solar cells”, Annual Review Materials Research, 2011, 41: p.269-295

[11] K.V.R. Murthy and H.S. Virk, “Luminescence phenomena: An introduction”, Defect and Diffusion Forum, vol.347,pp1-34,2014

[12] Mhammadreza Khorasaninejad and Simargeet Singh Saini, “Silicon nanowire optical waveguide (SNOW), Optics Express, vol.8, no.22, 23442,2010

[13] Yunyan Zhang and Huiyun Liu, “Nanowires for High-Efficiency Low-cost Solar PVs”, Crystals (2019),9(2),87

[14] Gaute Otnes, Magnus T.Borgstrom, “Towards high efficiency nanowire solar cells, Nano Today, vol.12,p.31-45,2017

[15] H.-J. Choi, “Vapor–Liquid–Solid Growth of Semiconductor Nanowires,” in Semiconductor Nanostructures for Optoelectronic Devices, G.-C. Yi, Ed. Berlin, Heidelberg: Springer Berlin Heidelberg, 2012, pp. 1–36.

[16] S. Sharma, K. K. Jain, and A. Sharma, “Solar Cells: In Research and Applications—A Review,” Mater. Sci. Appl., vol. 06, no. 12, pp. 1145–1155, 2015.

[17] Hyun Suk Jung and Nam-Gyu Park, “Perovskite solar cells: From Materials to Devices” small,vol.11,No 1,p.10-25,2015

[18] Yon-Hyun Seo,Eun-Chong Kim, Se-Phin Cho, Seok-Soon Kim,Seok-In Na, “High performance planar perovskite solar cells: Influence of solvent upon performance”, Applied Materials Today,vol.9,p.598-604, 2017

[19] X. Wang, Y. Fang, L. He, Q. Wang, T. Wu, “Influence of compact TiO2 layer on the photovoltaic characteristics of the organometal halide perovskite-based solar cells”, Mater. Sci. in Semic. Proc., Vol. 27, 2014, p. 569-576

[20] S. Shi, Y. Li, X. Li, H. Wang, “Advancements in all-solid-state hybrid solar cells based on organometal halide perovskites, Materials Horizons”, Vol. 2, p. 378-405,2015.

[21] Fedros Galatopoulos, Achilleas Savva, Ioannis T. Papadas, and Stelios A. Choulis,” The effect of hole transporting layer in charge accumulation properties of p-i-n perovskite solar cells”, Applied Physics Letter (APL) Materials, vol.5, 076102,2017

[22] Di Zhou, Tiantian Zhou, Yu Tian, Xiaolong Zhu, and Yafang Tu, “Perovskite-Based Solar Cells: Materials, Methods, and Future Perspectives,” Journal of Nanomaterials, vol. 2018, Article ID 8148072, 2018.

[23] Y. Zhang, W. Liu, F. Tan, Y. Gu, “The essential role of the poly(3-hexylthiophene) hole transport layer in perovskite solar cells”, Journal of Power Sources, Vol. 274, No. 0, p. 1224-1230, 2015

[24] Tze-Bin Song et al,”Perovskite solar cells: Film formation and properties”, Materials Chemistry A, vol. 3 p. 9032-9050,2015

[25] Claudio Quarti et al,“Structural and Optical Properties of Methylammonium Lead Iodide Across the Tetragonal to Cubic Phase Transition: Implications for Perovskite Solar Cells”, Energy and Environment Science, vol.9, p.155-163, 2016

[26] Martin A. Green, Anita Ho-Baillie and Henry J. Snaith, “The emergence of perovskite solar cells”, Nature Photonics, vol.8,p.506-514, 2014

[27] Nam Gyu Park, “Perovskite solar cells: an emerging photovoltaic technology”, Materials today ,vol.18,no 2,p.65-72,2015

[28] M. Ye, X. Wen, M. Wang, J. Iocozzia, N. Zhang, C. Lin, Z. Lin, “Recent advances in dye-sensitized solar cells: From photoanodes, sensitizers and electrolytes to counter electrodes”, Materials Today, Vol. 18, No. 3, p. 155-162,2015

[29]: S.Kayali, “I. GaAs Material Properties”,Published 1997

[30]: Gallium Arsenide, Encyclopedia of Materials: Science and Technology (2nd Edition),p.3431-3435, 2001

[31]: S.M.Sze, “Semiconductor Devices Physics and Technology”,2nd Edition, J.Wiley, 2002

[32]:T.Ibn-Mohammed et al., “Perovskite solar cells: An integrated hybrid lifecycle assessment and review in comparison with other photovoltaic technologies”, Renewable and Sustainable Energy Reviews 80, p.1321-1344, 2017

[33]: T.Bak,M.K. Nowotny, Sheppard and J.Nowotny, “Mobility of Electronic Charge Carriers in Titanium Dioxide”, J.Phys. Chemistry.C, vol. 112, No.33, pages 12981-12987, 2008

[34]: Kofstad, P. Non stoichiometry, “Diffusion and Electrical Conductivity in Binary Metal Oxides”, Wiley-Interscience, 1972

[35]:Adrian P.Mouritz, Introduction to Aerospace materials,“4-Stengthening of metal alloys”,p.57-90, 2012

[36]: R.Bourguiga et al., “Charge transport limited by grain boundaries in polycrystalline octithiophene thin film transistors”,The European Physical Journal Applied Physics, 19, p.117-122, 2002

[37]: S.M.Sze, M.K.Lee, “Semiconductor Devices, Physics and Technology”,3rd Edition

[38]: Sergio Valencia, Juan Miguel Martin, Gloria Restrepo, “Study of the Bandgap of Synthesized Titanium Dioxide Nanoparticles using the Sol-gel method and a Hydrothermal Treatment”, The Open Materials Science Journal, 4 ,p.9-14, 2010.

[39]: D.A.H. Hanaor, C.C.Sorrell, “Review of the anatase to rutile phase transformation”,J.Materials Science, vol.46,p.855-874, 2011

[40]:Elizabeth von Hauff, “Impedance spectroscopy for Emerging Photovoltaics”, J.Physical Chemistry. C 2019, 123, p.11329-11346

[41]: Operational Manual (HP 4284A Precision LCR Meter), Chapter 6, Measurement Basics, 1998

[42] Remnant PbI_2 an unforeseen necessity in high-efficiency hybrid perovskite-based solar cells, Apl.Materials 2,091101, 2014

[43] Hole-Transport Layer Processed from Aqueous Precursor solutions and their Application in Thin film Transistors and highly efficient Organic and Organometal Halide Perovskite Solar cells, Nilushi Wijeyasinghe et al., Advanced Functional Materials 27,1701818,2017

[44] Pisoni et al.,“Metallicity and conductivity crossover in white light illuminated $CH_3NH_3PbI_3$ perovskite” Materials science,16:15:54,2016

[45] Paola Vivo et al., “Influence of TiO_2 compact layer precursor on the performance of perovskite solar cells”, Organic Electronics 41,p.287-293,2017

[46] I.M,Dharmadasa, Y.Rahaq, A.A.Ojo, T.I.Alanazi, “Perovskite solar cells:a deep analysis using current-voltage techniques, Materials in Electronics,30, p.1227-1235, 2019

[47] M. A. Green, “Solar cell fill factors: General graph and empirical expressions,” Solid-State Electron., vol. 24, no. 8, pp. 788–789, Aug. 1981.